STABLE NANOCRYSTALLINE Au FILM STRUCTURES FOR SLIDING ELECTRICAL CONTACTS

Jon-Erik Mogonye, B.S., M.S.

Dissertation Prepared for the Degree of

DOCTOR OF PHILOSOPHY

UNIVERSITY OF NORTH TEXAS

May 2016

APPROVED:

Thomas W. Scharf, Major Professor
Somuri V. Prasad, Minor Professor
Samir Aouadi, Committee Member
Rajiv Mishra, Committee Member
Sundeep Mukherjee, Committee Member
Andrey Voevodin, Chair of the Department of Materials Science and Engineering
Costas Tsatsoulis, Dean of the College of Engineering, Dean of the Toulouse Graduate School

Mogonye, Jon-Erik. *Stable Nanocrystalline Au Film Structures for Sliding Electrical Contacts*. Doctor of Philosophy (Materials Science and Engineering), May 2016, 124 pp., 6 tables, 52 figures, references, 22 titles.

The main focus of this dissertation was to synthesize nanocrystalline Au films with grain structures capable of remaining stable during thermal exposure and under sliding electrical contact stress and the passing of electrical current. Simultaneous friction and ECR experiments of low fluence (< $1x10^{17}$ cm^{-2}) He and Ar ion implanted Au films showed reduction in friction coefficients from ~1.5 to ~0.5 and specific wear rates from ~$4x10^{-3}$ to ~$6x10^{-5}$ $mm^3/N{\cdot}m$ versus as-deposited Au films without significant change in sliding ECR (~16 mΩ). Nanoindentation hardness results revealed an increase from 0.84 GPa for as-deposited Au to ~1.77 GPa for Au uniformly implanted with 1 at% He. These strength increases are correlated with an Orowan hardening mechanism that increases proportionally to (He concentration)$^{1/3}$. Au-ZnO nanocomposite films in the oxide dilute regime (< 5 vol% ZnO) were investigated for low temperature aging stability in friction and ECR. Annealing at 250 °C for 24 hours Au-(2 vol%)ZnO retained a friction coefficient comparable to commercial Ni hardened Au of ~ 0.3 and sliding ECR values of ~35 mΩ. Nanoindentation hardness increases of these films (~2.6 GPa for 5 vol% ZnO) are correlated to microstructure via high resolution TEM and scanning electron microscope cross-sections to both Hall-Petch and Orowan strengthening mechanisms. Using the M-S model in combination with a model describing solute drag stabilized grain growth kinetics we present a new technique to probe grain boundary mobility and thermal stability from in-situ electrical resistivity measurements during annealing experiments.

ACKNOWLEDGEMENTS

First and foremost I would like to express my gratitude to Prof. Thomas W. Scharf who not only provided me the opportunity to continue research work with him, but who also became the greatest lecturer and mentor I have had the privilege to learn from in my young adult life. I sincerely appreciate his trust, guidance, and most of all patience in my endeavors to grow as an intellectual and as an adult.

I would also take this opportunity to express my gratefulness of Dr. Somuri V. Prasad who has been both a caring and resolute adviser who provided me the opportunity to continue my academic career. I have learned a great deal about research and how to present oneself from his wisdom in our many discussions.

I would also like to thank the many others at Sandia National Laboratories, including Dr. Nicolas Argibay, Dr. Khalid Hattar, Dr. Paul Kotula, Dr. Ronald Goeke, Dr. Joe Michael, Dr. Michael Dugger, Dr. Tom Bucheit, Dr. Barney Doyle, Bonnie McKenzie, Cory Gibson, Lisa Lowery, Michael Rye, Michael Marshall, Bruce McWatters, Stuart Van Deusen, and Rand Garfield for their fruitful discussion, collaboration, and assistance while conducting portions of this work. I am also thankful to Dr. Samir Aouadi, Dr. Rajiv Mishra, and Dr. Sundeep Mukherjee at the University of North Texas for serving on my committee.

This work was partially supported by the US Department of Energy, Office of Basic Energy Sciences. Sandia National Laboratories is a multi-program laboratory managed and operated by Sandia Corporation, a wholly owned subsidiary of Lockheed Martin Corporation, for the U.S. Department of Energy's National Nuclear Security Administration under contract DE-AC04-94AL85000.

TABLE OF CONTENTS

Page

LIST OF TABLE

Page

LIST OF FIGURES

Page

CHAPTER 1

INTRODUCTION

1.1 Tribological Applications of Sliding Electrical Contacts

The necessity to provide efficient transfer of electrical current between moving parts has been an engineering challenge since the invention of the unipolar motor in 1832 by Michael Faraday. With increasing implementation of electrical motors and generators occurring with the industrial revolution, and further increase in electrical contacts with the advent of the ever expanding electronics industry, the technological applications of sliding electrical contacts has become widespread. Sliding electrical contacts can be found in DC motor and generator current collector slip rings, printed circuit board edge connectors, data cable pin connectors and receivers, microelectromechanical systems (MEMS), circuit relays and switches, instrument signal transfer slip rings and many more applications. The main engineering challenges associated with these applications, especially long service life slip rings, is minimized wear and stable wear performance, acceptable friction to minimize mechanical energy losses, and low and stable electrical contact resistance to minimize Joule heating, increase electrical energy transfer efficiency, and provide suitable signal transfer.

1.2 Motivation

1.2.1 Industrial Use and Review of Electroplated Hard Gold

The use of gold in the electronics industry has reached over 300,000 kg per year in 2010 [1]. According to an evaluation by Goodman in 2002, when gold use in the electronics industry was 280,000 kg per year, the majority of this gold was used in electrical contacts, most

frequently electroplated gold [2]. Gold is used in tribological electrical contacts due to its high conductivity and excellent corrosion and oxidation resistance. Although electroplated hard gold has produced an improvement over pure gold platings in friction and wear performance, it has reliability issues regarding electrical contact resistance (ECR) over time and at elevated temperatures. The reliability issue is related to an increase in ECR due to the formation of surface oxide films that can cause system failure in low voltage and high frequency applications, especially systems which have expected service lives on the order of years. Improvement of tribological performance in gold through ion beam modified and composite structures is reviewed and implications for e-beam physical vapor deposition seem promising based on the factors of film purity, structure and precision of gold deposition.

Pure coarse grained gold is a highly ductile and malleable metal that under contact stresses in tribological systems easily deforms and allows the plated surface to conform to the opposing body. In self-mated contacts of soft gold, the high ductility results in a large area of real contact of deforming surface asperities leading to high friction and wear due to adhesion[3]. For contacts composed of dissimilar metals in which only one surface is gold plated, the relatively low yield stress of gold favors material transfer from the gold plated surface to the counterface resulting in a self-mated contact. Sliding friction between engineered surfaces that are relatively smooth is a function of the interfacial shear stress, and in the case of clean gold surfaces results in repeated cold welding and ductile fracture at asperity junctions[4]. To mitigate the frequency of adhesive welding and ductile failure of asperities, gold is alloyed with small amounts, typically (1-2 wt%), of cobalt or nickel, referred to as hard gold, to increase the plating hardness and thus reduce the real area of contact

between asperities[5]. The dominant factor determined by Lo et. al. for the increase in hardness of gold alloyed by small amounts of cobalt or nickel is grain refinement and Hall-Petch strengthening[6]. The increase in hardness in nickel and cobalt hardened gold reduces the observed cycles to failure but quantitative values of wear have not been determined for many contact pairs[7]. The reduction of real contact area in hard gold results in a smaller cross-sectional area for electrical conduction increasing the constriction resistance between contacting bodies that for a single asperity contact is proportional to the sum of the bulk resistivity of each material and inversely proportional to the contact radius[8]. This loss in electrical contact performance is typically less significant than the improvements in friction and wear response in hard gold plating, and has led to the widespread use of hard gold in the electronics industry.

Hard gold plating used in tribological electrical contacts can be deposited in a number of ways including galvanic or electroless plating, sputter deposition, electron beam evaporation, and pulsed laser deposition. However the most widely implemented technique for mass production driven by the emergence of the electronics industry in the 1940s is electroplating[9]. The typical bath solution for depositing hard gold electroplate utilizes gold potassium cyanide [$KAu(CN)_2$] as a gold source[9, 10]. In the interest of environmental factors other substitutes for gold sources to replace cyanide and arsenic based solutions including gold(I) sulfite $[Au(SO_3)_2]^{3-}$ and gold(I) thiosulfate $[Au(S_2O_3)_2]^{3-}$ complexes have been re-investigated [11] . Electroplating of hard gold in addition to incorporating nickel or cobalt precipitates at grain boundaries results in the inclusion of other elements found in the bath solution. In the case of cobalt hardened gold deposited in a cyanide bath, Okinaka has found

inclusions of O, K, and N to be in the range of 1-2 at%, C at approximately 4 at%, and H as high as 7 at%[12]. Okinaka also compiled data that shows an increase in hardness with increasing C content for cyanide bath deposited hard gold, but for thiosulfate depositions a decrease in hardness with the increase in ligand concentration of $[S_2O_3^{2-}] + [SO_3^{2-}]$[12]. Electroplating inherently incorporates inclusions many of which are difficult to characterize and could be detrimental to mechanical and tribological performance. Current ASTM Standard Specification B488-11 defines type I,II, and III gold platings as 99.70, 99.00, and 99.90 wt% Au respectively but excludes K, C and N from the calculation[13]. Other imperfections introduced into the plating include micro porosity which is dependent on deposition parameters such as current density and efficiency and hydrogen evolution in the bath[14].

One of the shortcomings in hard gold platings used for low voltage applications is the formation of surface metal oxides. A surface film of metal oxide only a few monolayers thick can increase the electrical contact resistance several orders of magnitude[15]. Furthermore thin metal oxide films are typically more brittle and easily fracture under tribological contact producing hard third body abrasive wear debris that can accelerate wear rates. Diffusive mass transport of the plated substrate material results in the surface accumulation of an oxide film in oxygenated atmospheres. A commonly hard gold plated material is copper due to its high conductivity and lower economic cost. However the gold copper system results in high rates of interdiffusion and surface accumulation of copper on the order 10-65 Å in 5 days at temperatures in the range of many electronics applications of 100 and 125ºC[16]. Also reported in this study was the change of electrical contact resistance which varied by four orders of magnitude in the same time period at 125ºC[16]. To prevent substrate material

diffusing to the surface, as well as to increase adhesion and wear resistance, a nickel underlayer film on the order of 1-5 µm thick is commonly deposited beneath the gold electroplate. Although it has been found that nickel is a suitable diffusion barrier for copper, it cannot completely prevent itself from diffusing through gold to form surface oxides over extended time periods[17]. Cobalt in cobalt hardened gold has also been shown to diffuse to the surface and form surface oxides. Tompkins aged 0.26 wt% cobalt hardened electroplated gold at 100 and 150ºC for 250 and 122 days, respectively and found a cobalt oxide thickness of approximately 10 and 55 Å[18]. The detrimental effects to contact resistance in 0.25 wt% cobalt hardened gold were confirmed by Antler and showed to increase by an order of magnitude in 100 hours at 200ºC and a similar although slower change in 0.25 wt% nickel hardened gold was observed[15].

1.2.2 Ion Implantation for Au Tribological Improvement

Investigations of ion implantation into gold were first driven to understand the formation of helium bubbles from tritium decay and alpha radiation in reactor containers. However few studies have been aimed at evaluating the tribological and surface effects of implantation in gold. One study by Robic et. al. evaluated the stress, hardness, and wear resistance of gold implanted at 100 and 200 keV with ions of He, Ne, Ar, and B with doses up to $3x10^{17}$ cm^{-2} [19]. In this study it was found that the integrated lateral stress in gold increased proportional to the dose up to 10^{13} cm^{-2} after which it increased as the square root of dose until saturating at approximately 10^{16} cm^{-2} for each ionic species except He in which it remained proportional. Also reported is approximately a 35% increase in Knoop hardness for B implantation that did not correlate with the rate in change of lateral stress, however He results

were not reported. Although wear experiments were conducted the counterface material chosen was a rubber pin and the measurement of wear resistance was not conducted in quantitative manner[20]. Another study by Leech investigated N_2^+ ions implanted at 100 keV and $2x10^{17}$ cm^{-2} in Au8Ag, Au26Ag3Ni, and Au30Pd29.5Ag1.55Sn alloys found a significant reduction and more stable coefficient of friction as well as a 13% increase in Knoop hardness[21]. Leech also reported no significant change in electrical contact resistance as a result of N implantation.

1.2.3 Au-Oxide Composites For Improved Tribological Performance

The interest in higher temperature applications of gold where retention of hardness and resistance of surface oxide formation are desirable has led to the investigation of several oxide dispersion strengthened composites. Initial work done by Hill studied hardness, resistivity, and wear of 1.0 vol% inclusions of Al_2O_3, Y_2O_3, TiO_2, and CeO_2 prepared by powder metallurgy techniques[22]. Hill reported approximately a 16% increase in hardness which was retained after 600ºC anneal as well as a 50% reduction in mass loss during wear measurements for each oxide except Al_2O_3 which showed minimal improvement[22]. More recent work conducted by Argibay et. al. investigated the wear, electrical contact resistance and friction of Au-ZnO nanocomposite films in a range of 0.1-28.0 vol% ZnO prepared by e-beam deposition. Linear wear measurements against a Neyoro G gold alloy rider were found to be unmeasurable for both 2.0 and 28.0 vol% ZnO after 1000 cycles but a specific wear rate of the rider was reported to be $4.3x10^{-8}$ mm^3-$(N-m)^{-1}$[23]. Also reported was a significant reduction in grain size of the films for just 0.1 vol% ZnO characterized by a bimodal distribution with an out of plane <111> texture and no in plane texture[23]. This reduction in grain size is attributed as the cause for

the unmeasurable wear rate reported and is thought to be increasing the hardness via Hall-Petch strengthening for gold as shown by Lo et al.[6].

The oxide dispersion strengthened gold composites of 1.0 vol% investigated by Hill were also measured for electrical resistance over a range of temperatures from 0-905ºC. The correlation of resistance to temperature was shown to increase linearly as was the pure gold specimen with only a few percent increase of resistance over that of gold[22]. Argibay et. al. also evaluated the electrical contact resistance during sliding of 2.0 and 28.0vol% ZnO and found a single minimal increase but more steady state ECR for 2.0 vol% ZnO over that of pure deposited gold but an increase of four orders of magnitude for 28.9 vol% ZnO. The increase in ECR by four order of magnitude for 28.9 vol% ZnO did not correlate with the measured increase in resistivity of the film which only increased by one order of magnitude over the 0.1 vol% ZnO film. Also characterized was the "chatter" or ECR values greater than 1 Ω during 100 sliding cycles and reported for 2.0 vol% ZnO that chatter can begin in the first few cycles and is attributed to contact separation by ZnO wear debris in the sliding track[23].

1.3 Dissertation Overview

In light of the widespread use of electroplated hard gold in the electronics industry, and the human safety and environmental concerns involving its production method, this study is aimed at investigating a clean physical vapor deposition (PVD) technique, electron beam (e-beam) evaporation in vacuum, to deposit Au containing thin electrical contact films. Based on the review of current hard Au platings low temperature aging issues with surface oxide formation two processing methods will be investigated based on the assumption that they will

have no chemical potential with O_2 in ambient air to drive diffusion and segregation to the surface air interface. These methods include investigating noble gas ion implantation into e-beam Au gold and Au-ZnO codepostion to produce stable nanocrystalline Au grain structures during thermal exposure and under sliding electrical contacts. This dissertation investigates the processing-structure-tribological-electrical property relations of these films. Chapter 1 gives a broad introduction of the uses of sliding electrical contact films and review of the current use, strengthening mechanisms, and electrical contact resistance phenomenon of commercial "hard gold" and Au-oxide composites as a motivation for the development of new processing methods and materials. Chapter 2 gives a theoretical overview of quintessential published work regarding sliding metal tribology and electrical contact resistance that is relevant to understanding the interdisciplinary nature of studying tribological electrical contact materials. Chapter 3 describes the methods and experimental techniques implemented in this study. Chapter 4 presents the results and discussion of the investigation of noble gas ion implantation for use in Au sliding ECR films. Chapter 5 presents the results and discussion of the investigation of Au-ZnO codeposited films. Chapter 6 provides a summary of the dissertation and includes an outline of the major conclusions from this body of work as well as recommendations for future work and research in this area.

1.4 Chapter 1 References

1. Hageluken, C. and C.W. Corti, *Recycling of gold from electronics: Cost-effective use through 'Design for Recycling'.* Gold Bulletin, 2010. **43**(3): p. 209-220.
2. Goodman, P., *Current and future uses of gold in electronics.* Gold Bulletin, 2002. **35**(1): p. 21-26.
3. Pashley, M.D., J.B. Pethica, and D. Tabor, *Adhesion and micromechanical properties of metal surfaces.* Wear, 1984. **100**: p. 7-31.

4. Antler, M., *Sliding wear of metallic contacts.* IEEE Transactions on Components, Hybrids, and Manufacturing Technology, 1981. **4**(1).
5. Antler, M. *Plated coating for electric contacts*. in *The Role of Coatings in the Prevention of Mechanical Failures, Proc. of the 23rd Meeting of the Mechanical Failures Prevention Group*. 1976. U.S. National Bureau of Standards.
6. Lo, C.C., J.A. Augis, and M.R. Pinnel, *Hardening mechanisms of hard gold.* Journal of Applied Physics, 1979. **50**(11): p. 6887-6891.
7. Antler, M., *Tribological Properties of Gold for Electric Contacts.* IEEE Transactions on Parts, Hybrids, and Packaging, 1973. **9**(1): p. 4-14.
8. Holm, R., *Electric Contacts: Theory and Application, 4th Edition*. 1967, New York: Springer-Verlag.
9. Christie, I. and B. Cameron, *Gold electrodeposition within the electronics industry.* Gold Bulletin, 1994: p. 12-20.
10. Chrzanawski, W., Y.G. Li, and A. Lasia, *Study of a mechanism of hard gold electrodeposition.* Journal of Applied Electrochemistry, 1996. **26**: p. 385-396.
11. Kato, M. and Y. Okinaka, *Some recent developments in non-cyanide gold plating for electronics applications.* Gold Bulletin, 2004. **37**: p. 37-44.
12. Okinaka, Y., *Significance of inclusions in electroplated gold films for electronics applications.* Gold Bulletin, 2000. **33**(4): p. 117-127.
13. *Standard Specification for Electrodeposited Coatings of Gold for Engineering Uses*. 2011, West Conshohocken, PA: ASTM International.
14. Liu, Z., et al., *Effect of Morphology and Hydrogen Evolution on Porosity of Electroplated Cobalt Hard Gold.* Journal of The Electrochemical Society, 2010. **157**(7): p. 411-416.
15. Antler, M., *Gold-Plated Contacts: Effect of Thermal Aging on Contact Resistance.* Plating and Surface Finishing, 1998. **85**(12): p. 85-90.
16. Tompkins, H.G. and M.R. Pinnel, *Low-temperature diffusion of copper through gold.* Journal of Applied Physics, 1976. **47**(9): p. 3804-3812.
17. Pinnel, M.R., *Diffusion-Related Behaviour of Gold in Thin Film Systems.* Gold Bulletin, 1979. **12**: p. 62-71.
18. Tompkins, H.G., *Diffusion of Cobalt out of Cobalt-Hardened Gold Measured with Auger Electron Spectroscopy.* Journal of The Electrochemical Society, 1975. **122**(7): p. 983-987.
19. Robic, J., J. Piaguet, and J. Gailliard, *Some measurements of hardness, wear and stresses in ion implanted thin metallic films.* Nuclear Instruments and Methods, 1981. **182**: p. 919-922.
20. Robic, J.Y., J. Piaguet, and J.P. Gailliard, *Some measurements of hardness, wear and stresses in ion implanted thin metallic films.* Nuclear Instruments and Methods, 1981. **182-183**: p. 919-922.
21. Leech, P.W., *The effect of nitrogen implantation on the tribological properties of gold-based alloys and electroplated palladium.* IEE Transactions on Components, Hybrids, and Manufacturing Technology, 1988. **11**(1): p. 16-21.
22. Hill, J.S., *Dispersion-strengthened gold.* Gold Bulletin, 1976. **9**(3): p. 76-80.
23. Argibay, N., et al., *Wear resistant electrically conductive Au-ZnO nanocomposite coatings synthesized by e-beam evaporation.* Wear, 2013. **302**: p. 955-962.

CHAPTER 2

THEORETICAL OVERVIEW OF SLIDING METAL TRIBOLOGY AND ELECTRICAL CONTACT RESISTANCE

This chapter aims to provide the reader with a condensed review of fundamental and classical research relevant to understanding the various interactions that occur in sliding electrical contacts.

2.1 Tribology

2.1.1 Contact Mechanics and Nature of Surfaces

The science of contact mechanics originated with Hertz's 1882 publication [6] describing the elastic deformation of solid spheres as a function of normal force, and the resultant contact area. Others have further developed Hertzian mechanics to predict elastic stress distributions into the subsurfaces for various contact geometries, with a very valuable treatise provided by Johnson [8]. From Hertzian analysis of shear stress in a flat body in a static line contact with a cylinder, it can be seen that point of max shear is in the subsurface shown by the isolines of shear in Fig. 2.1a. This contact also results in a compressive stress inside the contact area with the surfaces outside of the contact experiencing surface tractions in tension. Similarly for a line contact in sliding with a coefficient of friction of 0.2, shown in Fig. 2.1b, the point of maximum shear remains in the subsurface but moves closer to the surface and to a zone in front of the sliding contact. With increasing values of coefficient of friction to a value of 0.3 the point of maximum shear occurs at the surface of the flat body. The surface stresses also shift, with a fully compressive stress in front of the sliding cylinder and tension in the trailing side.

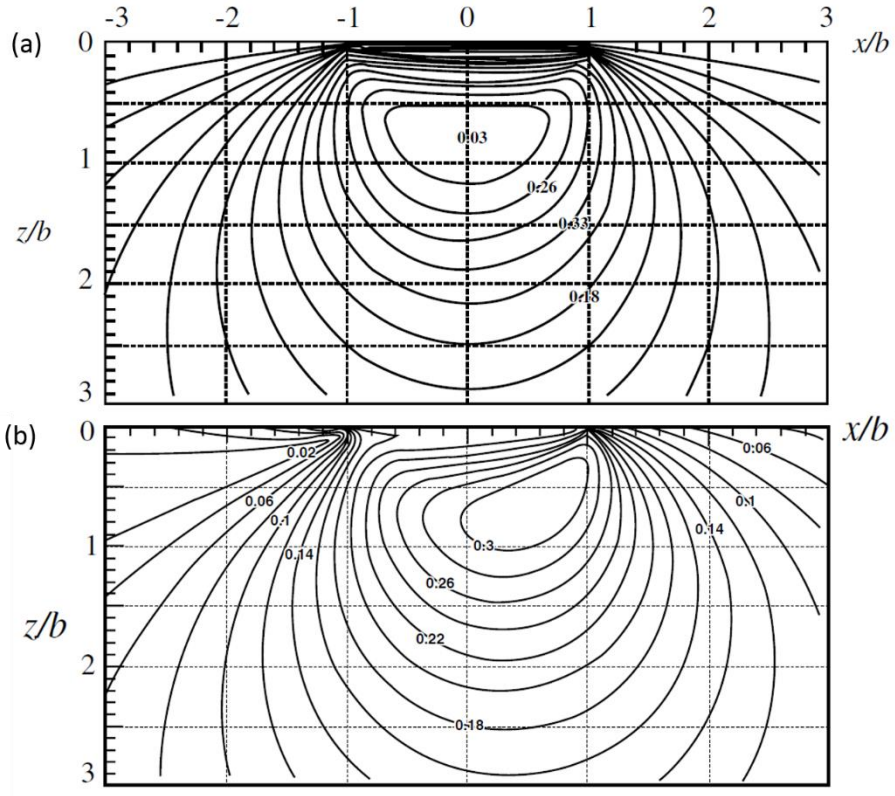

Fig. 2.1: (a) Contours of maximum shear stress normalized by Hertz stress for a line contact in a material with ν = 0.3, and (b) contours of principle shear stress beneath a sliding line contact with a coefficient of friction = 0.2 [5].

Based on the Hertzian analysis, contact area of elastically deformed bodies was assumed to follow the proportionality of $A \propto N^{2/3}$, where A is contact area, and N is normal force. However this ideal elastic description of contact area depends upon the assumption that the contacting surfaces are perfectly smooth. A fundamental aspect of contact mechanics of engineered materials is that at the interface of two contacting rigid solids there is a large disparity in the magnitude of the apparent (A_a) area and real (A_r) area of contact. This disparity arises from the fact that engineered, and natural, surfaces are imperfect and are comprised of microscopic scale roughness features, protrusions referred to as asperities, often coinciding with a more macroscopic scale surface waviness, or kerf, and direction or lay that is shown

schematically in Fig. 2.2. In 1939 Bowden and Tabor [9] gave experimental evidence through electrical resistance measurements on crossed cylinders that the A_r of contact as a function of normal load between metal surfaces was 10^2 to 10^5 times less than the apparent area of contact. The first direct observation of the phenomenon was conducted by Dyson and Hirst [10] between steel balls and metallized glass surfaces by phase contrast microscopy and revealed that for various surface preparations the real area of contact was restricted to clusters of asperities with increasing area and number for increased load. The observed distribution of the contacting asperities also hinted to the importance of the more macroscopic surface features, e.g. waviness or kerf created by lapping and polishing processes, on the clustering of contacts. Others experimental work on contact resistance between mated metals is summarized by Holm [11], in which he suggests the interface is supported by a few asperity contacts that must be plastically deforming even when the Hertzian contact stress calculated by

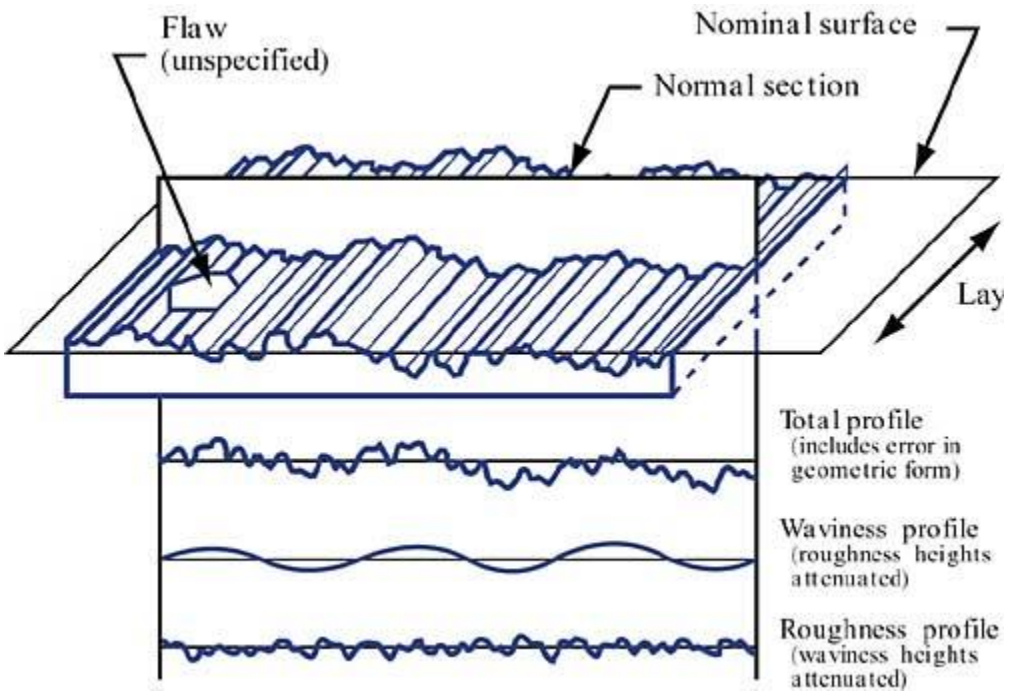

Fig. 2.2: Schematic of surface topographical parameters at varying scales, including waviness, lay, and roughness [2].

the A_a would result in an elastic contact pressure below the yield strength of the weaker material.

Experiments of the mechanics of sliding metal contacts during the 1950's led to Archard and Hirst publishing work that contradicts the concept that the A_r of contact by asperities invariably results in their plastic deformation and provides experimental evidence that for low normal contact forces some metallic surfaces will wear during sliding and become smoother, leading to an elastic contact condition [12]. Archard went on to publish a mathematical model [13] showing that for an idealized rough surface containing a series of spherical asperities superimposed on a larger series of spherical height variations brought into contact with a flat rigid half-space, that as load is increased asperities in contact would deform elastically resulting in more asperities coming into contact, yielding a linearly proportional relationship between

normal load and A_r. Expanding on the concepts of Archard, Greenwood and Williamson provided a model of nominally flat contacts where the surface roughness is modelled by the use of statistical parameters derived from surface topography measurements to predict the transition from elastic to plastic deformation [14]. In this publication, they presented evidence suggesting that typical surface roughness variations can be well described by a Gaussian distribution and provided an expression for a non-dimensional parameter, called the index of plasticity given in Eq. 2.1, that includes material properties of both contacting materials and statistical surface topographical data to estimate the transition from fully elastic to plastic asperity deformation.

$$\Psi = \frac{E'}{H}\sqrt{\frac{\sigma}{\beta}} \tag{2.1}$$

This expression in Eq. 2.1 is a function of the reduced elastic modulus for the two materials, *E'*, the hardness of the softer material in contact, *H*, the standard deviation in the relative surface height distributions, σ, and the average radius of curvature of surface asperities β. *For* values of $\Psi < 0.6$ a predominantly elastically deforming asperity contact of the surfaces is predicted, excluding a few extremely high contact pressure asperities. In the range of $0.6 < \Psi < 1.0$ the contact regime is described as being in a transition region where deformation cannot be clearly ascribed to be predominantly elastic or plastic, and for $\Psi > 1.0$ the asperities of the softer material are expected to be mostly plastically deforming, leading to increased contact area. The reduced modulus of the contacting materials, *E'*, is given in Eq. 2.2, with subscripts denoting arbitrarily the contacting bodies, and is dependent on their respective elastic moduli, *E*, and Poisson's ratio, *v*.

$$E' = \left(\frac{1-\nu_1^2}{E_1} + \frac{1-\nu_2^2}{E_2} \right)^{-1} \tag{2.2}$$

From the above brief review adapted from quintessential publications of contact mechanics and the nature of surfaces a few fundamental concepts can be summarized as below.

1) The point of maximum shear in static and sliding contacts of smooth surfaces is in the subsurface except when the coefficient of friction is greater than 0.3.
2) The real area of contact between nominally flat metal contacts is dependent on material properties of elastic modulus and hardness, as well as the surface roughness, asperity distribution, and the applied normal force.
3) The real area of contact between engineered materials consists of a number of contacting asperities dispersed across the surfaces resulting in a real contact area that is $10^2 – 10^5$ times less than the projected apparent area.
4) A non-dimensional parameter called the index of plasticity can provide a prediction of the deformation regime of the contacting asperities as a function of the materials elastic moduli, Poisson's ratio, hardness, and surface topography parameters; however, it does not include the applied normal force.
5) Some metallic surfaces can start in a regime of predominantly plastically deforming asperities, but through wear processes achieve a smoother and more conformal contacting interface leading to a predominantly elastic contact.

2.1.2 Sliding Friction

Kinetic friction is the term used to describe the resistance of motion between two contacting bodies in relative tangential motion and arises from non-conservative forces that

convert kinetic energy into internal energy, e.g. heat, of the bodies and surrounding environment [15]. The first published work providing an expression for the coefficient of friction, Eq. 2.3, was given in 1699 by Amontons [16], where F is the friction force, μ is the coefficient of friction, and N is the normal force. Amontons developed this relation by experiments on sliding blocks and made the assertion that the friction force was independent of the contact area. This relationship and the assumption that F is independent from contact area is known as Amontons' law.

$$F = \mu N \tag{2.3}$$

This relationship is still in use today as the basis for calculating the kinetic coefficient of friction as F and N are both easily measurable experimental variables. The value of the coefficient of friction, however, must be determined empirically as it is not a materials property, but rather a 'systems property' that is dependent on the materials in contact and conditions such as temperature, contact force, sliding velocity, surface chemical reactions, and environmental factors such as humidity. These influencing factors on friction operate across all length scales, from atomistic, for example oxide diffusion in the surface, to microscopic in the case of surface roughness and asperity interaction, to macroscopic geometry and loading conditions.

In attempts to relate friction to the Hertzian contact area, Adam [17] was the first to publish that a consequence of the linear relationship between friction and normal force of Amontons' law, and the Hertzian contact area proportionality with normal force, leads to the prediction that the friction force should be proportional to the contact area by, $F \propto A_r^{3/2}$. A further development in relating the coefficient of friction to more microscopic interfacial

properties came from Bowden and Tabor's classical theory of adhesive friction [18], expressions of which are given in Eq. 2.4. This theory considers the frictional force as a result of the product of the real contact area and the shear strength (τ), and by treating the normal force over the real area as representative of the mean Hertzian contact pressure (P_H), relates the coefficient of friction to the interfacial shear strength (τ_0) and a constant α representing the pressure dependence of the shear strength. The constant α is the lowest obtainable friction coefficient for a given sliding tribocouple for all other factors minimized.

$$\mu = \frac{A_r \tau}{N} = \frac{\tau}{P_H} = \frac{\tau_0}{P_H} + \alpha \tag{2.4}$$

Also shown for a Hertzian elastic sphere against a flat elastic half space, the friction coefficient can be related to the materials' reduced modulus according to the expression given in Eq. 2.5, where R is the radius of the sphere.

$$\mu = \tau_0 \pi \left(\frac{3R}{4E'} \right)^{2/3} N^{-1/3} + \alpha \tag{2.5}$$

According to this Hertzian analysis by Bowden and Tabor, the coefficient of friction is predicted to be proportional to the normal force by $\mu \propto N^{-1/3}$. This result differs from Amontons' law of a linear dependence and predicts that while contact deformation remains elastic the coefficient of friction will significantly decrease for increasing normal force. This non-Amontonian friction behavior has been observed for many engineered solid lubricant coatings including diamond-like nanocompsite (DLN), and composite MoS_2/Sb_2O_3/Au coatings in both humid and dry nitrogen environments [19].

Although the friction models presented above have been shown to model the friction behavior of hard coatings and lightly loaded elastic contacts fairly well, due to the rough

topography of metallic surfaces leading to contact at asperities experiencing a high degree of plasticity, metallic friction is more difficult to model. At the asperity scale three predominant mechanisms effect the coefficient of friction, and are shown schematically in Fig. 2.3. They include adhesion which occurs for asperities pressed into contact by either pure normal force or combined normal and tangential force, ploughing from hard third body debris, work hardened wear debris, or hard asperities, and asperity plastic deformation during sliding. A simple model of the effect of plowing of a hard asperity is provided by Rabinowicz [20] by treating the asperity as a cone displacing material on its inclined face as it slides through the metal. This expression is given in Eq. 2.6, where μ_p is the component of friction due to plowing, F_p is the friction force of plowing, r is the normal contact area radius, θ is the angle between the surface and the inclined face of the cone, and p is the compressive strength of the metal.

$$\mu_p = \frac{F_p}{N} = \frac{\left(r^2 \tan\theta\right)p}{\pi r^2 p} = \frac{\tan\theta}{\pi} \tag{2.6}$$

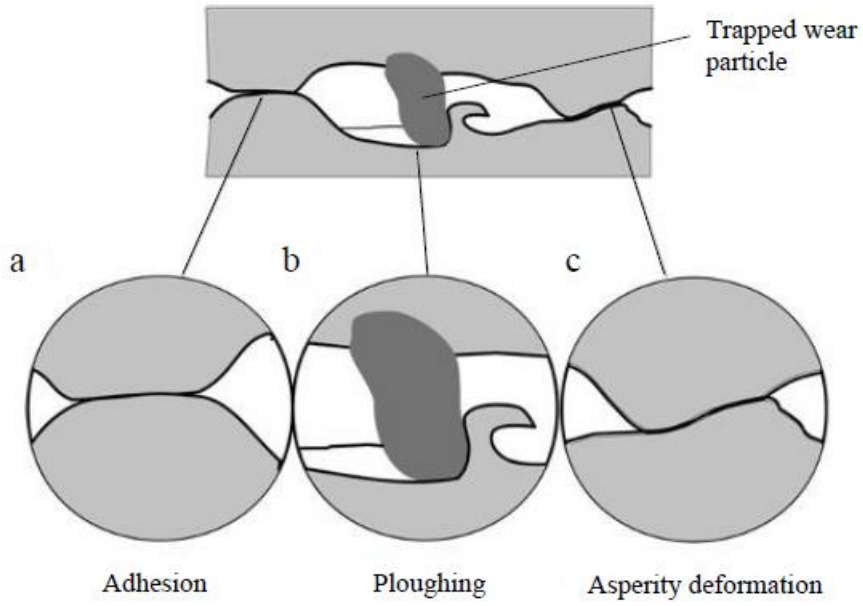

Fig. 2.3: Schematic showing the three asperity scale components of sliding friction, for (a) adhesion, (b) ploughing, and (c) asperity deformation [4].

This model assumes that the asperity in contact is perfectly rigid and cuts the softer metal at the full depth of its penetration into the surface. Further developments of asperity level friction incorporated the adhesion contribution originally proposed by Bowden and Tabor with plowing contributions of a flat tipped conical asperity. The interpretation assumes that asperities in contact are influenced by adhesion, and under normal pressure the asperities flatten and contact increases as asperity tips flatten, resulting in junction growth. These models have been summarized well in the expression from Blau [21] given in Eq. 2.7, where μ_i is the friction coefficient of the cone against the material flowing across its face.

$$\mu = \left(\frac{\tau}{N}\right)\left(\pi r^2\right) + \mu_i \cos^2\theta + \frac{\tan\theta}{\pi} \tag{2.7}$$

These models highlight the high dependence of sliding friction on the adhesive contribution due to the softer metal plastically deforming at asperity junctions, increasing the real contact area and leading to greater adhesive friction.

Metallic friction is also dependent on the structures of the subsurface, especially the grain size and its evolution during sliding. The classical studies on metallic friction by Rigney and Hirth [22] revealed that other non-conservative forces contributing to friction are correlated to the amount of heat lost in the bulk due to plastic deformation as well as the stored energy in the plastically deformed zones of the softer metal. The deformed zones in the subsurfaces of the softer metal can however lead to reduced friction. In studies of sliding friction against nanocrystalline Ni, Prasad et. al [23] found contact pressure and sliding velocity regimes in which a stable low friction condition could be established with the retention of a nanocrystalline near surface zone. Similar results have been observed for nanocrystalline

coatings of Ni [24], and nanocrystalline surface structured Cu [25]. These low metallic friction conditions are theorized to be dependent on shear rate accommodation of the nanocrystalline zone providing easy slip in a confined zone by a transition from dislocation mediated deformation to grain-boundary sliding mediated deformation. A first principles expression of the shear rate accommodated by grain boundary sliding is given by Raj and Ashby [26], and denoted in Eq. 2.8, where τ is the local shear stress, Ω the atomic volume, k the Boltzmann's constant, T is the temperature, d is the grain size, δ is the width of the grain boundary diffusion path, D_{gb} is the grain boundary self-diffusivity, and D_{bk} is the bulk self-diffusivity.

$$\dot{\gamma} = \tau \frac{160\Omega}{kT} \frac{1}{d^2} \left(1 + \frac{\pi\delta}{d} \frac{D_{gb}}{D_{bk}} \right) D_{bk} \tag{2.8}$$

This relation implies that the grain boundary sliding accommodated deformation is only a significant contribution to shear accommodation for very small grains sizes, on the order of 20 nm or less. However if the right conditions and friction induced structures are stable, this phenomenon can significantly reduce friction of otherwise highly adhesive metal friction.

2.1.3 Wear Mechanisms of Sliding Contact

Wear is in general defined as the removal of material from solid surfaces as a result of relative motion of bodies in contact, but as described by Antler [27] can also include the plastic flow and dimensional change of a surface. There is a large volume of texts and publications dedicated to the review of known wear mechanisms. A few recommended texts on the subject of wear include *Engineering Tribology* [28], *Wear: Materials, Mechanisms and Practice* [29], and *Principles and Applications of Tribology* [30]. It is important to state that, similar to fiction, wear is a 'systems property' and dependent on the materials in the tribocouple, the

environmental conditions, and the operating conditions such as normal force and velocity. In the case of sliding contact wear of metals, the list of predominant wear mechanisms resulting in mass loss can be shortened to abrasion, adhesive transfer, and fatigue delamination. Abrasion can occur due to hard asperities sliding against a softer metal resulting in the ploughing and cutting of the surface, and can also occur due to harder third body debris and work hardened debris trapped in the interface. Adhesive transfer is especially common in bare metal sliding contacts and results in mass loss from a surface when the adhesive junction strength is greater than the cohesive strength of the weaker material. Fatigue delamination wear is well described by Suh [31] as occurring in the following steps during initial wear:

1. Initial asperity deformation of the softer material leads to a smoothing of the contact such that the contact area increases and approaches a planar contact of the softer surface with the asperities of the harder surface.
2. Further sliding of the harder asperities on the softer surface induces shear deformation with increasing plastic strain accumulation.
3. As subsurface deformation continues, cracks are nucleated at zone interfaces of different wear structures and grain boundaries.
4. Further loading and deformation causes the cracks to extend and propagate, typically parallel to the surface, and eventually connect to neighboring cracks.
5. Eventually at specific weak positions these cracks shear to the surface resulting in a "sheet" of material that can be delaminated.

Although there are many mechanisms to wear, the aforementioned mechanisms and their processes are the dominant modes of wear applicable to sliding electrical contact materials.

2.2 Electrical Contact Resistance

When two electrical conductors are in contact and the flow of current is constrained to the asperity junctions, this depends partially on the real area of contact between bodies discussed in section 2.1.1. In general it is difficult to develop accurate models or predictions of contact resistance in sliding electrical couples at the macro scale due to complexities such as evolving topography and contact area due to wear, chemical changes at the surface such as oxide films, and the presence of other outside contaminants or liquid lubricants. However, as described by Holm [11], contact resistance (R) in a metal-metal junction is a function primarily of the constriction resistance (R_c) and the film resistance (R_f), given in Eq. 2.9.

$$R = R_c + R_f \tag{2.9}$$

The following subsections are included to discuss the phenomena of constriction resistance, which arises when electric current is constrained at the interface to the real area of contact, and to film resistance which is primarily a result of electrically insulating oxides or other non-conductive surface films.

2.2.1 Constriction Resistance

The measurement of contact resistance between crossed metal cylinders was the first method by which the vast difference between the apparent and real area of contact was elucidated. According to Bowden and Tabor [9], the first demonstration of the discrepancy between the contact resistance and the apparent area of contact of metal junctions is attributed to Binder [32], who showed contact resistance was higher than that expected for the entire apparent area of contact.

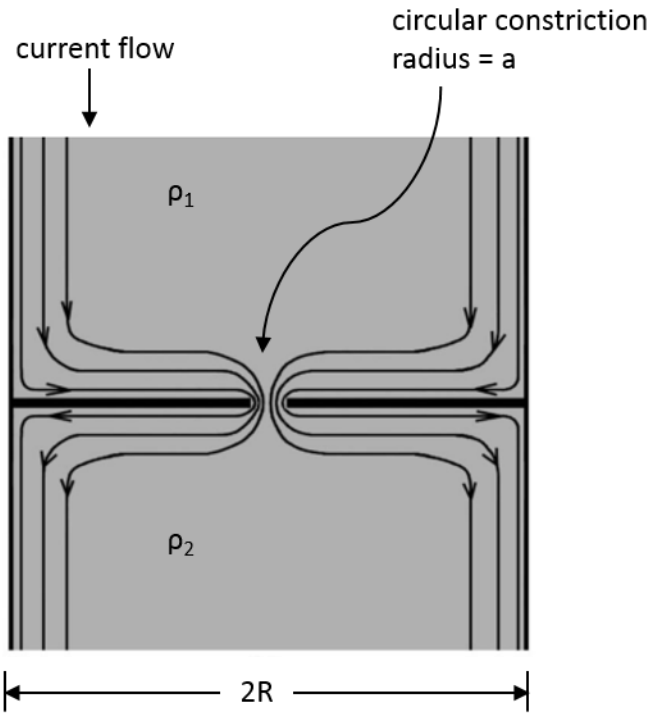

Fig. 2.4: Schematic of electrical resistance through a circular constriction, adapted from [3].

A useful overview of the fundamental concepts of electrical contact resistance discussed in this section is given by Timsit [7]. Starting with the simple case of electrical current being constrained to a circular constriction area between two conductive half-spaces, as shown in Fig. 2.4, allows for the derivation of a simple and commonly implemented expression of constriction resistance given in Eq. 2.10, from Holm [11].

$$R_c = \frac{\rho_1 + \rho_2}{4a} \tag{2.10}$$

This expression provides constriction resistance as a function directly proportional to the sum of the bulk resistivity of each half space (ρ_1 and ρ_2, in units of Ω-m) and inversely proportional to the circular constriction radius.

Although Eq. 2.10 is a useful expression for a single asperity contact, for practical engineered surfaces with Gaussian distributions of asperity and valley heights a large number of

asperities are in contact at the microscale, including point contact geometries of a sphere on flat configuration. When current is passing through neighboring asperity contacts in a rough contact, mutual electrostatic interaction between electrons flowing in close proximity can increase the constriction resistance. This effect is even more pronounced for a tight cluster of neighboring asperities in contact. Greenwood [33] developed an analytical expression, given in Eq. 2.11, formulated by expanding on Holm's classical model [11] defining the Holm radius (α) given in Eq. 2.12, which is a characteristic radius of the statistical spatial distribution of asperities in a cluster, and including statistical distribution of real asperity contacts of varying diameter. In the expression Eq. 2.11, ρ is the average resistivity of the conductors in contact, n is the number of asperities, $\bar{a}$ is the average asperity radius, and α is used as the statistical interaction distance. The Holm radius is defined in Eq. 2.12 as a function of the two dimensional separation distance (s_{ij}) and number of contacting asperities.

$$R_c = \frac{\rho}{2}\left(\frac{1}{n\bar{a}} + \frac{1}{\alpha}\right) \tag{2.11}$$

$$\alpha^{-1} \equiv \frac{3\pi}{16n^2}\sum\sum\frac{1}{s_{ij}} \tag{2.12}$$

Although Eq. 2.11 is rooted in a fantastic analysis of the real area of contact and electrostatic interactions of electrons, it is relatively intractable to apply in a real macroscopic sliding electrical contact as the topography, and even the resistivity, can continuously change due to wear processes.

2.2.2 Film Resistance

The second primary source of contact resistance, and arguably the more difficult to model, according to Holm is film resistance. Film resistance arises from nonconductive films on

the surface of metals, which are typically oxides formed from exposure to air, known as native oxides. The bulk resistivity of oxides is in general orders of magnitude greater than that of pure metals. For example, a typical engineering conductor material Cu has a bulk resistivity, $\rho \sim 1.7 \times 10^{-8}$ Ω-m [34], while its cuprous oxide from, Cu_2O, which readily forms at low temperatures has a bulk resistivity 12 orders of magnitude greater with a value of $\rho \sim 5 \times 10^{4}$ Ω-m. Although native oxides on metal surfaces are quite ubiquitous for many metals, their thickness is often on the order of single of nanometers due to self-passivation and allows for current to flow through them via the phenomenon of electron tunneling.

The growth rate of metal oxide films at relatively low temperatures has been postulated by the classical work of Mott [35] and Fehlner & Mott [36] to be logarithmic in nature, with an increase in rate at elevated temperatures to a parabolic form. This logarithmic limiting oxidation rate of single crystal Cu surfaces was demonstrated by extensive experimental work by Young et al. [37] in a pure oxygen atmosphere and at a temperature of 70°C. The limiting behavior and passivation is a result of the increased diffusion pathway as the oxide film grows.

For two contacting metal asperities both containing relatively thin oxide films, there are two possible conduction pathways. If the contact stress between the asperities is great enough to cause fracture of the native oxide layer, thus exposing bare metal to metal contact, then conduction may occur and be subject to constriction resistance according to the discussion in the previous section. If the native oxide films remain continuous in a lightly loaded contact, and is sufficiently thin, then the electron conduction pathway will be through tunneling. A simple but useful expression of the contact resistance due to film tunneling is given by Holm [11] and denoted in Eq. 2.13.

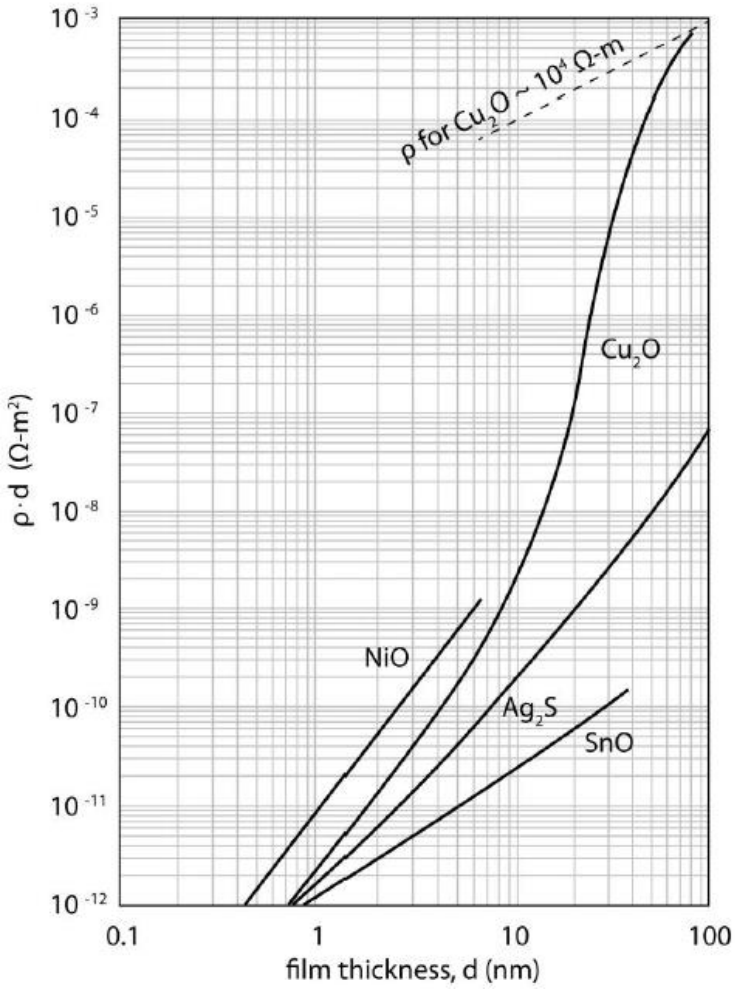

Fig. 2.5: Variation in tunneling resistivity vs oxide film thickness for various metal-oxide junctions, from [1] adapted from data from Timsit [7].

$$R_f = \frac{\rho}{2a} + \frac{\sigma}{\pi a^2} \tag{2.13}$$

The tunneling contribution to film resistance is a function of the metal bulk resistivity (ρ), the tunneling resistivity (σ) in units of Ω-m^2, and the asperity contact radius (a). A plot of the change in tunneling resistance with increasing oxide film thickness is shown in Fig. 2.5. This plot highlights that for very thin native oxide films, less than 1 nm, the tunneling resistance is not a significant factor, but for oxide films of greater thickness the contribution to overall contact resistance can be larger than 95% of the overall ECR.

2.5 Chapter 2 References

1. Argibay, N., *Low wear metal sliding electrical contacts*. 2011: University of Florida.
2. ASME-B46.1-1995, *Surface Texture: Surface Roughness, Waviness, and Lay.* New York: American Society of Mechanical Engineers, 1996.
3. Timsit, R.S., *Constriction resistance of thin film contacts.* Components and Packaging Technologies, IEEE Transactions on, 2010. **33**(3): p. 636-642.
4. Holmberg, K. and A. Matthews, *Coatings Tribology: Properties, Mechanisms, Techniques and Applications in Surface Engineering 2nd ed.* Tribology and Interface Engineering Series. **56**: p. 44.
5. Williams, J.A. and R.S. Dwyer-Joyce, *Contact between solid surfaces.* Modern tribology handbook, 2001. **1**: p. 121-162.
6. Hertz, H., *Über die Berührung fester elastischer Körper.* Journal für die reine und angewandte Mathematik, 1882. **92**: p. 156-171.
7. Timsit, R.S., *Electrical Contact Resistance.* in Electrical Contacts Principles and Applications, 1999(P.G. Slade, Marcel Dekker, New York): p. 943-1017.
8. Johnson, K.L. and K.L. Johnson, *Contact mechanics*. 1987: Cambridge university press.
9. Bowden, F. and D. Tabor, *The area of contact between stationary and between moving surfaces.* Proceedings of the Royal Society of London. Series A, Mathematical and Physical Sciences, 1939: p. 391-413.
10. Dyson, J. and W. Hirst, *The true contact area between solids.* Proceedings of the Physical Society. Section B, 1954. **67**(4): p. 309.
11. Holm, R., *Electric contacts: theory and application*. 2013: Springer Science & Business Media.
12. Archard, J. and W. Hirst. *An examination of a mild wear process*. in *Proceedings of the Royal Society of London A: Mathematical, Physical and Engineering Sciences*. 1957. The Royal Society.
13. Archard, J. *Elastic deformation and the laws of friction*. in *Proceedings of the Royal Society of London A: Mathematical, Physical and Engineering Sciences*. 1957. The Royal Society.
14. Greenwood, J. and J. Williamson. *Contact of nominally flat surfaces*. in *Proceedings of the Royal Society of London A: Mathematical, Physical and Engineering Sciences*. 1966. The Royal Society.
15. Krim, J., *Resource Letter: FMMLS-1: Friction at macroscopic and microscopic length scales.* American Journal of Physics, 2002. **70**(9): p. 890-897.
16. Amontons, G., *De la Resistance Causes dans les Machines.* Academie Royale A, 1699: p. 275-282.
17. Adam, N.K., *The Physics and Chemistry of Surfaces.* Oxford University Press, 1938: p. 232.
18. Bowden, F.P. and D. Tabor, *The friction and lubrication of solids*. Vol. 1. 2001: Oxford university press.
19. Scharf, T.W. and S.V. Prasad, *Solid lubricants: a review.* Journal of Materials Science, 2012. **48**(2): p. 511-531.
20. Rabinowicz, E., *Friction and Wear of Materials.* Wiley, New York, NY, 1965: p. 69.

21. Blau, P.J., *Friction science and technology: from concepts to applications*. 2008: CRC press.
22. Rigney, D. and J. Hirth, *Plastic deformation and sliding friction of metals.* Wear, 1979. **53**(2): p. 345-370.
23. Prasad, S.V., C.C. Battaile, and P.G. Kotula, *Friction transitions in nanocrystalline nickel.* Scripta Materialia, 2011. **64**(8): p. 729-732.
24. Mishra, R., B. Basu, and R. Balasubramaniam, *Effect of grain size on the tribological behavior of nanocrystalline nickel.* Materials Science and Engineering: A, 2004. **373**(1): p. 370-373.
25. Zhang, Y., et al., *Friction and wear behaviors of nanocrystalline surface layer of pure copper.* Wear, 2006. **260**(9): p. 942-948.
26. Raj, R. and M. Ashby, *On grain boundary sliding and diffusional creep.* Metallurgical transactions, 1971. **2**(4): p. 1113-1127.
27. Antler, M., *Sliding wear of metallic contacts.* Components, Hybrids, and Manufacturing Technology, IEEE Transactions on, 1981. **4**(1): p. 15-29.
28. Stachowiak, G. and A.W. Batchelor, *Engineering tribology*. 2013: Butterworth-Heinemann.
29. Stachowiak, G.W., *Wear: materials, mechanisms and practice*. 2006: John Wiley & Sons.
30. Moore, D.F., *Principles and Applications of Tribology: Pergamon International Library of Science, Technology, Engineering and Social Studies: International Series in Materials Science and Technology*. Vol. 14. 2013: Elsevier.
31. Suh, N.P., *The delamination theory of wear.* Wear, 1973. **25**(1): p. 111-124.
32. Binder, L., *Der Widerstand von Kontakten.* Elektrotech. Maschinenbau, 1912. **30**: p. 781-782.
33. Greenwood, J., *Constriction resistance and the real area of contact.* British Journal of Applied Physics, 1966. **17**(12): p. 1621.
34. Slade, P.G., *Electrical Contacts: Principles and Applications.* Marcel Dekker, New York, 1999.
35. Mott, N., *The theory of the formation of protective oxide films on metals.—III.* Transactions of the Faraday Society, 1947. **43**: p. 429-434.
36. Fehlner, F.P. and N.F. Mott, *Low-temperature oxidation.* Oxidation of metals, 1970. **2**(1): p. 59-99.
37. Young, F.W., J.V. Cathcart, and A.T. Gwathmey, *The rates of oxidation of several faces of a single crystal of copper as determined with elliptically polarized light.* Acta Metallurgica, 1956. **4**(2): p. 145-152.

CHAPTER 3

EXPERIMENTAL METHODS AND PROCEDURE

3.1 Electron-beam Film Deposition

3.1.1 E-beam Deposition System and Sample Preparation

A Thermionics Vacuum Products Co.10 kV Triad e-beam evaporation system was used for the deposition of both pure Au and composite Au-ZnO films, a picture of the vacuum system, power supply, and control electronics is provided in Fig. 3.1. As a high vacuum deposition process, e-beam synthesized films are typically free from contamination and highly conformal to the substrate. The electron beam path and film material deposition is shown schematically in Fig. 3.2. The electron beam is generated by a field emission source and magnetically deflected to the crucible to provide localized heating resulting in the sublimation of the film material. Once sublimated in a vacuum the film material deposits on the target substrate in line of sight from the crucible. Prior to all film depositions the vacuum chamber was pumped to a base pressure of less than $1x10^{-6}$ Torr. The film material source to substrate

Fig. 3.1: Photograph of the Thermionics Vacuum Products Co. Triad e-beam evaporation system with accompanying power supply and control electronics. Photograph courtesy of Ron Goeke from Sandia National Laboratories.

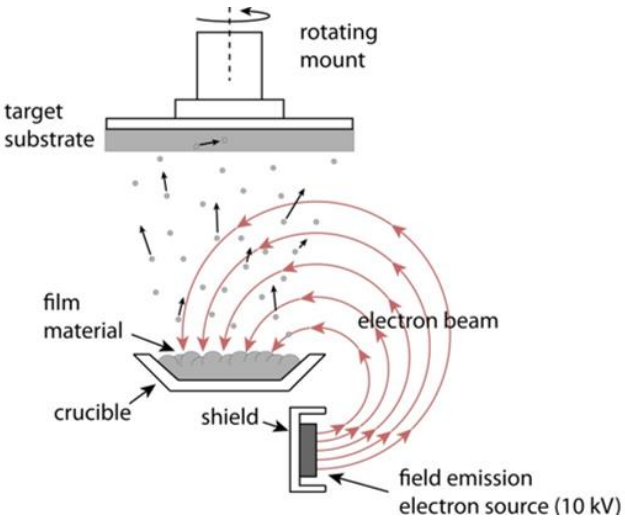

Fig. 3.2: Schematic of e-beam evaporation process highlighting the electron beam path from emission source to crucible and the resultant evaporation and deposition of film material.

distance was 300 mm and all depositions were conducted at room temperature. To achieve compositional and thickness uniformity of the films, a rotating substrate mount was used as shown in Fig. 3.2.

Various substrate materials were used depending on the experimental testing and characterization of the films. For the majority of the films used in sliding ECR tribometer testing, Si substrates were cut into 10 mm^2 squares from wafers by diamond scribing. The Si wafers were cleaned in acetone and isopropyl alcohol baths then subsequently cleaned by oxygen plasma prior to deposition. The native oxide on the Si wafer surface (estimated to be approximately 3 nm thick) provided an interdiffusion barrier between the Si and deposited adhesion or film layers. Prior to e-beam deposition the Si substrates were first sputter coated with a nominally 500 nm thick Ti layer for adhesion followed by a nominally 500 nm thick Pt layer to act as a diffusion barrier. Samples used for in-situ resistivity annealing experiments, described in section 3.5.2, were deposited directly onto polished 25 mm^2 square sintered Al_2O_3 substrates 3.2 mm thick that went through the same substrate cleaning procedures as the Si

substrates.

3.1.2 Pure Au Film Deposition

The pure e-beam Au films to be subsequently implanted by noble gas ions were deposited onto the Si substrates previously sputter coated with Ti adhesion and Pt diffusion layers. The films were deposited by evaporation of high purity Au pellets (99.999% purity) sourced from Materion Advanced Chemicals at room temperature. The rate of deposition was controlled using feedback from a quartz crystal microbalance (QCM) until the Au films were nominally 1.8 µm thick. The deposition rate and thus film thickness was calibrated to the QCM by stylus profilometry. A physical substrate shutter, shown in Fig. 3.3, was used to block the substrates from line of sight of the crucibles to establish the calibrated deposition rates prior to film deposition. The resultant Au film average root-mean-square (RMS) surface roughness was determined by scanning white light interferometry (SWLI) to be less than 3 nm.

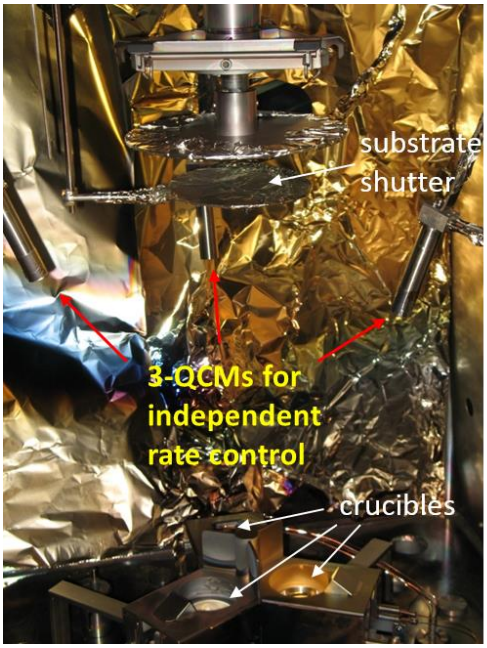

Fig. 3.3: Photograph of the interior of the deposition chamber showing the material crucibles with respective independent QCMs and the substrate shutter. Photograph courtesy of Ron Goeke from Sandia National Laboratories.

3.1.3 Au-ZnO Composite Film Deposition

The composite Au-ZnO films of varying composition were deposited onto Si substrates sputter coated with Ti/Pt layers for sliding ECR tribometer testing and onto polished Al_2O_3 substrates for in-situ resistivity annealing experiments. The source materials were pure Au pellets (99.999% purity) and ZnO tablets (99.9% purity), both from Materion Advanced Chemicals. The Au and ZnO deposition rates were controlled independently by feedback from separate QCMs aligned with the crucibles as shown in Fig. 3.3. Calibration of each QCM was established by stylus profilometry of films deposited from only Au or ZnO. The deposition rates were varied between 0.00 and 2.00 nm-s^{-1} to achieve the desired volume fraction of ZnO in the film. The substrates were blocked by a physical shutter until the desired deposition rates were established and stable to provide uniform composition throughout the film thickness. The resultant film average RMS surface roughness of films deposited on Si substrates was determined by SWLI to be less than 4 nm.

3.2 Ion Beam Implantation

3.2.1 Ion Accelerators and Implantation Methods

Ion implantation of e-beam synthesized Au films was conducted at the ion beam lab of Sandia National Laboratories. For ion implantation at relatively low energies a 350 kV High Voltage Engineering Europa Implanter was used with a beam spot size of approximately 1 µm. Higher energy ion implantations were conducted using a 3 MV National Electrostatics Corp. Pelletron with a beam spot size of approximately 150 nm. All ion implantations were conducted under a base pressure of $1x10^{-7}$ Torr and at nominally room temperature with the

incident ion beam normal to the film surface. Ions of ^{3}He, ^{4}He, Ar, and Au were used to evaluate ion beam modification effects on the tribological and mechanical behavior of the Au films. To produce laterally homogeneous ion distributions in the Au films, the ion beam was rastered in stepped profile across a 10 mm^2 area using deflector plates. Target doses were achieved by integrating measured ion beam current over time until the total fluence was achieved. Post ion implantation film surfaces were cleaned by 25:75 ratio of O_2:Ar plasma for 10 mins to remove any surface carbonaceous species deposited by the ion beam that could affect tribological and ECR measurements.

3.2.2 Prediction of Implanted Ion Ranges and Distributions

The widely used freely available code The Stopping and Range of Ions in Matter (SRIM) 2008, published by James Ziegler, was used for the prediction of ion implantation ranges, distribution, and point defect generation. These set of programs calculate the stopping and range of ions into matter by statistical treatment of averaging collision results between jumps calculated from single quantum mechanical ion-atom collisions. The ion and target atoms are treated as a screened Coulomb interaction during collision, with the target atoms treated as an amorphous homogeneous solid with a single specific binding energy necessary for displacement by either incoming ions or knock-on atoms. A full description of the code is better left to the author of the program in the similarly titled book [2]. The program is especially suited to the prediction of range and distribution of light ions such as He, which is shown to have a mean error of 7.3 % when implanted into Au for a large range of ion energies in Fig. 3.4 when compared to published range data.

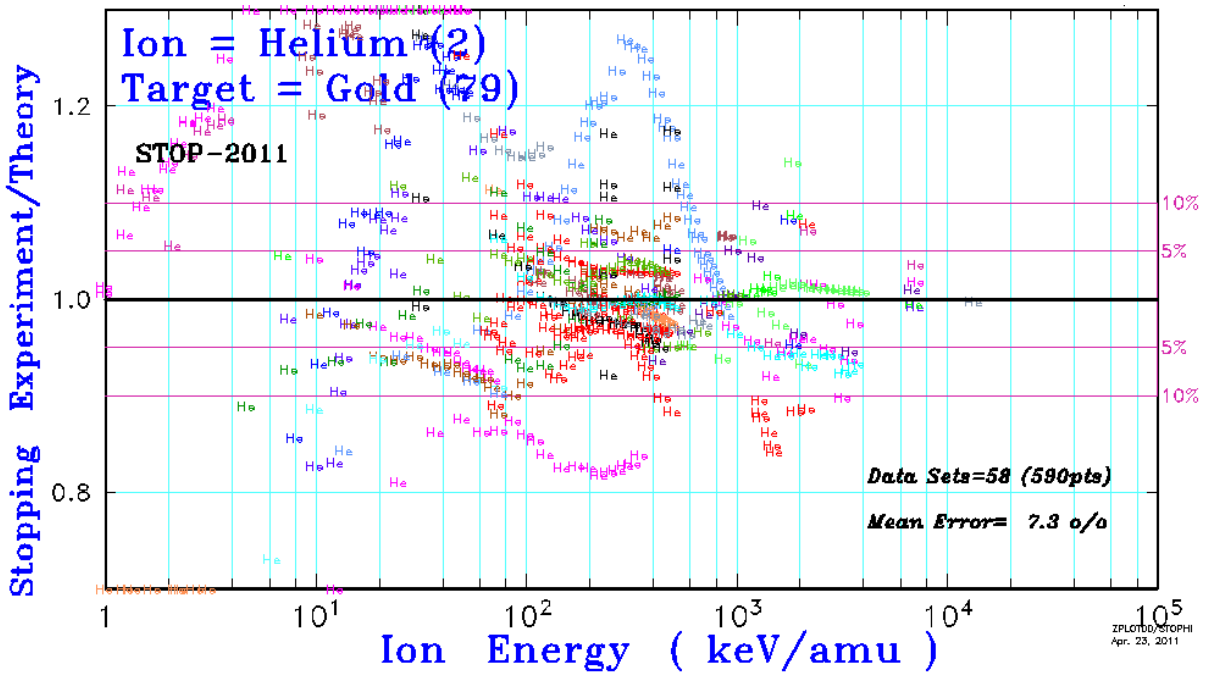

Fig. 3.4: Ratio of published stopping of He ions into Au versus that predicted by SRIM plotted against incident ion energy per atomic mass unit [1].

3.3 Simultaneous Friction and ECR Measurements

3.3.1 Linear ECR Tribometer Capabilities

A custom built linear tribometer equipped with an Agilent Technologies B2911A digital source/meter, photograph and accompanying schematic shown in Fig. 3.5, was used to conduct all simultaneous friction and ECR measurements. The tribometer independently measures applied normal force and lateral or frictional force through independent double leaf flexures, which constrain the displacement to in plane linear motion, coupled to load cells. The load cells were independently calibrated using dead weights and calibrated scales throughout the expected experimental loads, thus incorporating the leaf flexure spring rate into the calibration. Continuous ECR measurements are made by operating the source/meter in voltage-regulated remote sensing mode and measuring the voltage drop and current using a four-point probe

bridged across the film surface and counterface pin. Both the substrate of the film and the counterface pin are electrically isolated from the rest of the rig by custom fixtures machined from polycarbonate and polyether ether ketone, respectively.

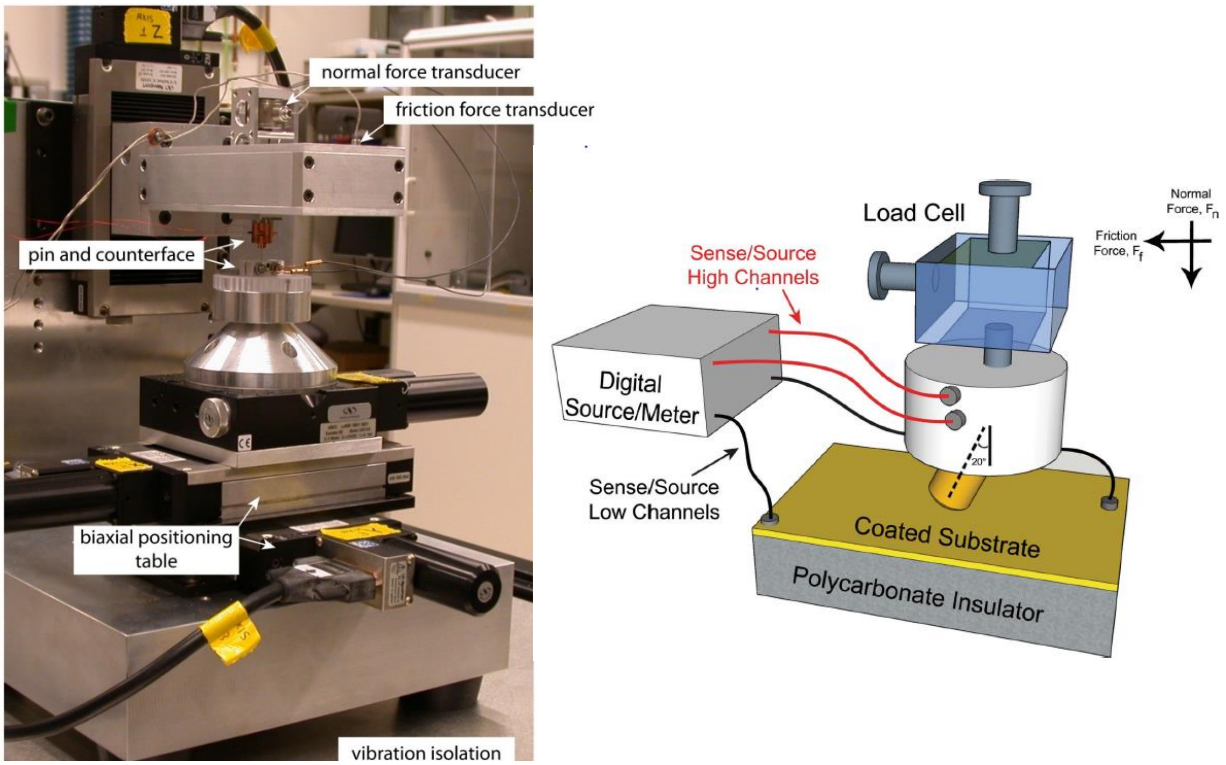

Fig. 3.5: Photograph and accompanying schematic of custom-built linear ECR tribometer. Photograph courtesy of Rand Garfield from Sandia National Laboratories.

3.3.2 Materials and Methods of Sliding ECR Tribometry Experiments

All tribological friction ECR tests were conducted in unidirectional sliding motion by translating the bottom fixture by the 2 mm track length while recording data then lifting the upper load cell assembly and translating the bottom fixture to the start position and repeating. A normal force of 100 mN and a linear speed of 1 mm-s^{-1} were used for a duration of 100 sliding cycles. Prior to each sliding ECR experiment a static normal force of 100 mN was applied and a voltage set to produce approximately 100 mA of direct current through the ECR circuit. All tests were conducted at room temperature in lab air (15-30 % relative humidity). The counterface

rider was made from Neyoro G alloy wires, a hard Au-Cu alloy nominally 72Au-14Cu-8Pt-5Ag by weight, sourced from Deringer-Ney Inc. The Au-Cu alloy wires were first annealed to a hardness of approximately 1.96 GPa and then hand machined on a lathe to produce a hemispherical tip with a 1.59 ± 0.05 mm radius of curvature to produce a point contact geometry. The machined hemispherical tips were subsequently hand lapped using progressively finer diamond paste to a center line average roughness (R_a) of 100 nm or less measured by SWLI. Prior to sliding experiments the polished riders were ultrasonically cleaned in isopropyl alcohol and blown dry with dry nitrogen. The top insulating fixture holds the Au-Cu alloy counterface pin at a canted angle of 20° as shown in Fig. 3.5 so that multiple tests could be conducted on a single rider by rotating it about its cylindrical axis to a unique contact area.

3.4 Film Structural and Mechanical Properties Determination

3.4.1 Scanning White Light Interferometry of Surface Profiles

Surface topography data of the Au-Cu alloys and films pre and post sliding ECR tribometry were collected using a Veeco NT1100 scanning white light interferometer (SWLI) with either a 50X or 10X objective lens. The topographical height data was then analyzed using Bruker Vision64 version 5.41 software. Wear volumes of the pins post sliding ECR testing were measured as the missing volume displaced below a reference plane fitted to the unworn film surface outside the wear track. These wear volumes were used to calculate the specific wear rate, given in Eq. 3.1, known as Archard's equation, where V is the wear volume, F is the applied normal load, and d is the total sliding distance of the rider. These values are reported in their traditional units of mm^3-$(N\text{-}m)^{-1}$.

$$k = \frac{V}{Fd} \tag{3.1}$$

Film transfer volumes and wear volumes of the Au-Cu alloy rider surfaces were taken as the measured volume above or below, respectively, a level reference plane after planarizing a spherical fit of the measured hemispherical tip geometry surrounding the wear area.

3.4.2 Nanoindentation

A Nanoindenter XP (Agilent Technologies Inc., formerly Nanoinstruments Inc., Oak Ridge TN) was used to perform dynamic AC coupled indentations using a diamond Berkovich tip to determine film hardness and modulus values. The Berkovich tip area function was calibrated by indentation into a fused silica reference according to ASTM E2546-15. Dynamic indentation is an established technique of using a lock-in amplifier and waveform to oscillate the loading coil and monitor the displacement thus enabling a measurement of contact stiffness continuously with increasing displacement of the indenter into the sample [3]. A total of sixteen individual indentations in a 4x4 matrix with a minimum spacing of 100 μm between indents were performed per film tested to a maximum indentation depth of 1000 nm each. Further data analysis pertinent to Berkovich tip shape effects and indentation depth is described in the subsequent results and discussion chapters.

3.4.3 X-Ray Diffraction

X-Ray diffraction (XRD) analysis was conducted using a Bruker D8 diffractometer and general area detector diffraction system. The sample mount was equipped with an Eulerian texture cradle capable of sample tilt angles of 0 - 78° and rotation about the sample normal from 0 - 354°. A sealed tube CuKα X-ray source producing a wavelength of 1.54 Å with incident-beam mirror optics to remove Kβ radiation was employed. Diffraction data sets were collected

in θ-2θ mode for 2θ angles of 15-80° at sample tilt angles from 0 - 66° in increments of 6°. Data sets collected at varying sample tilt angles were analyzed using the MATLAB code Tilt-A-Whirl developed at Sandia National Labs [4].

3.4.4 Scanning Electron Microscopy, FIB Milling, and Kikuchi Diffraction

Scanning electron microscopy (SEM) images of wear track surfaces and grain sizes of the pure e-beam deposited Au samples were collected using a Zeiss Supra 55 VP SEM operated at 20 kV. Grain sizes of the pure e-beam Au film were determined by collecting electron backscatter diffraction (EBSD) maps and data analysis using Oxford Channel 5 software.

Transmission electron microscopy (TEM) specimens were prepared using a FEI Helios 450 dual platform focused ion beam (FIB)/SEM using in-situ Pt deposition to protect sample surfaces from ion damage. The FIB milled TEM specimens were then removed from the bulk of the film using an ex-situ microprobe and transferred to C film coated Cu grid TEM specimen holders. The FIB was also used to mill cross-sections to the surface normal of e-beam Au-ZnO composite films using standard ion milling techniques with the revealed cross-section surface polished by low energy (2 kV Ga^{+}) ions to enhance grain boundary contrast for line-intercept measurement of grain sizes.

Due to the small grain size of certain e-beam Au-ZnO films standard EBSD measurements were impractical. For these films crystallographic texture and grain size were determined by utilizing the transmission Kikuchi diffraction (TKD) method [5], which requires the specimen be prepared in a similar fashion to TEM specimens such that a thin damage free section is sufficiently thin for electron transmission. Plan view specimens were prepared in the FIB by first milling a larger section of the film free and mounting it to a grid where it was

subsequently polished by low kV ions to remove surface damage from higher kV milling. The TKD maps were collected in the dual beam FIB/SEM with the SEM operating at 30 kV and the specimen surface normal at 10° tilt with respect to the electron beam. Data was collected using an Oxford Aztec EBSD system with a step size of 10 nm. Grain size was determined from the TKD maps by taking a contiguous line measure of grain diameters over distances maintaining an orientation mismatch of less than 10°.

3.4.5 Transmission Electron Microscopy

Scanning transmission electron microscopy (STEM) and X-ray microanalysis were performed on the same samples used for TKD as well as ex-situ FIB lift-outs of as deposited and worn Au-ZnO films with a FEI Company Titan G2 80-200 transmission electron microscope/STEM operated at 200 kV. This microscope is equipped with a high brightness field-emission electron source, a spherical aberration corrector on the probe forming optics, and four integral silicon-drift X-ray detectors (SuperX™) that allow for full X-ray spectral images to be collected and correlated to the 2D image array. As-deposited and worn e-beam Au film implanted with He ions were also imaged using this microscope in bright field, and dark field imaging modes using a high angle annular diffraction (HAADF) detector. Traditional transmission bright field micrographs to analyze grain structure of the same as-deposited and worn He implanted Au TEM specimens were collected using a Philips CM30 TEM operated at 300 kV. To enhance image contrast of the film surfaces, the He implanted Au samples were first sputter coated with C then in-situ locally protected with Pt deposition.

3.5 Electrical Resistivity

3.5.1 Thin Film Resistivity Measurements

Film electrical resistivity measurements of pure Au and Au-ZnO films, deposited directly onto Si substrates, were conducted by first measuring the film sheet resistance values using an adjustable four-point tungsten microprobe assembly and a Keithley 2400 source/meter. Two sheet resistance values were recorded per film by moving the tungsten microprobes to contact unique positions at the square specimen corners. The two unique sheet resistance values were used to calculate the electrical resistivity of the film in accordance with the van der Pauw method [6], with the film thickness taken from calibrated QCM data from e-beam deposition. A more in depth description of how the electrical resistivity of the He ion implanted Au layer is separated from the combined measured sheet resistance of the Au layer deposited on Pt/Ti adhesion layers is given in section 4.1.3.

3.5.2 In-Situ Thin Film Resistivity Annealing Experiments

Au-ZnO composite films deposited on polished AL_2O_3 substrates were annealed in a contiguous temperature profile starting at room temperature and ramped at a rate of 2°C-min^{-1} to dwells at approximately 100, 200, 300, 400, and 500°C for a period of 8 hours each before being passively cooled back to room temperature from the highest temperature. During the full annealing profile, sheet resistance was continuously measured via four-point probe measurement at the specimen corners.

A custom built four-point probe fixture was designed and manufactured for use at elevated temperatures, photographs of which are given in Fig. 3.6. The fixture was fabricated from an alumina base plate with four stainless steel posts holding horizontal rods machined

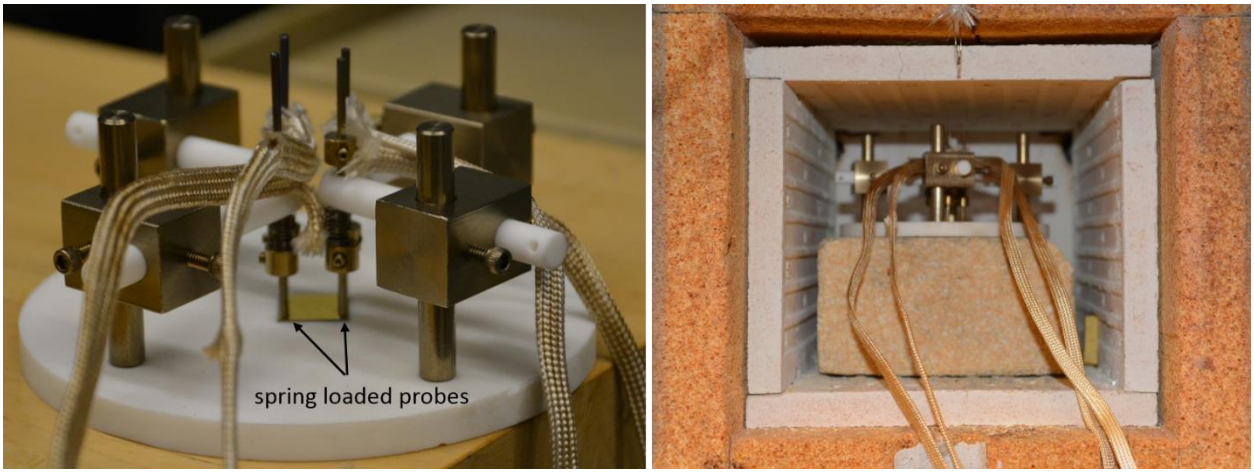

Fig. 3.6: Photographs of the custom built high temperature four-point probe resistivity fixture outside and inside the annealing furnace.

from Macor, adjustable by set screws, to provide electrical isolation to the specimen and contact probes. The contact probes were fitted through holes drilled in the Macor rods and constrained by set screw collars. Contact probes were made from 3 mm W rod with one end machined to a spherical radius of approximately 6 mm by turning then subsequently hand polished with diamond paste before being cleaned in isopropyl alcohol and finally sputter coated with Pt to prevent diffusion into the sample film and oxidation at the contact interface. Steel springs were used to apply a normal force to the Pt coated W probe tips and were the only clamping force holding the sample at the corner positions of the specimen in accordance with the van der Pauw measurement technique [6]. Copper wires were swaged to the W probes and glass fiber insulated for use in the furnace to provide measurement of the sheet resistance via source meter. The annealing experiments were performed in a ceramic lined electrically heated furnace with a hinged door and an internal volume envelope approximately 150 x 150 x 150 mm.

The annealing temperature profile was controlled using a commercial proportional

integral derivative (PID) controller and the furnace equipped thermocouples. Temperature of the film was measured by a K-type thermocouple affixed to the fixture so that it was lightly in contact with the film surface at the center of the square sample. Sheet resistance was measured with an Agilent 34420A micro-ohm meter. Sheet resistance values and temperature data from the K-type thermocouple were continuously recorded throughout the experiment at a rate of 1 kHz using a National Instruments USB-6008 data acquisition card connected to a laptop running LabVIEW 8.1. Data analysis and grain growth determination from these experiments are described in section 5.3.

3.6 Chapter 3 References

1. *http://www.srim.org/SRIM/SRIMPICS/STOP02/STOP0279.gif.*
2. Ziegler, J.F. and J.P. Biersack, *SRIM-2008, Stopping Power and Range of Ions in Matter.* 2008.
3. Oliver, W.C. and G.M. Pharr, *Measurement of hardness and elastic modulus by instrumented indentation: Advances in understanding and refinements to methodology.* Journal of materials research, 2004. **19**(01): p. 3-20.
4. Rodriguez, M.A., et al., *TILT-A-WHIRL: a texture analysis package for 3D rendering of pole figures using M atlab.* Powder Diffraction, 2013. **28**(02): p. 81-89.
5. Trimby, P.W., *Orientation mapping of nanostructured materials using transmission Kikuchi diffraction in the scanning electron microscope.* Ultramicroscopy, 2012. **120**: p. 16-24.
6. van der Pauw, L., *A method of measuring the resistivity and Hall coefficient on lamellae of arbitrary shape.* 1958.

CHAPTER 4[†]

STRUCTURE, ELECTRICAL RESISTIVITY, MECHANICAL BEHAVIOR, TRIBOLOGY, AND ELECTRICAL CONTACT RESISTSANCEOF NOBLE ION IMPLANTED Au FILMS

This chapter presents the results and discussion of noble ion implantation effects on the microstructure, electrical resistivity, mechanical behavior, sliding friction, wear mechanisms, and electrical contact resistance of e-beam deposited Au thin films. The majority of this chapter is focused on the largest sample set of varying ion implantation conditions, implantation energy (E) and fluence (ϕ), listed in Table 4.2, which utilized ^{3}He ions implanted at mean depths varying from the near surface (~48 nm) to the full Au film thickness (~1.8 µm). Au ion implantation that is expected only to alter the e-beam Au films by introducing point defects, and a small set of samples implanted with higher atomic mass noble ions, Ar, were generated to see if similar tribological and sliding ECR results could be obtained to that of specific ^{3}He implanted samples utilizing relatively low fluences.

[†] Portions of this chapter are presented based on the publication by J.E. Mogonye, K. Hattar, P.G. Kotula, T.W. Scharf, and S.V. Prasad, "He implantation for improved tribological performance in Au electrical contacts," Journal of Materials Science 50.1 (2015): 382-392 with permission from Springer Publishing.

4.1 He Ion Implantation Distributions and Effects on Film Microstructure and Resistivity

4.1.1 SRIM Modelling of He Ion Distributions and Stopping

Utilizing SRIM generated ^{3}He ion range (mean implantation depth) in Au, a series of implantation energies were chosen such that the range of the implanted He distributions would vary from the very near surface (~48 nm for the lowest energy) to the full thickness of the e-beam Au film. The five energies chosen to generate these varying He ion distributions are given in Table 4.1 along with the respective aggregate ratio of electronic to nuclear stopping power, Au vacancy generation per incident ion, ion range, and ion straggle generated by SRIM modelling of 100,000 ^{3}He ions (3.003 amu) into Au. Due to the low atomic mass of ^{3}He ions, the predominant stopping mechanism during implantation into Au is due to electronic drag interactions and ionization as represented by the ratio of electronic to nuclear stopping in Table 4.1 that reveals a several order magnitude difference between stopping powers. Also due to the relatively low nuclear interaction of the ^{3}He ions with Au, the resultant Au vacancy generation per incident ion is expected to be of the second or third order of magnitude per ion for each energy condition used here in.

Table 4.1: Summary of SRIM predicted results for ^{3}He ion implantation into Au including ratio of electronic and nuclear stopping powers, Au vacancy generation, ion range (mean of ion distribution) and straggle (one standard deviation of ion distribution).

Ion energy (keV)	Ratio of electronic/nuclear stopping	Au vacancies generated per incident ion	Range (Å)	Straggle (Å)
22.5	17.6	44	482	536
45	31.0	68	950	813
250	183	137	4462	1756
650	455	170	9728	2310
1200	683	193	16900	2764

Ion distribution results from SRIM modeling of 100,000 ^{3}He ions for each energy in Table 4.1 were used to generate the He concentration profiles shown in Fig. 4.1 by scaling the ion distribution by each unique fluence ($1x10^{10}$, $1x10^{12}$, $1x10^{14}$, and $1x10^{16}$ cm^{-2}) used in sample generation. These distributions represent the expected at.% He concentration profile for each of the single energy implant condition samples prepared and listed in Table 4.2. The highest expected local concentration of He is approximately 1.6 at.% for the E = 22.5 keV, $\phi = 1x10^{16}$

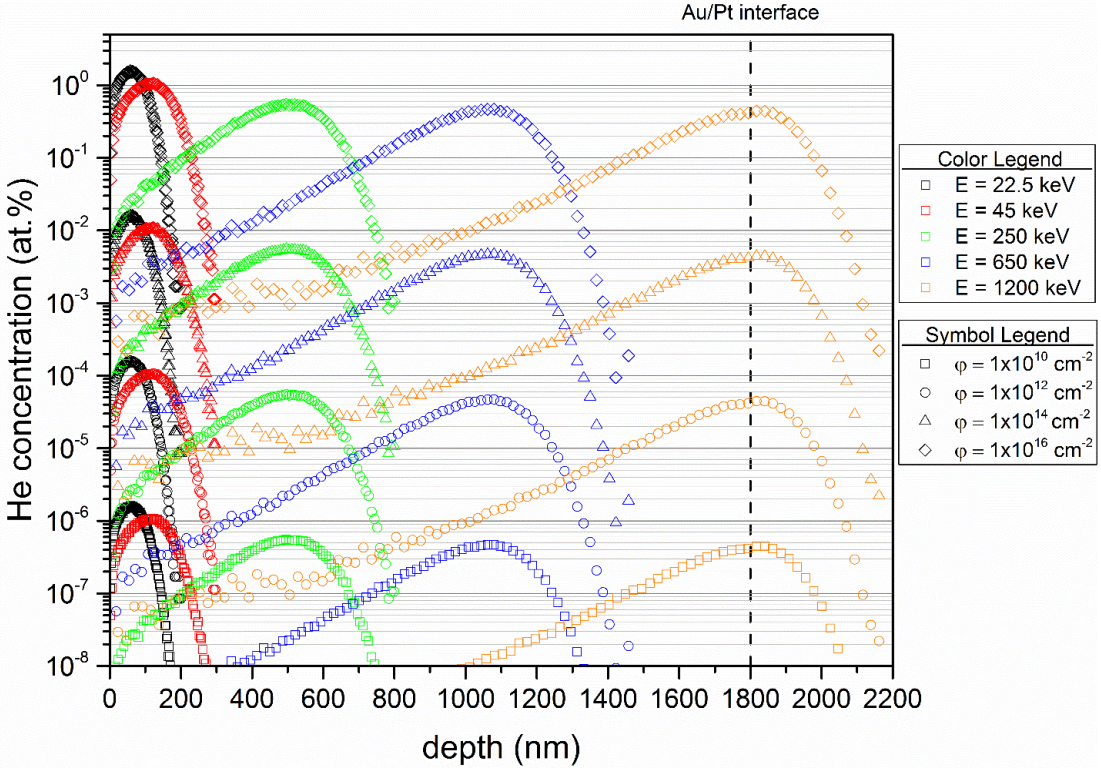

Fig. 4.1: SRIM predicted He concentration in at.% versus implantation depth into Au film for each implantation energy, E, and implantation fluence, ϕ, used for sample generation. Vertical dashed line marks the Au/Pt film interface.

cm^{-2} condition. Samples utilizing multiple energies of He ion implantation to generate broader distributions of He concentration in the Au film were generated by sequential implantation in decreasing energy steps. These multiple energy implantation profiles utilized fluences listed in Table 4.2 such that the cumulative fluence sum of He ions resulted in $1x10^{12}$ or $1x10^{16}$ cm^{-2} for

Table 4.2: ^{3}He ion implantation conditions used for sample generation. In multiple energy implant conditions implantation was sequenced in decreasing energy.

Sample No.	Energy, E (keV)				Fluence, ϕ (cm^{-2})				Fluence sum (cm^{-2})
	E_1	E_2	E_3	E_4	ϕ_1	ϕ_2	ϕ_3	ϕ_4	
1	22.5				1E10				1E10
2	22.5				1E12				1E12
3	22.5				1E14				1E14
4	22.5				1E16				1E16
5	45				1E10				1E10
6	45				1E12				1E12
7	45				1E14				1E14
8	45				1E16				1E16
9	250				1E10				1E10
10	250				1E12				1E12
11	250				1E14				1E14
12	250				1E16				1E16
13	650				1E10				1E10
14	650				1E12				1E12
15	650				1E14				1E14
16	650				1E16				1E16
17	1200				1E10				1E10
18	1200				1E12				1E12
19	1200				1E14				1E14
20	1200				1E16				1E16
21	22.5	45			5E11	5E11			1E12
22	22.5	45			5E15	5E15			1E16
23	22.5	250			5E11	5E11			1E12
24	22.5	250			5E15	5E15			1E16
25	22.5	650			5E11	5E11			1E12
26	22.5	650			5E15	5E15			1E16
27	22.5	1200			5E11	5E11			1E12
28	22.5	1200			5E15	5E15			1E16
29	45	250			5E11	5E11			1E12
30	45	250			5E15	5E15			1E16
31	45	650			5E11	5E11			1E12
32	45	650			5E15	5E15			1E16
33	45	1200			5E11	5E11			1E12
34	45	1200			5E15	5E15			1E16
35	250	650			5E11	5E11			1E12
36	250	650			5E15	5E15			1E16
37	250	1200			5E11	5E11			1E12
38	250	1200			5E15	5E15			1E16
39	650	1200			5E11	5E11			1E12
40	650	1200			5E15	5E15			1E16
41	22.5	45	250	650	5E11	5E11	5E11	5E11	1E12
42	22.5	45	250	650	2.5E13	2.5E13	2.5E13	2.5E13	1E14
43	22.5	45	250	650	2.5E15	2.5E15	2.5E15	2.5E15	1E16

implantation profiles using two energies, or $1x10^{12}$, $1x10^{14}$, or $1x10^{16}$ cm^{-2} for implantation profiles using four energies. The resulting He concentration profiles in the multiple energy implanted samples is expected to be the sum of similarly individually scaled He distributions shown in Fig. 4.1 at a given depth.

4.1.2 He Ion Implantation Effects on Microstructure

XRD patterns collected in θ-2θ scans at each incremented sample tilt angle, ψ, relative to the sample surface normal in increments of 6° from 0-66° of as-deposited e-beam Au and e-beam Au implanted with ^{3}He ions at an energy, E = 650 keV, to a fluence, ϕ = $1x10^{16}$ cm^{-2} are shown in Fig. 4.2a&b, respectively. Both XRD patterns exhibited a high intensity for the (111) family of planes with little to no other signal above background for other crystalline planes expected for structure factor allowed Bragg diffraction of a randomly oriented FCC structure when ψ = 0°. This indicates that the e-beam synthesized Au film on a Pt adhesion layer at room temperature results in a highly textured (111) surface normal structure, and that at He

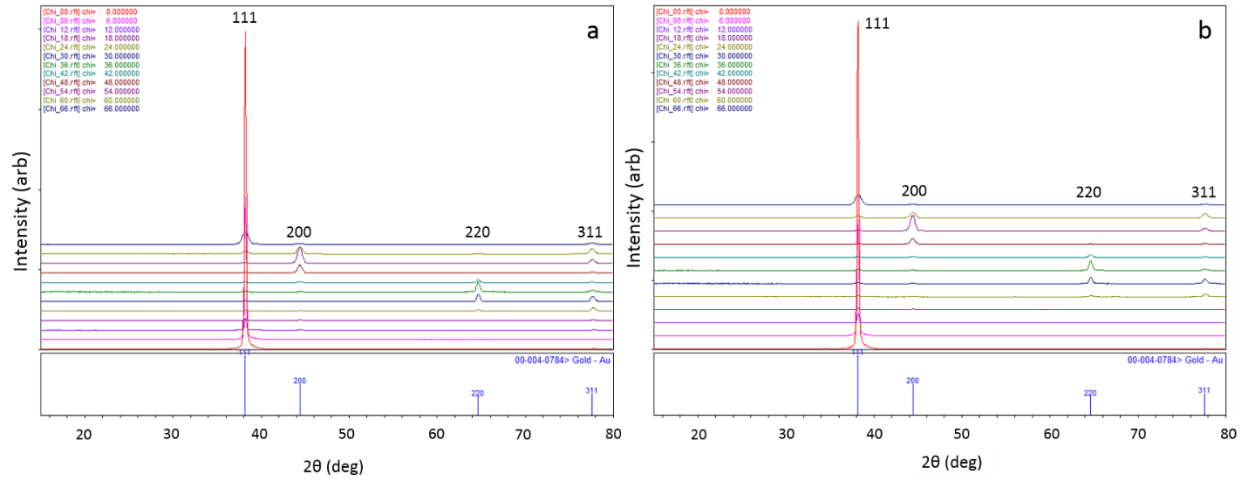

Fig. 4.2: XRD patterns collected at sample tilt angle increments, ψ, of 6°from 0-66° of (a) as-deposited e-beam Au and (b) e-beam Au implanted with ^{3}He ions at an energy, E = 650 keV to a fluence, ϕ = $1x10^{16}$ cm^{-2}, revealing a highly textured FCC (111) surface normal structure for both films.

implantation energies of 650 keV to the highest fluence in the sample matrix of $1x10^{16}$ cm^{-2} did not induce significant heating to incur annealing recrystallization or other effects to alter the texture of the Au grains. Further analysis of this data set and the application of XRD scans at varying tilt angles, ψ, are discussed in section 4.2.3 for film strain analysis.

Bright field TEM micrographs of FIB prepared film cross-sections are shown in Fig. 4.3 of (a) as-deposited e-beam Au and Au implanted with He ions at energies of E = 22.5 keV to a fluence of $\phi = 1x10^{12}$ cm^{-2} and E = 1200 keV to a fluence of $\phi = 1x10^{16}$ cm^{-2} in (b) and (c), respectively. The as-deposited e-beam Au film micrograph exhibited a segmented columnar grain structure with average grain diameters captured in the cross-section on the order of 200-300 nm. This is not representative of the mean grain diameter as pure e-beam Au deposited near room temperature is shown in Fig. 5.1a to have a bimodal grain size distribution with grain diameters on the order of 1 μm occupying roughly half of the film surface normal area.

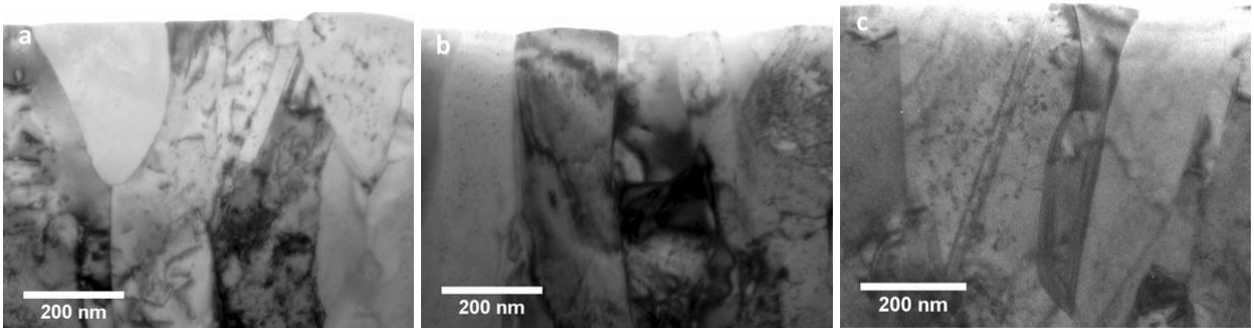

Fig. 4.3: Bright field TEM cross-sectional micrographs of (a) as-deposited e-beam Au, (b) Au He ion implanted at E = 22.5 keV, $\phi = 1x10^{12}$ cm^{-2}, and (c) Au He ion implanted at E = 1200 keV, $\phi = 1x10^{16}$ cm^{-2}.

Selected area diffraction (not shown) of the film cross-section presented in Fig. 4.3a confirmed the (111) film surface normal texture exhibited in the XRD pattern in Fig. 4.2a. Both the He ion implanted films shown in the micrographs of Fig. 4.3a&b retained the columnar grain structure as well as the (111) film texture as that of the as-deposited film. This is further evidence to

indicate that even the highest He ion implantation energy (1200 keV) and the greatest fluence ($1x10^{16}$ cm^{-2}) investigated did not induce significant enough Au film heating so as to initiate annealing, grain growth, and recrystallization. In the TEM specimens presented in Fig. 4.3, circular Fresnel fringes in the bright field image plane were not observed when the objective lens was in under focus (a typical method of observing He implanted bubble structures) indicating that He bubbles were not present in these cross-sections, that the specimens were too thick, or that He structures were unobservable with this instrument.

To investigate potential He implantation induced structures in select ion implanted films, another set of specimen cross-sections were prepared by FIB milling with final Ga^+ ion polishing with the ion beam operating at 2 keV to generate thin and uniform cross-sections. These samples were then imaged using HAADF STEM with an electron beam generated from a Schottky field-emission source operating at 200 kV and with aberration correctors on the probe-forming optics, since this imaging method has been reported to resolve He implantation induced cavities of ~0.8 nm diameter that were not observable by under focus Fresnel fringe contrast [1]. These HAADF STEM cross-sectional images are shown in Fig. 4.4 for implantation conditions of E = 22.5 keV, $\phi = 1x10^{12}$ cm^{-2} in (a-b), E = 650 keV, $\phi = 1x10^{14}$ cm^{-2} in (c), and E = 1200 keV, $\phi = 1x10^{16}$ cm^{-2} in (d). In this imaging mode, lower atomic number regions of the Au film appear as darker contrast. In Fig. 4.4a of the E = 22.5 keV implanted films, there is evidence of near surface spherical formations of darker contrast and at higher magnification in Fig. 4.4b it is revealed that there is a bimodal distribution of spherical formations that may be He containing bubbles or cavity formation. The bimodal distribution contains cavities of

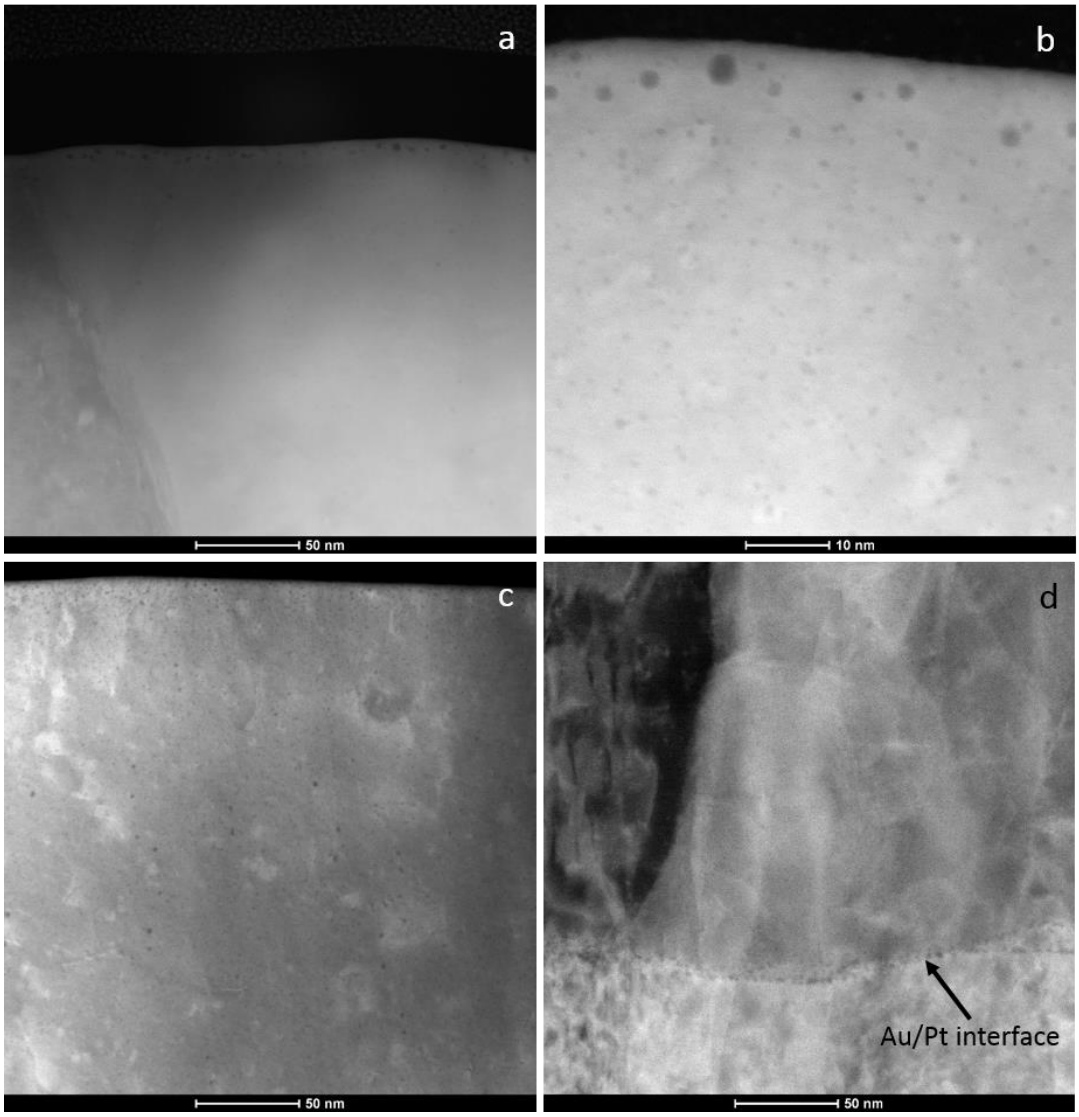

Fig. 4.4: HAADF STEM cross-sectional images of (a-b) Au He ion implanted at E = 22.5 keV, ϕ = $1x10^{12}$ cm^{-2}, (c) Au He ion implanted at E = 650 keV, ϕ = $1x10^{14}$ cm^{-2}, and (d) Au He ion implanted at E = 1200 keV, ϕ = $1x10^{16}$ cm^{-2} (image captured at the Au/Pt interface).

approximately 2-5 nm in the top 10 nm with approximately 1 nm diameter features extending to a depth of nearly 100 nm. The maximum depth of observable cavity formation for 22.5 keV He ion implantation energy is in reasonable agreement with the SRIM predicted range plus one standard deviation (straggle) given in Table 4.1. In Fig. 4.4c for the E = 650 keV implanted film, dark contrast points of He cavity formation appear to be densest in the top 10 nm with observable cavities approximately 1 nm in diameter extending to a depth of 350 nm. The cavity

formation for this film was not observed to extend to the full SRIM predicted range plus its straggle reported in Table 4.1. For the E = 1200 keV implanted film shown in Fig. 4.4d, cavity formation was not observed throughout the full SRIM predicted range however there is a an observable high density of cavities on the order of 1-4 nm located at the Au/Pt adhesion layer interface as well as the larger diameter cavities in the top 10 nm of the film (not shown). This localization of He bubbles/cavities at metallic interfaces has also been observed and documented for Cu/Nb nanolaminate interfaces [2, 3] and is expected to localize in high He concentrations due to reduced defect formation at interfaces and a reduction in interfacial energy at semi-coherent metallic interfaces [4].

4.1.3 He Implantation Effects on Au Film Resistivity

Electrical resistivity values of the He implanted films were characterized by four-point probe measurements of the combined sheet resistance of the Au film and Pt and Ti adhesion layers on the non-conductive Si substrates. Two unique sheet resistance values for each film were recorded by a rotation of the probe positions at the corners of the 10 mm square specimens of 90° in accordance with the van der Pauw method [5]. To isolate the resistivity value of the Au films, the measured combined sheet resistance is treated as a measure of the Au, Pt, Ti layers as resistors in parallel. The resistivity of the Au layer could then be approximated by using Eq. 4.1, where ρ is the material specific resistivity, t is the layer thickness, and R_s is the measured combined sheet resistance. Layer thickness of the adhesion layers were measured from HAADF STEM cross-section micrographs and were measured to have average thickness of $t_{Pt} = 628$ nm, and $t_{Ti} = 462$ nm. The layer thickness of the gold used

in the calculation was taken from QCM measurements during e-beam deposition with an average value of $t_{Au} = 1814$ nm. Resistivity values of the adhesion layers used for the calculation were $\rho_{Pt} = 10.6$ μΩ-cm and $\rho_{Ti} = 55.4$ μΩ-cm.

$$\rho_{Au} = t_{Au}\left(\frac{1}{R_s} - \frac{t_{Pt}}{\rho_{Pt}} - \frac{t_{Ti}}{\rho_{Ti}}\right)^{-1} \tag{4.1}$$

The resultant He ion implanted Au film resistivity values of single energy implantation conditions calculated using Eq. 4.1 are shown in Fig.4.5. The average value of as-deposited e-beam Au measured is plotted as a solid line and its standard deviation as dashed lines. Nearly all of the single energy implantation conditions yielded Au film resistivity values within one standard deviation of the as-deposited e-beam Au condition. This is further evidence that the Au film did not experience significant enough heating from ion implantation for any of the energies or fluences investigated to induce recrystallization or grain growth, as a larger average

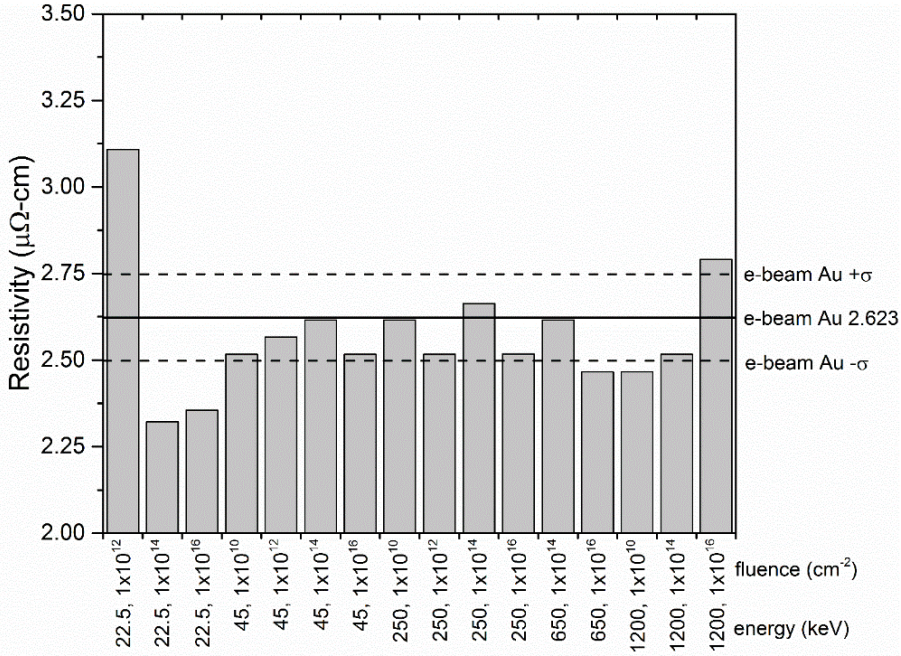

Fig. 4.5: ^{3}He ion implanted Au film resistivity values of single energy implantation conditions calculated from four-point probe measurements using Eq. 4.1.

grain size would decrease the grain boundary density and decrease the measured resistivity. It also suggests that the expected vacancy generation from SRIM modeling listed in Table 4.1 did not introduce enough defects to significantly increase the resistivity.

Further evidence of the negligible effect of ^{3}He ion implantation on Au film resistivity is shown in Fig. 4.6 for multiple implantation energy conditions. Again the majority of the films agree well with the as-deposited e-beam Au resistivity values even when multiple energy implant conditions are expected to generate a more evenly distributed concentration of implantation induced point defects, e.g. vacancies and Au interstitials.

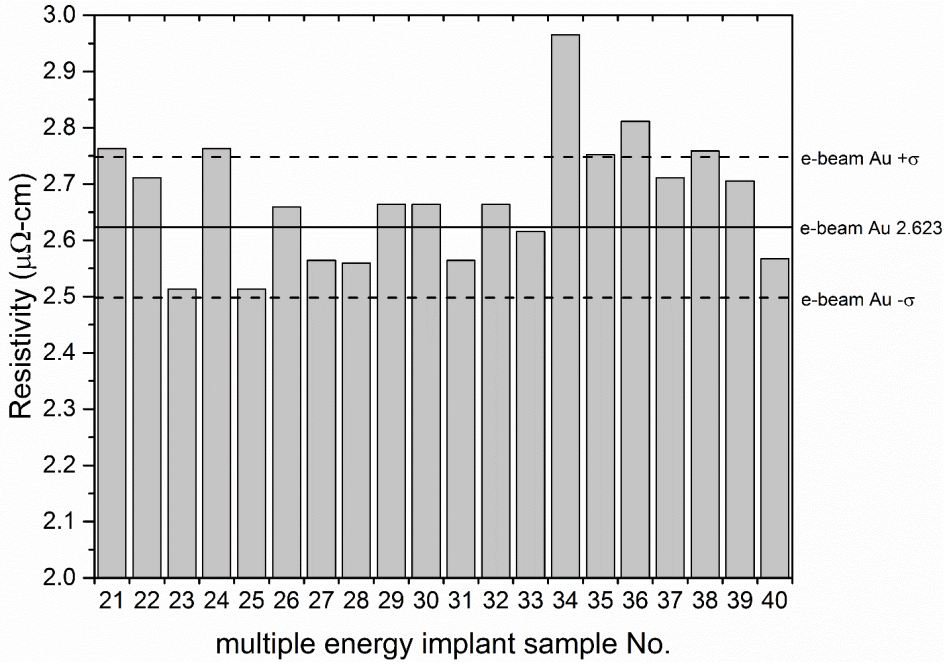

Fig. 4.6: ^{3}He ion implanted Au film resistivity values of multiple energy implantation conditions calculated from four-point probe measurements using Eq. 4.1.

4.2 He Implantation Effects on Mechanical Behavior

4.2.1 Plane Strain-Stress XRD Analysis

Film strain analysis of the XRD peak shifts due to lattice parameter changes collected in

θ-2θ scans at incremented sample tilt angle, ψ, of as-deposited e-beam Au and Au implanted at E = 650 keV to a fluence of ϕ = $1x10^{16}$ cm^{-2} are shown in Fig. 4.7. The film implanted at conditions of E = 650 keV, and ϕ = $1x10^{16}$ cm^{-2} was chosen as its expected ion range was near the center of the Au film, Fig. 4.1, and was implanted to the highest fluence thus would be the most likely of the single implant conditions to produce film strain measurable by this technique.

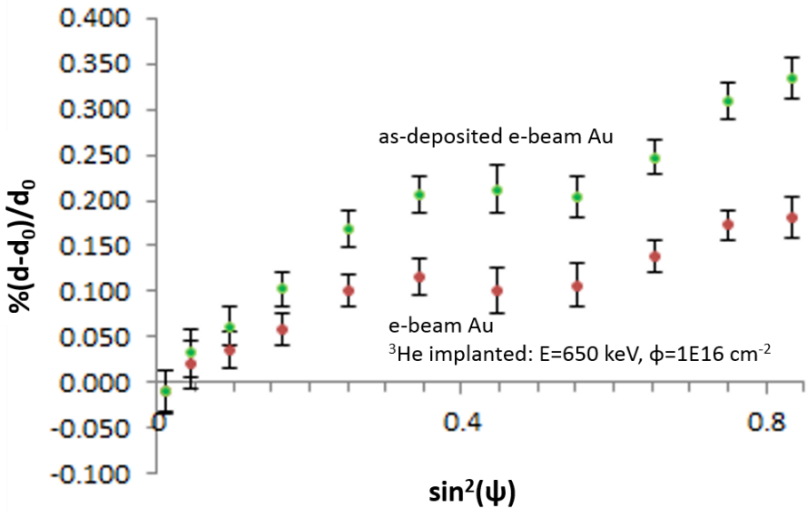

Fig. 4.7: In plane strain versus $sin^2(\psi)$ of as-deposited e-beam Au and Au implanted at E = 650 keV to a fluence of ϕ = $1x10^{16}$ cm^{-2}. Data has been corrected empirically to assumed strain free Ag powder.

The positive slopes of the data in Fig. 4.7 indicate that both films are under in-plane tensile strain, most likely from thermal expansion mismatch strains from e-beam deposition. After empirical correction to Ag powder, linear fits of the data in Fig. 4.7 revealed that the in-plane strain was 0.42% and 0.23% for as-deposited and the He ion implanted films, respectively. The equivalent residual tensile stress from these strain measurements were approximately 74 MPa, and 31 MPa for the as-deposited and He ion implanted specimens, respectively. Based on previously discussed evidence that He ion implantation did not induce recrystallization, grain growth, or other structural changes, it is presumed that the reduction in tensile strain is a result of He ion structures contributing a net compressive strain field in the film. Similar analysis of

integrated stress of Au foils in-situ during He ion implantation by Robic et al. found that compressive stress increased proportionally to ion fluence up to approximately $1x10^{16}$ cm^{-2} [6].

4.2.2 Nanoindentation Hardness

Fig. 4.8 shows nanoindentation hardness, indenter load over stiffness squared (P/S^2), and film elastic modulus (E) values of as-deposited e-beam Au with single energy implant conditions of E = 22.5, 650, and 1200 keV to a fluence of $\phi = 1x10^{10}$ cm^{-2} (a - c, left column) and the same energies implanted to a fluence of $\phi = 1x10^{16}$ cm^{-2} (d - e, right column). Data has been plotted as the mean of 16 indentations with data from indentation depths < 30 nm excluded due to expected indenter tip radius affecting the results. P/S^2 values are included as it is a ratio of directly measured instrument variables that is comparable to hardness that can indicate if surface roughness or plastic pile-up effects are skewing the measured hardness [7], or if adhesive sublayers or the substrate are significantly affecting the results[8]. For the films implanted to a fluence of $\phi = 1x10^{10}$ cm^{-2} in Fig. 4.8a the measured hardness values are all within the measured standard error of the as deposited Au film and exhibited an initial decrease in hardness followed by increasing hardness with increasing indentation depth. The trend of hardness with indentation depth in Fig. 4.8a can be compared to the P/S^2 values in Fig. 4.8b that also exhibit variation for indentation depths < 100 nm before approaching a steady value for indentation depths > 100 nm. The trend in hardness and P/S^2 values with increasing indentation depth are similar for the same energy films implanted to a fluence of $1x10^{16}$ cm^{-2}

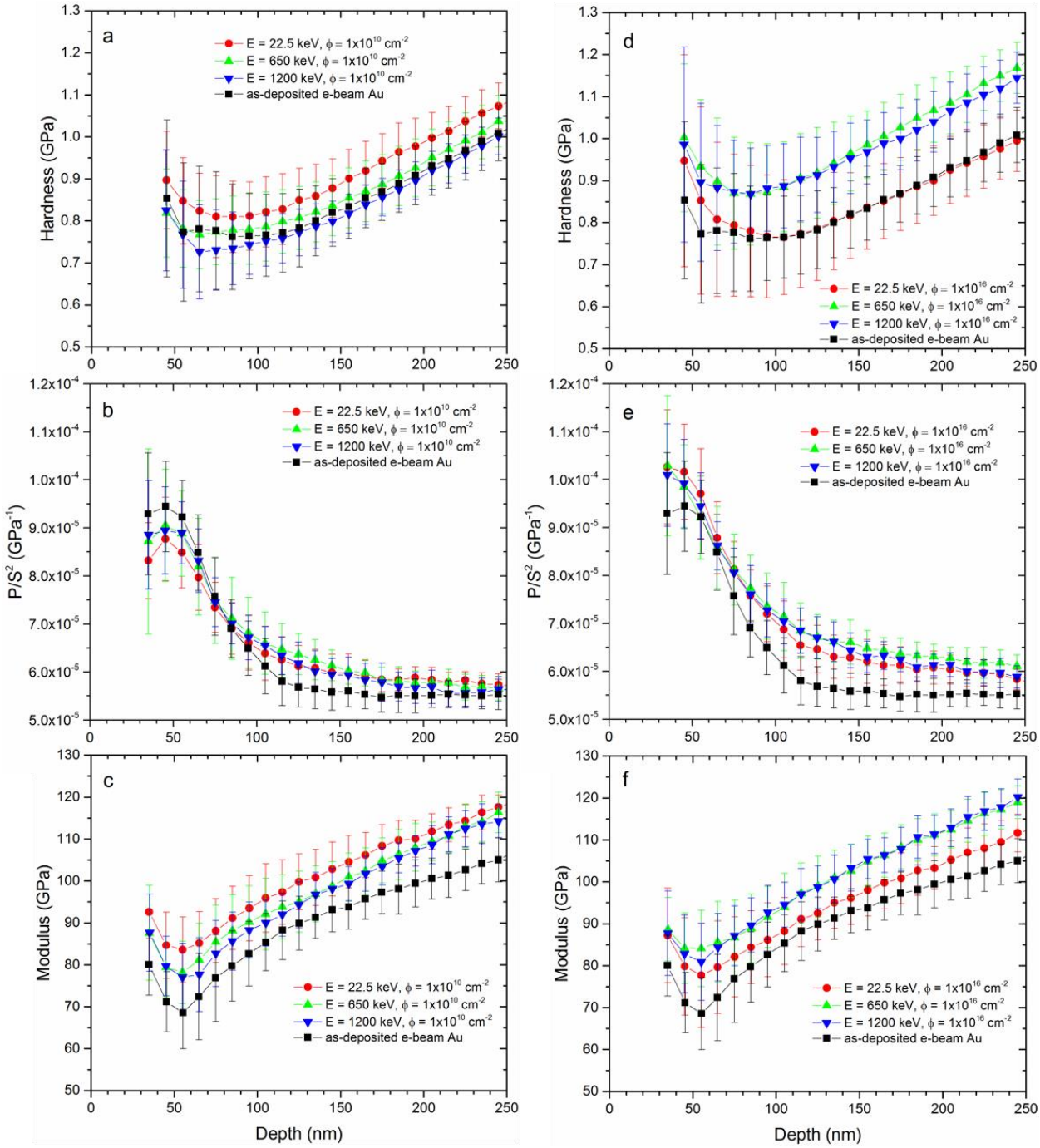

Fig. 4.8: Nanoindentation hardness (a), indenter load normalized by the square of contact stiffness, P/S^2 (b), and film elastic modulus (c), for as-deposited e-beam Au and single energy implant conditions of E = 22.5, 650, and 1200 keV each to a fluence of $\phi = 1x10^{10}$ cm^{-2}. Nanoindentation hardness (d), P/S^2 (e), and film elastic modulus (f) for as-deposited e-beam Au and single energy implant conditions of E = 22.5, 650, and 1200 keV each to a fluence of $\phi = 1x10^{16}$ cm^{-2}. Error bars are standard deviations for data binned at intervals of 10 nm indentation depth.

shown in Figs. 4.7d&e, respectively, however the measured hardness values of the E = 650 and 1200 keV films at this fluence appear to be greater than that of the as-deposited Au film. Film elastic modulus values of films implanted to fluences of $1x10^{10}$ cm^{-2} and $1x10^{16}$ cm^{-2}, Figs. 4.8c and 4.8f, respectively, exhibited increasing values with increasing indentation depth similar to the hardness values. In comparison to the as-deposited e-beam Au, the He implanted films did exhibit small increases in elastic moduli, however due to the modulus data not plateauing with depth for any data set it is unclear if this is an accurate measurement as the increasing trend with depth could be a consequence of adhesion layers or substrate contributions.

Inconclusive results of nanoindentation analysis in Fig. 4.8 are likely due to the relatively low at.% He concentration and non-uniform distribution of the single energy implanted films, demonstrated in Fig. 4.1. To obtain more conclusive data, a new set of samples were generated to have a uniform at.% He concentration that in turn yield a continuous distribution of mechanical behavior with film thickness measurable by nanoindentation. To achieve a more homogeneous distribution of implanted He, a series of SRIM simulations were conducted at varying implantation energies of ^{4}He ions with distributions varying from localized at the very near surface to near the full Au film thickness. The results of these simulations and the resultant individual implantation energies and fluences required to achieve a near homogeneous distribution of 1 at.% He through the majority of the Au film layer are shown in Fig. 4.9. Two other samples were generated to have a near homogeneous distribution of 5 and 1 at.% He, however due to the time required to generate these full profile samples they were implanted with a maximum energy of 500 keV with energies < 500 keV remaining the same as those plotted in Fig. 4.9. To achieve the 5 at.% He concentration specimen, the fluences were

scaled in a similar fashion as those in Fig. 4.9 until the sum of the individual implant conditions approached the target concentration.

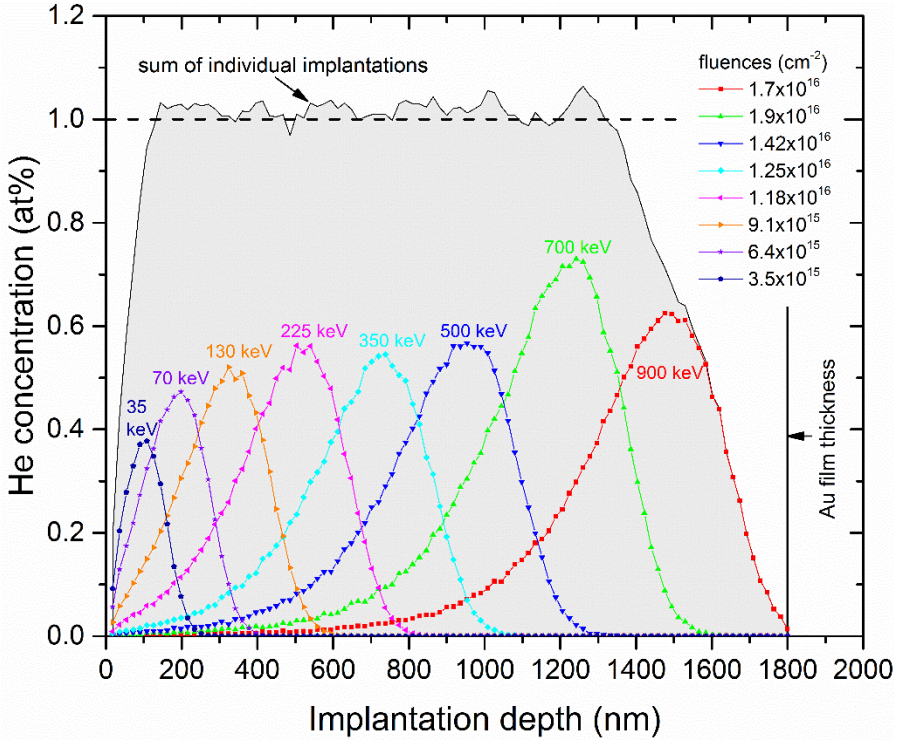

Fig. 4.9: SRIM simulation results of individual ^{4}He ion implantation energies into Au to yield a summed uniform concentration of 1 at.% He.

Nanoindentation hardness, P/S^2, and film elastic modulus values of as-deposited e-beam Au and films uniformly implanted for energies ≤ 500 keV to a concentration of 1 and 5 at.% He, as well as the 1 at.% He concentration profile implanted at a maximum energy of 900 keV, are shown in Fig. 4.10. From Fig. 4.10a it is clear that film hardness increases with increasing He concentration. Comparing the hardness values to the P/S^2 values in Fig. 4.10b there is a commensurate trend with increasing He concentration as well as steady P/S^2 values for indentation depths greater than 100 nm. Similarly the elastic modulus values in Fig. 4.10c appear to approach an asymptotic value for indentation depths greater than 100 nm with values for all the films within error of the as-deposited e-beam Au suggesting contrary to Figs.

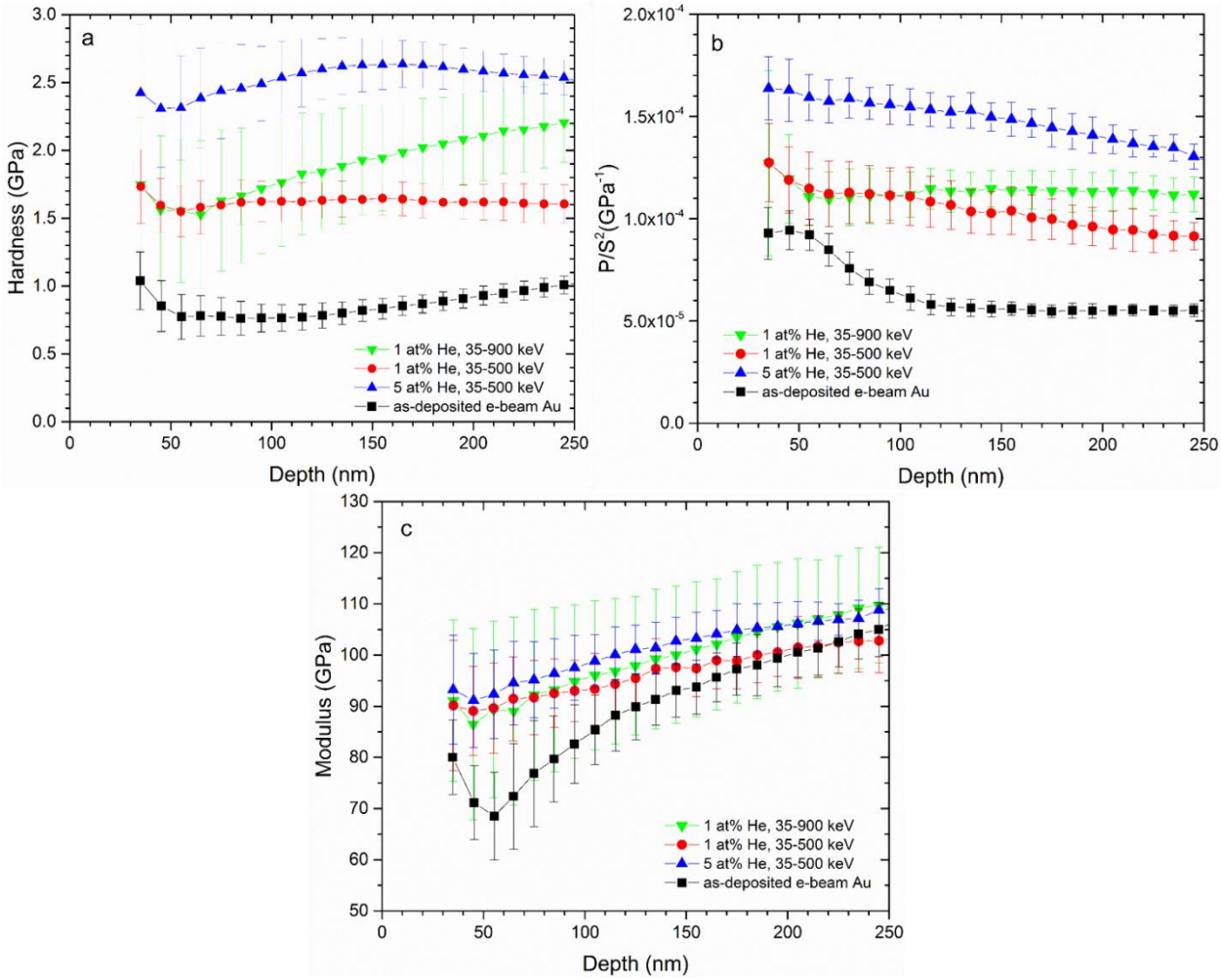

Fig. 4.10: Nanoindentation hardness (a), indenter load normalized by the square of contact stiffness, P/S^2 (b), and film elastic modulus (c) for as-deposited e-beam Au and Au films uniformly implanted to SRIM modeled He concentrations of 1 and 5 at.%. Error bars are standard deviations for data binned at intervals of 10 nm indentation depth.

4.8 c&f that He ion induced structures do not significantly affect the elastic stiffness of the Au film. The average elastic modulus of each film, including the as-deposited Au, are greater than typical polycrystalline values, ~ 79 GPa, which is likely a result of the high degree of (111) texture as shown later in Fig. 5.1a. Average film hardness values were taken from depths > 100 nm coincident with the lower variation in P/S^2 values to exclude possible pile up and indenter geometry effects and have been plotted versus (He concentration)$^{1/3}$ in Fig. 4.11 with the

second ordinate of 1/3 hardness included as Tabor's approximation to yield strength from pyramidal indentation [9]. A linear increase of hardness with (He concentration)$^{1/3}$ is in reasonable agreement with the data in Fig. 4.11. A similar correlation of yield strength being proportional to (He concentration)$^{1/3}$ has been observed by Knapp et al. for Ni uniformly implanted with He ions at room temperature [10]. This relationship is explained by the authors to be a result of an Orowan strengthening mechanism whereby an increase in the volume density of He bubbles and resultant decrease in mean obstacle (He bubbles/cavities) separation yields the 1/3 power dependence on He concentration if the average bubble size remains invariant and similar mechanisms have been described for He implanted Cu [11]. Although an exhaustive TEM analysis of He bubbles/cavities was not conducted in the present study, the mean bubble size excluding the top 10 nm of the film has been observed to be fairly homogeneous and on the order of single of nm's, representative in Fig. 4.4 b&c. The Orowan strengthening mechanism of He bubbles or induced voids is explained by Knapp et al. to be a

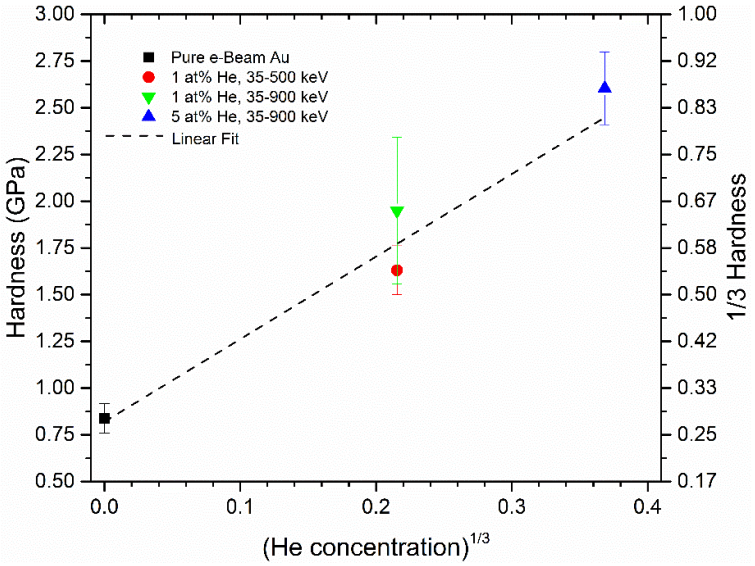

Fig. 4.11: Measured nanoindentation hardness values of uniformly He implanted samples as a function of (He concentration)$^{1/3}$ with the second ordinate of 1/3 hardness as an approximation of yield strength.

result of pinning glissile dislocations by: (1) reduction of dislocation core energy annihilated by intersecting the cavity, (2) reduction in near field strain energy, and (3) an energy barrier from step formation should a dislocation bisect a cavity [10]. As previous XRD analysis, Fig. 4.2, TEM micrographs, Fig. 4.3, and resistivity measurements, Figs. 4.5& 4.6, all suggest that room temperature He ion implantation had negligible effects on the microstructure of the e-beam Au films, and the measured change in hardness is expected to be primarily a result of the Orowan strengthening mechanism as explained by Knapp et al [10].

4.3 Tribology and Sliding ECR of He Ion Implanted e-beam Au

4.3.1 Sliding Friction and ECR Response

The coefficient of friction and corresponding ECR values during sliding ECR measurements of the as-deposited e-beam Au and select single energy He ion implant conditions of E = 22.5 keV, $\phi = 1x10^{12}$ cm^{-2}, and E = 1200 keV, $\phi = 1x10^{16}$ cm^{-2} are shown in Fig.

4.12a&b, respectively. The as-deposited Au film exhibited a rapid run in period of increasing friction over the first 20 cycles before reaching a steady-state value of approximately 1.5-1.75 with high variance, similar to reports of wrought Au [12]. In contrast, the E = 1200 keV film exhibited short run in before reaching a steady state of ~0.5 CoF, while the E = 22.5 keV film exhibited no run in with a stable CoF of 0.45 throughout the 100 cycles of sliding wear. Sliding ECR values per sliding cycle, Fig. 4.12b, of the as-deposited Au exhibited a decrease in ECR during the CoF run in period of the first 20 cycles that is likely a result of increasing contact area due to adhesive asperity deformation during initial wear before approaching a value of 17 mΩ. The E = 22.5 keV film also exhibited a similar trend of decreasing ECR with initial wear during the first few cycles of run in before obtaining similar mean ECR values to that of the as-deposited Au. However, the variance in ECR for cycles beyond run in were least for the E = 1200 keV film. The ECR values off the plotted scale are due to data loss from those cycles likely due to electrical contact separation. Although not all of the collected sliding friction and ECR

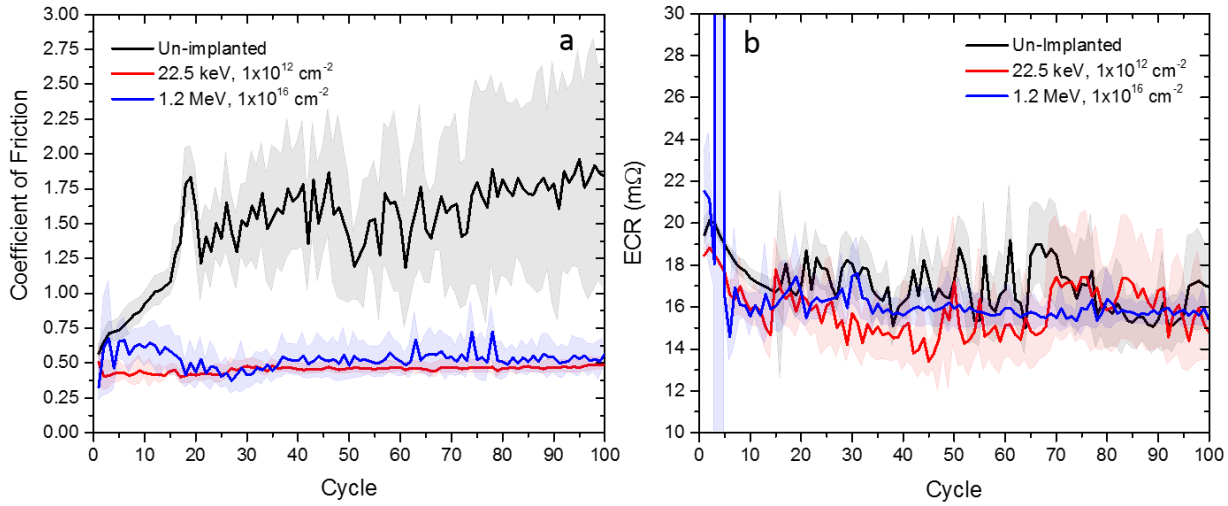

Fig. 4.12: Coefficient of friction (a) and ECR data (b) per sliding cycle for as-deposited e-beam Au and Au implanted with He ions at E = 22.5 keV, ϕ = 1x10^{12} cm^{-2} and E = 1200 keV, ϕ = 1x10^{16} cm^{-2} sliding against a spherically tipped Au-Cu alloy rider. Shaded areas correspond to the average value, solid line, ± 1σ of data collected at 50 Hz.

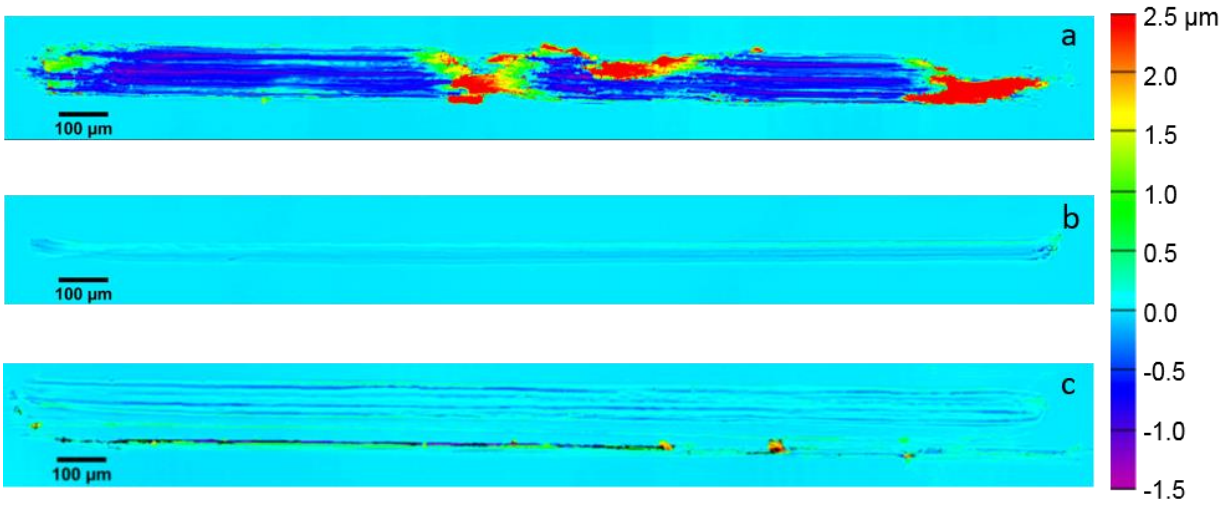

Fig. 4.13: SWLI spectral topographical map of film surfaces after 100 sliding ECR cycles for (a) as-deposited e-beam Au, (b)Au implanted with He ions at E = 22.5 keV, ϕ = $1x10^{12}$ cm^{-2}, and (c) E = 1200 keV, ϕ = $1x10^{16}$ cm^{-2}. *Black regions* in (c) correspond to data loss.

data per cycle of each He ion implantation condition is reproduced herein, the coefficient of friction values varied drastically and are discussed relative to the wear mechanisms in section 4.3.3. Sliding ECR values however were largely unaffected by any of the He ion implantation conditions investigated, with only minor run in fluctuations likely due to third body debris generated contact separation, and maintained steady state ECR values in the range of 16-24 mΩ. This result is in agreement with Figs. 4.5 and 4.6 where it was shown that Au film resistivity is largely unaffected by He ion implantation.

4.3.2 Wear Behavior and Mechanisms

Spectral topographical maps generated from SWLI data collected from the wear tracks generated by sliding ECR measurements on the films in Fig. 4.12 are shown in Fig. 4.13 and are highlighted here as they exhibit the three dominant wear mechanism observed for the He ion implanted films. The largest degree of wear was observed for the as-deposited Au film with wear depths approaching 1.5 µm, nearly the full Au film thickness, leaving approximately 300

nm Au thickness in the wear track. Large positively displaced volumes (regions in red) are observed at the end and near the center of the as-deposited Au film in Fig. 4.13a. This is indicative adhesive Au film transfer onto the pin and then retransferred to the wear surface in the center of the wear track, and plowing pile up or decohesion at the end of the wear track. It should be noted that many of the sliding ECR experiments on as-deposited Au resulted in complete film failure through delamination at the Pt interface, evidenced by SWLI depth profiles and observable to the naked eye, before completing 100 cycles of sliding wear. In contrast, the E =22.5 keV film exhibited both a reduction in wear track width and depth (approximately 0.15 μm) with minimal accumulation of wear debris at the end of the wear track. The topography inside the wear track is also significantly smoother with no evidence of adhesive pull-out of film material and is evidence of a change of wear mechanisms from gross adhesion to fine scale surface abrasion. The E = 1200 keV film wear track exhibited micro-scale surface striations in the direction of sliding indicative of harder third body particles being generated during run in wear, but also showed significant reduction in maximum wear depth of approximately 0.5 μm in comparison to the as-deposited Au film. Both the E = 22.5, and 1200 keV films had significantly reduced wear rates, which are given in the He ion implantation wear rates summary in Fig. 4.15a.

Fig. 4.14 shows 3-D topographical reconstruction from SWLI data of the spherically tipped Au-Cu alloy counterfaces post sliding ECR experiments against the (a) as-deposited Au, (b) He implanted at E = 22.5 keV, $\phi = 1x10^{12}$ cm^{-2}, and (c) E = 1200 keV, $\phi = 1x10^{16}$ cm^{-2} films whose CoF and ECR, and wear track topography are shown in Figs. 4.12 and 4.13, respectively.

The counterface post sliding against the as-deposited Au film, Fig. 4.14a, shows a large volume (8239 μm^3) of adhered material transferred from the Au film that is in agreement with the rough wear track surface and adhesive pullout observed in Fig. 4.13a. In contrast, the counterface coupled with the E = 22.5 keV film, Fig. 4.14b, revealed no adhesive film transfer but had a worn flat at the contact point and had a negative net volume transfer of -14 μm^3 that is in agreement with the aforementioned fine abrasive wear mechanism and smoother wear track surface shown in Fig. 4.13b. The counterface coupled to the E = 1200 keV film in Fig. 4.14c revealed a significant reduction in adhered material volume (263 μm^3) in comparison to the as-deposited counterface. In addition, the counterface contains surface striations matching those found in the wear track in Fig. 4.13c, and small regions of positive wear that are likely

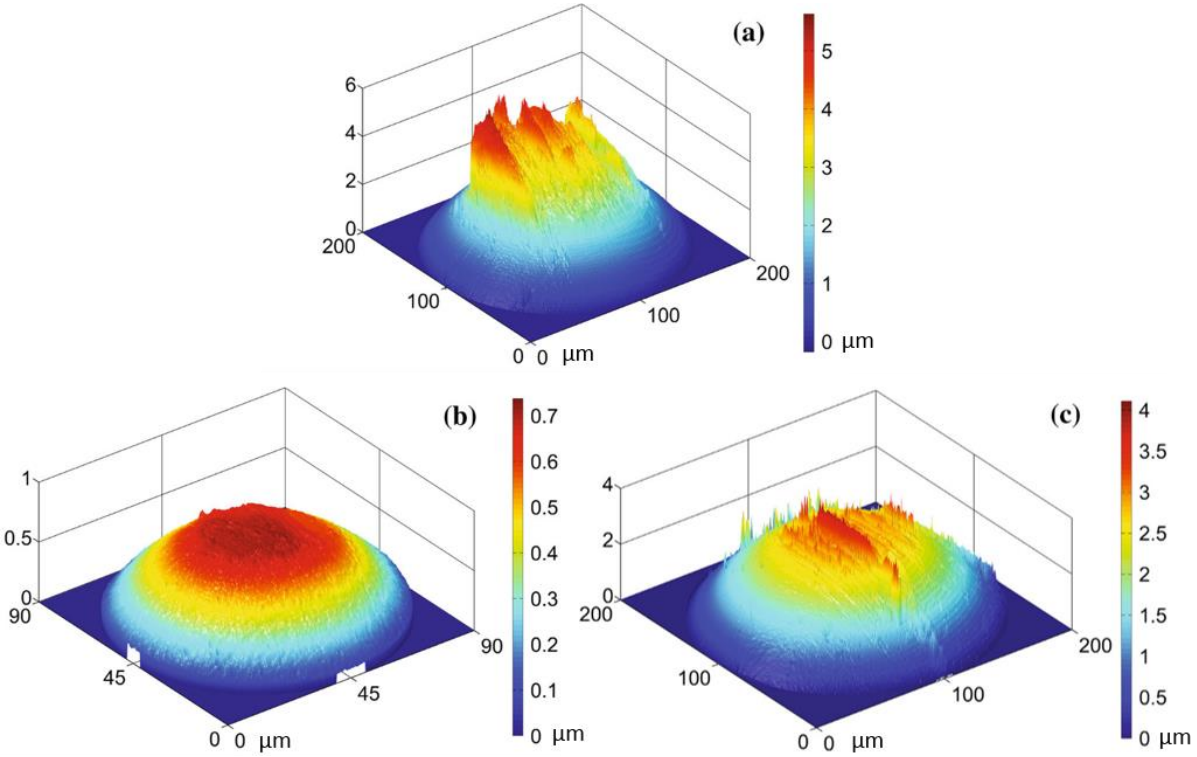

Fig. 4.14: SWLI 3-D topographical reconstruction of Au-Cu alloy pin surfaces after 100 sliding ECR cycles for (a) as-deposited e-beam Au, (b) Au implanted with He ions at E = 22.5 keV, ϕ = $1x10^{12}$ cm^{-2}, and (c) E = 1200 keV, ϕ = $1x10^{16}$ cm^{-2}.

adhered hard third body debris generating the micro-abrasion wear mechanism.

The specific wear rates of single energy and multiple energy He ion implantation conditions listed in Table 4.2 and are plotted in Fig. 4.15a&b, respectively, with the average as-deposited pure e-beam Au wear rate marked by the dashed line. Although some single energy implant conditions and many of the multiple energy implant conditions resulted in a two order of magnitude reduction in specific wear rate, a direct correlation to implant conditions is difficult to determine. There is potentially a bimodal distribution in wear rates with the mean implantation energy as the single implant energies of 45 and 250 keV at each fluence investigated, as well as the multiple energy implant conditions incorporating 45 keV He ions (samples 31-34, Fig. 4.15b), resulted in no appreciable decrease in Au film wear rates.

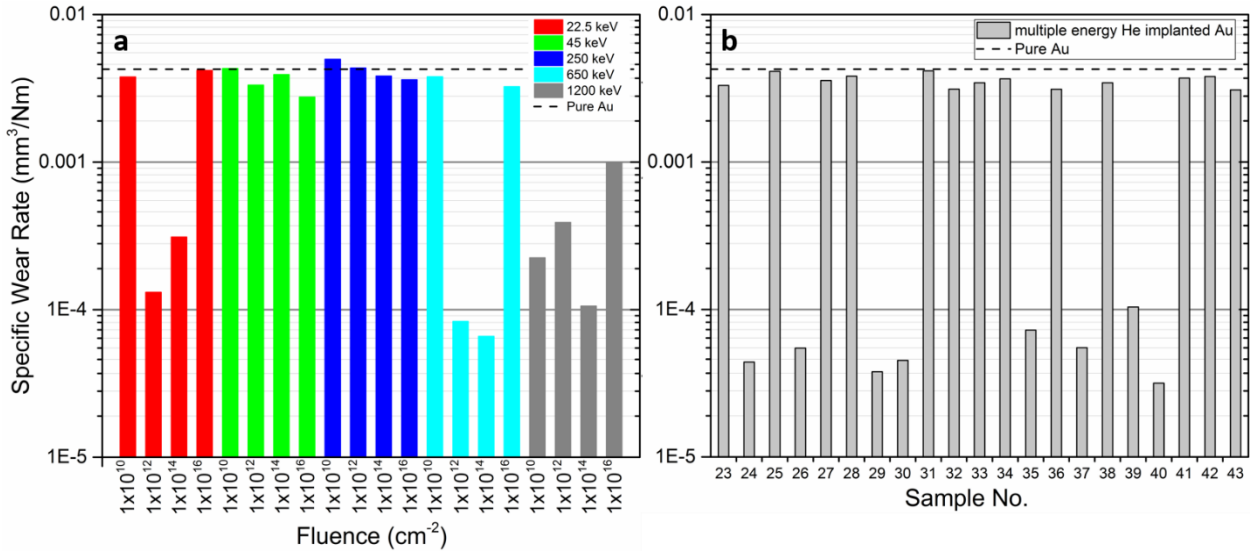

Fig. 4.15: Specific wear rates for (a) single energy He ion implantation conditions and (b) multiple energy He ion implantation conditions in comparison to as-deposited pure e-beam Au.

4.3.3 Correlations of Adhesive Wear and Sliding Friction

Although a direct correlation of specific wear rate to either He implant variable of energy or fluence could not be determined, an evaluation of wear mechanisms can be made by plotting the net volume transfer of material to the Au-Cu alloy counterface versus the mean coefficient of friction, as shown in Fig. 4.16a&b for single energy and multiple energy implant conditions, respectively. For the single energy implant conditions, there is a clear segregation of the data promoting a correlation of reduced adhesive transfer with reduced mean coefficient of friction, although two outlier data points are observed. The same correlation is observed to be even more operative for the multiple energy implant films in Fig. 4.16b. Although it cannot be stated explicitly from just plots such as these whether reduced friction is a result of reduced wear, or vice versa, it can be combined with the topographical evidence in Figs. 4.13 and 4.14. The analysis of the wear track topography and the coupled Au-Cu alloy counterfaces identifies that the main mechanism of increased wear is that of gross adhesion. In a classical static Hertzian contact stress analysis for the experimental conditions implemented and assuming a

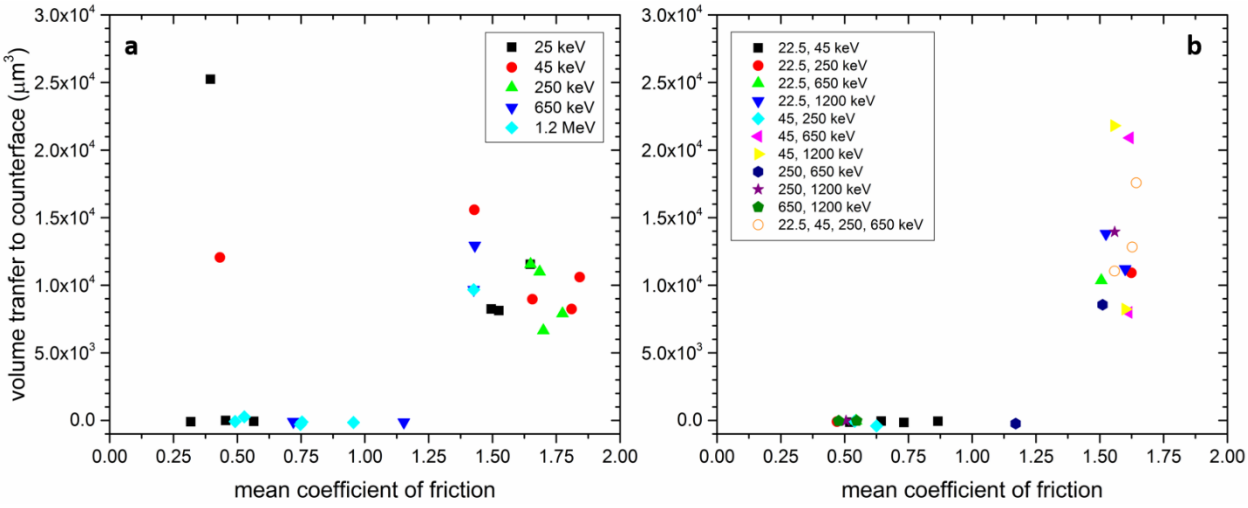

Fig. 4.16: SWLI determined integrated volume transfer to Au-Cu alloy counterface versus mean coefficient of friction for 100 sliding cycles for (a) single energy He ion implantation conditions and (b) multiple energy He ion implantation conditions.

Poisson's ratio of 0.44 for both the Au-Cu alloy and e-beam films, and elastic moduli of 110 GPa for the Au-Cu alloy and 79 GPa for pure polycrystalline Au, a maximum initial contact stress of 292 MPa is predicted. This is slightly greater than the yield strength of similar grain size Au films of 236 MPa, [13], and when considering the stress amplifications due to surface asperities the pure e-beam Au sample is expected to experience large surface plastic deformation and real to apparent contact area ratios. These tribocouple conditions with increased real to apparent contact area are what lead to both increased adhesive wear and friction due to increased interfacial contact area, and the change in wear mechanism and which material parameters lead to it, is what is identified by Fig. 4.16.

4.4 Sliding-induced Subsurface Deformation of He implanted Samples

To investigate the change in wear mechanisms between as-deposited Au film and He ion implanted films described in Figs. 4.12 - 4.14, cross-sectional TEM specimens were locally FIB milled from the center of the wear track and parallel to the direction of sliding to determine the respective microstructural evolution in response to tribological stresses. Figs. 4.17a,c,e show HAADF STEM images of the film cross-sections with corresponding near surface BF-TEM images shown in Fig. 4.1b,d,f. The remaining worn film of the as-deposited Au exhibited significant

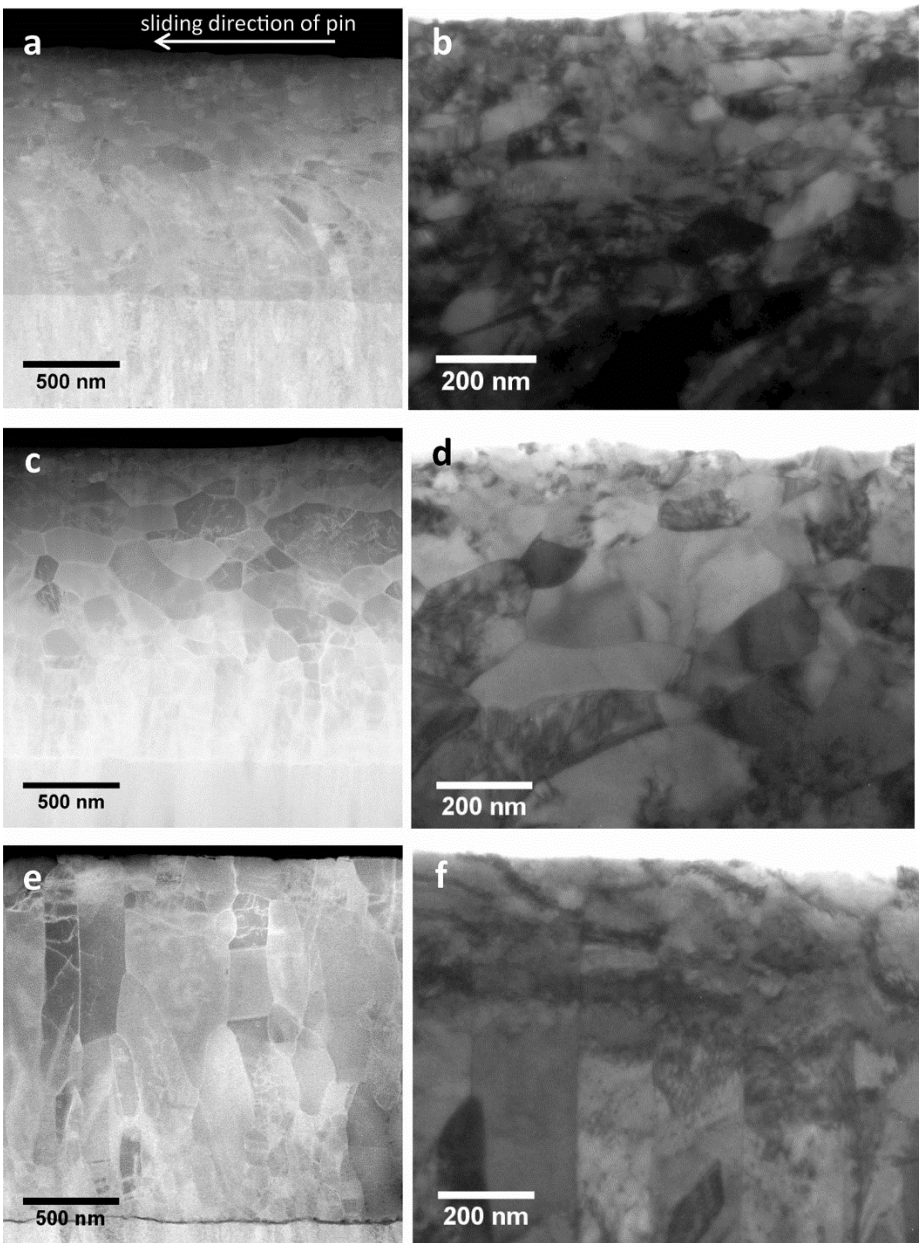

Fig. 4.17: STEM HAADF cross-sectional micrographs after 100 sliding ECR cycles for (a) as-deposited e-beam Au, (c) Au implanted with He ions at E = 22.5 keV, $\phi = 1x10^{12}$ cm^{-2}, and (e) E = 1200 keV, $\phi = 1x10^{16}$ cm^{-2} with corresponding BF TEM images of the near surfaces of the same cross-sections in (b, d, and f). The as-deposited cross-section was taken from a point of maximum wear depth in the track to avoid analyzing retransferred material from the pin.

grain refinement, grain bending in the direction of sliding, and dislocation density in comparison to the unworn cross-section in Fig. 4.3a revealing that subsurface tribological stresses were significantly greater than the film yield strength throughout the film thickness.

Grain refinement was most significant in the top 100 nm of the film with grain sizes on the order of 10-50 nm visible in the BF TEM image in Fig. 4.17b with grain sizes increasing slightly nearer the Au/Pt interface. The He implanted at E =22.5 keV wear STEM cross-section image, Fig. 4.17c, revealed a more equiaxed grain structure compared to the unworn columnar structure in Fig. 4.3b, and significantly less grain refinement in comparison to the worn as-deposited cross-section. Grain sizes in the upper half of the film were on the order of 200-500 nm, with slightly decreasing grain sizes extending to the Au/Pt interface. Higher magnification BF-TEM at near surface of the same film given in Fig. 4.17d revealed similar nanocrystalline grain sizes in the top 100 nm as the as-deposited film. In contrast, the He implanted at E = 1200 keV film, Fig. 4.17e, retained a predominantly columnar grain structure as that of its unworn condition in Fig. 4.3c. The near surface BF-TEM image of the film, Fig. 4.17f, revealed a high density of dislocation cells/networks in the upper 200 nm however no evidence of a nanocrystalline surface layer similar to those in Fig. 4.17b&d was found in this specimen. The observed reduction in grain refinement of the He implanted films shown in Fig. 4.18c&d corresponds to a reduction in the integrated plastic strain accumulation in comparison to the highly deformed pure e-beam Au film, and can be thought of stored work. Classical studies of metallic friction by Rigney & Hirth [14] revealed that the magnitude of the coefficient of friction can be related to the energy lost as heat and stored in the plastic deformation of the softer metal in a sliding tribocouple. This agrees with the observed microstructures in Fig. 4.18 and the reduction in CoF of these He implanted film from 1.5 to approximately 0.5 in comparison to the as-deposited Au, Fig. 4.12. The reduction in plastic strain accumulation in these He implanted samples is expected to be due the Orowan strengthening mechanism and increased

film hardness from He induced cavities as described in section 4.2.2.

High magnification near surface region HAADF STEM images of the worn cross-sections of He implanted at E = 22.5 keV, $\phi = 1x10^{12}$ $cm^{-2}$and E = 650 keV, $\phi = 1x10^{14}$ cm^{-2}conditions as well as near the Au/Pt interface of the E = 1200 keV, $\phi = 1x10^{16}$ cm^{-2} film highlighting He cavity evolution due to tribological stress are shown in Fig. 4.18a,b, and c, respectively. These images can be compared to the unworn microstructures of the same films in given in Fig. 4.4. The E = 22.5 keV film exhibited a noticeable increase in areal density and mean diameter of the He cavities in the near surface nanocrystalline region shown in Fig. 4.17b. The near surface of the E = 650 keV film revealed a similar increase in mean diameter of He cavities, however grain refinement of the captured region containing these cavities was isolated to an approximately 50 nm thick top layer with largely undeformed Au grains at increasing depth. Although the E = 1200 keV film did not reveal any observable He cavities in the near surface, an increase in cavity density was observed at the Au/Pt interface as shown in Fig. 4.18c. The observed increase in mean diameter and areal density of He cavities could be due to He diffusion from previously unobservable locations, such as dislocations, vacancies, and interstitial sites, or from dislocation

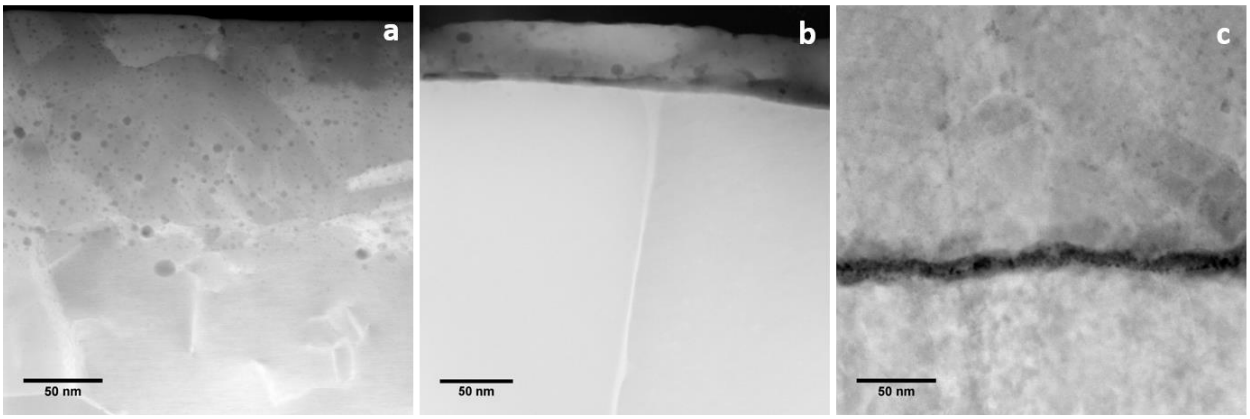

Fig. 4.18: HAADF STEM cross-sectional micrographs He ion implanted Au films after 100 sliding ECR cycles at near surface of implant conditions of (a) E = 22.5 keV, $\phi = 1x10^{12}$ cm^{-2}, (b) E = 650 keV, $\phi = 1x10^{14}$ cm^{-2}, and (c) at the Au/Pt interface of implant condition E = 1200 keV, $\phi = 1x10^{16}$ cm^{-2}.

intersection and trapping during deformation. The high density of He cavities in the nanocrystalline regions of the E = 22.5, and 650 keV films could be evidence of nanocrystalline stabilization that can also act to reduce friction as has been observed for nanocrystalline Ni [15]. The proposed mechanism of reduced friction for nanocrystalline surface regions is a transition from dislocation to grain boundary sliding mediated plasticity whereby the rate of shear accommodation is described by Raj and Ashby [16] and can localize shear accommodation and plastic deformation. This mechanism could be enhanced by the aforementioned preference of He to localize in semi-coherent interfaces and grain boundaries discussed in section 4.1.2 and is hypothesized to increase the shear strain rate accommodation of Au grain boundaries by locally decreasing grain boundary cohesion and stabilizing them from stress assisted grain growth.

4.5 Evaluation of Au and Ar Ion Implantation

To extend the analysis of ion implantation effects on e-beam deposited Au films and to determine if defect structures induced by ion implantation alone are capable of improving sliding friction and wear, films were implanted with Au ions at E = 2800 keV, $\phi = 1x10^{10}$ cm^{-2} with an implantation range of 186 nm and straggle of 78 nm. Au ion implantation into Au will yield high density of defect structures including self-interstitials, vacancies, and potentially amorphous regions, however it will not produce stable cavities as was observed for He ion implantation. Results of SRIM displacement damage modelling predict approximately $5.3x10^4$ vacancies per incident Au ion at E = 2800 keV. Typical sliding coefficient of friction and ECR response of the Au ion implanted e-beam Au is shown in Fig. 4.19. Similar to the as-deposited

Au specimen in Fig. 4.12, the ECR quickly stabilized to a steady value, approximately 20 mΩ. The friction response however exhibited no run in behavior and quickly approached values of approximately 1.8 before visible film delamination occurred and the counterface began sliding on the Pt adhesion layers and retransferred material in the wear track similar to that shown in Fig. 4.13a. The ECR also drastically increased in variance during film delamination failure, around cycle 65, before much of the retransferred Au material was plowed free of the wear track. This response was repeatable over several experiments and indicates that introducing a high density of ion induced point defects and other defect structures is not sufficient enough strengthening to improve upon e-beam Au friction and wear, and could potentially accelerate failure.

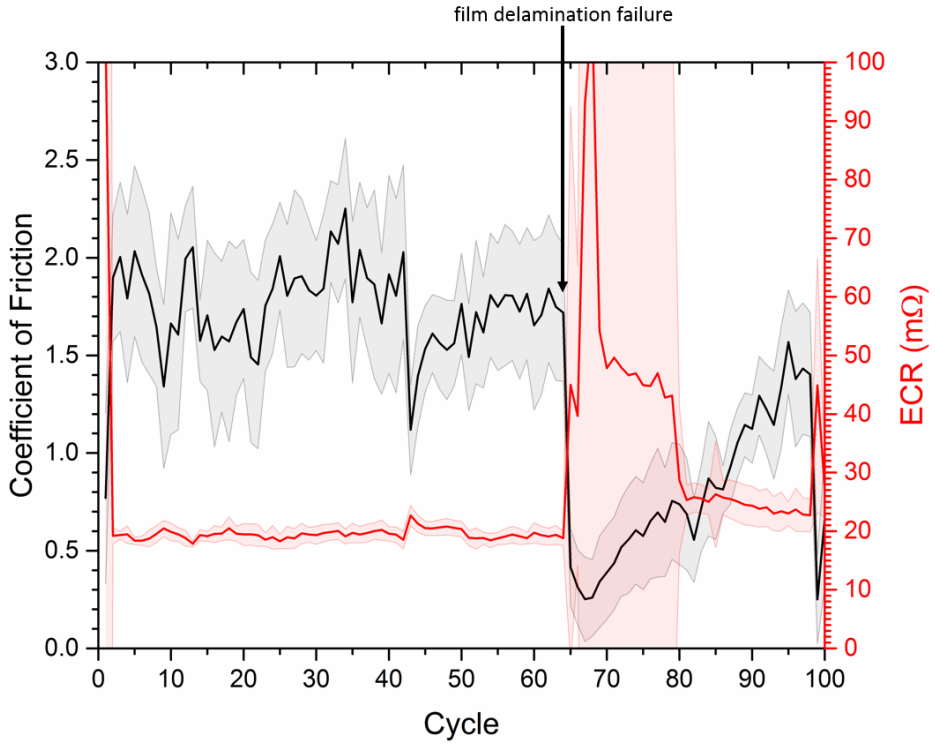

Fig. 4.19: Coefficient of friction and ECR data per sliding cycle for e-beam Au implanted with Au ions at E = 2800 keV, $\phi = 1x10^{10}$ cm^{-2}. Shaded areas correspond to the average value, solid line, ± 1σ of data collected at 50 Hz.

To evaluate if other noble gas ions could be used to improve tribological performance of Au film sliding ECR contacts, a set of films were implanted with Ar ions and tested under identical sliding ECR experiments. Due to the much greater atomic mass of Ar (39.948 amu), implantation into Au at significant depths would require significantly higher energies than He ions. Also it was demonstrated that very near surface He ion implantation, range of 48 nm for E = 22.5 keV, yielded significant performance gains. For these reasons SRIM tables were used to select an energy for Ar ions that would result in a comparable ion implantation range to that of the E =22.5 keV He ions. Ar implantation was conducted with an energy, E = 170 keV (expected ion range of 59 nm and straggle of 32 nm), to fluences of $\phi = 1x10^{12}$, $1x10^{14}$, and $1x10^{16}$ cm^{-2}. Typical sliding coefficient of friction and ECR of these Ar ion implanted films are shown in Fig. 4.20a&b, respectively. Interestingly the medium fluence condition, $\phi = 1x10^{14}$ cm^{-2}, repeatedly exhibited gross friction similar to as-deposited or wrought Au, while the low and high fluence, specimens resulted in much more stable friction coefficients of approximately 0.5 and 0.65, respectively. The ECR response was most stable for the low fluence Ar implantation condition with an extremely stable value of 14 mΩ while the medium fluence condition showed greater

variance with an average value of approximately 20 mΩ after a run in period of 20 cycles. The high fluence condition ECR response exhibited a large fraction of contact separation in the signal during the first 37 cycles, as indicated by off scale values that were >> 1 Ω, before obtaining an average value near 17 mΩ, although within certain cycles the variance was very high and likely a result of periodic third body debris separation. The specific wear rates from SWLI measurements of the Ar ion implanted films are summarized in Table 4.3 in comparison to as-deposited e-beam Au (0 implantation energy). Although the friction and ECR response of the low fluence Ar implanted sample was exceptional in comparison the as-deposited Au, it exhibited similar wear rates as well as the medium fluence condition. The high fluence Ar implantation condition did however result in a 2 order of magnitude reduction in wear rates in comparison with a very repeatable result. These initial Ar ion implantation sliding ECR results indicate that not only are light noble gas ions, e.g. He, able to improve the tribological performance of Au thin films, but heavier noble elements may also be suitable that can

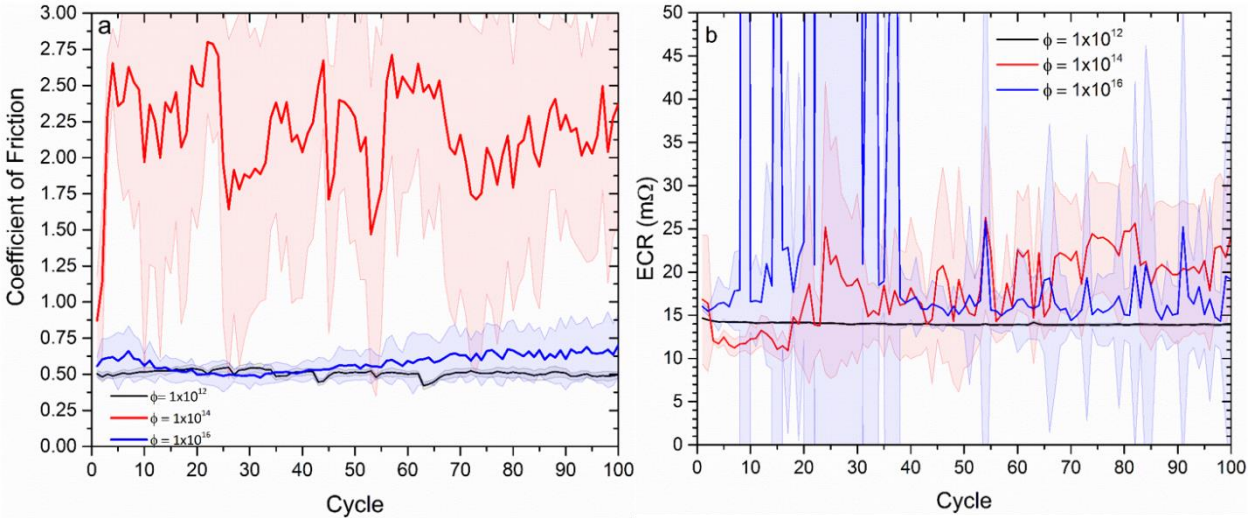

Fig. 4.20: Coefficient of friction (a) and ECR data (b) per sliding cycle for e-beam Au implanted with Ar ions at E = 170 keV to fluences of $\phi = 1x10^{12}$, $\phi = 1x10^{14}$, and $\phi = 1x10^{16}$ cm^{-2}. Shaded areas correspond to the average value, solid line, ± 1σ of data collected at 50 Hz.

potentially produce subsurface nm sized bubbles or cavities.

Table 4.3: Average specific wear rate and standard deviation of as-deposited e-beam Au, and e-beam Au implanted with Ar ions at an energy of 170 keV to varying fluences.

Ar ion energy (keV)	Ar ion fluence (cm^{-2})	Average specific wear rate (mm^3/Nm)	Std. Dev. of specific wear rate (mm^3/Nm)
0	0	$5.25x10^{-3}$	$2.88x10^{-3}$
170	$1x10^{12}$	$5.05x10^{-3}$	$9.99x10^{-3}$
170	$1x10^{14}$	$1.21x10^{-2}$	$8.41x10^{-3}$
170	$1x10^{16}$	$6.44x10^{-5}$	$4.31x10^{-5}$

4.7 Chapter 4 References

1. Parish, C.M. and M.K. Miller, *Aberration-corrected X-ray spectrum imaging and Fresnel contrast to differentiate nanoclusters and cavities in helium-irradiated alloy 14YWT.* Microsc Microanal, 2014. **20**(2): p. 613-26.
2. Demkowicz, M., A. Misra, and A. Caro, *The role of interface structure in controlling high helium concentrations.* Current opinion in solid state and materials science, 2012. **16**(3): p. 101-108.
3. Demkowicz, M.J., R.G. Hoagland, and J.P. Hirth, *Interface Structure and Radiation Damage Resistance in Cu-Nb Multilayer Nanocomposites.* Physical Review Letters, 2008. **100**(13).
4. Kashinath, A., A. Misra, and M. Demkowicz, *Stable storage of helium in nanoscale platelets at semicoherent interfaces.* Physical review letters, 2013. **110**(8): p. 086101.
5. van der Pauw, L., *A method of measuring the resistivity and Hall coefficient on lamellae of arbitrary shape.* 1958.
6. Robic, J., J. Piaguet, and J. Gailliard, *Some measurements of hardness, wear and stresses in ion implanted thin metallic films.* Nuclear Instruments and Methods, 1981. **182**: p. 919-922.
7. Page, T., G. Pharr, J. Hay, W. Oliver, B. Lucas, E. Herbert, and L. Riester. *Nanoindentation Characterisation of Coated Systems: P: S 2-A New Approach Using the Continuous Stiffness Technique*. in *MRS Proceedings*. 1998. Cambridge Univ Press.
8. Saha, R. and W.D. Nix, *Effects of the substrate on the determination of thin film mechanical properties by nanoindentation.* Acta Materialia, 2002. **50**(1): p. 23-38.
9. Tabor, D., *The hardness of metals*. 2000: Oxford university press.
10. Knapp, J.A., D.M. Follstaedt, and S.M. Myers, *Hardening by bubbles in He-implanted Ni.* Journal of Applied Physics, 2008. **103**(1): p. 013518.
11. Li, N., M. Nastasi, and A. Misra, *Defect structures and hardening mechanisms in high dose helium ion implanted Cu and Cu/Nb multilayer thin films.* International Journal of Plasticity, 2012. **32-33**: p. 1-16.
12. Antler, M., *Sliding wear of metallic contacts.* Components, Hybrids, and Manufacturing Technology, IEEE Transactions on, 1981. **4**(1): p. 15-29.

13. Emery, R.D. and G.L. Povirk, *Tensile behavior of free-standing gold films. Part II. Fine-grained films.* Acta Materialia, 2003. **51**(7): p. 2079-2087.
14. Rigney, D. and J. Hirth, *Plastic deformation and sliding friction of metals.* Wear, 1979. **53**(2): p. 345-370.
15. Prasad, S.V., C.C. Battaile, and P.G. Kotula, *Friction transitions in nanocrystalline nickel.* Scripta Materialia, 2011. **64**(8): p. 729-732.
16. Raj, R. and M. Ashby, *On grain boundary sliding and diffusional creep.* Metallurgical transactions, 1971. **2**(4): p. 1113-1127.

CHAPTER 5 ‡

STRUCTURE, MECHANICAL BEHAVIOR, TRIBOLOGY, ELECTRICAL CONTACT RESISTSANCE, AND THERMAL STABILITY OF E-BEAM SYNTHESIZED ZnO HARDENED Au NANOCOMPOSITE FILMS

This chapter presents the experimental results and discussion of microstructure and mechanical behavior relations as well as sliding friction, wear, and electrical contact resistance (ECR) of e-beam synthesized ZnO hardened Au nanocrystalline thin films in the dilute oxide (< 5.0 vol.%) regime. Novel methods and interpretations of grain size stability experiments during in-situ electrical resistivity annealing profiles are also presented for these films. The aim of this chapter is to expand on the previous work of collaborators that have published on sliding ECR behavior of as deposited e-beam Au-ZnO films [1], and initial models developed to describe the electrical resistivity of the composite Au-ZnO films as a function of ZnO concentration [2], and to extend the analysis of the sliding electrical contact resistance, friction, wear, and structural stability of the Au-ZnO thin films in low temperature aging and annealed conditions. As the initial tribological and ECR results of the Au-2 vol.% ZnO film were promising, and it contains similar hardening concentration as that of ASTM B488-11 Type II hard gold, much of the work presented in this chapter is focused on it.

‡ Portions of this chapter are presented based on the publication by N. Argibay, J.E. Mogonye, J.R. Michael, R.S. Goeke, P.G. Kotula, T.W. Scharf, M.T. Dugger, and S.V. Prasad, “On the thermal stability of physical vapor deposited oxide-hardened nanocrystalline gold thin films,” Journal of Applied Physics 117, 145302 (2015) with permission from AIP Publishing.

5.1 Au-ZnO Thin Film Structure and Mechanical Behavior

5.1.1 Grain Size Determination of As Deposited Films

A planar EBSD map of the film surface normal and electron TKD inverse pole figure maps along with SEM micrographs of FIB milled cross-sections are shown in Fig. 5.1 for Au-ZnO films of varying oxide concentration. The EBSD map of the pure Au specimen shown in Fig. 5.1a revealed that the as-deposited e-beam Au yielded a wide range of grain diameter sizes from the order of 20 nm to several μm with a bimodal distribution. The as-deposited pure e-beam Au film also retained a predominantly (111) surface normal texture, as is expected for pure FCC metals deposited at room temperature by PVD methods [3], and also exhibited growth twins observable on the specimen surface for grains on the order of 1 μm. Cross-sections of Au-ZnO films shown in Fig. 5c were FIB milled at multiple locations on each film and subsequently surface ion etched to enhance grain boundary contrast in SEM imaging for horizontal line intercept method measurement of the grain diameters. As seen in Fig. 5c with increasing concentration of ZnO from 0.1 to 2.0 vol.% the average diameter of the Au grains reduces while retaining a columnar grain structure with less than 2.0 vol.% ZnO and also shows evidence of twinning. Although the average grain size was too fine for large area EBSD maps of the 1.0 and 2.0 vol.% ZnO films, small area TKD maps shown in Fig. 5b revealed that the surface normal texture is more random than the pure e-beam Au in Fig. 5a.

Grain size distributions also changed with increasing Au-ZnO concentration from the observed bimodal distribution of the pure e-beam Au. With very dilute additions of ZnO (< approximately 0.5 vol.%) the grain size distribution was still highly variable as seen from a histogram of EBSD data of the 0.1 vol.% film shown in Fig. 5.2, but was well described by a log-

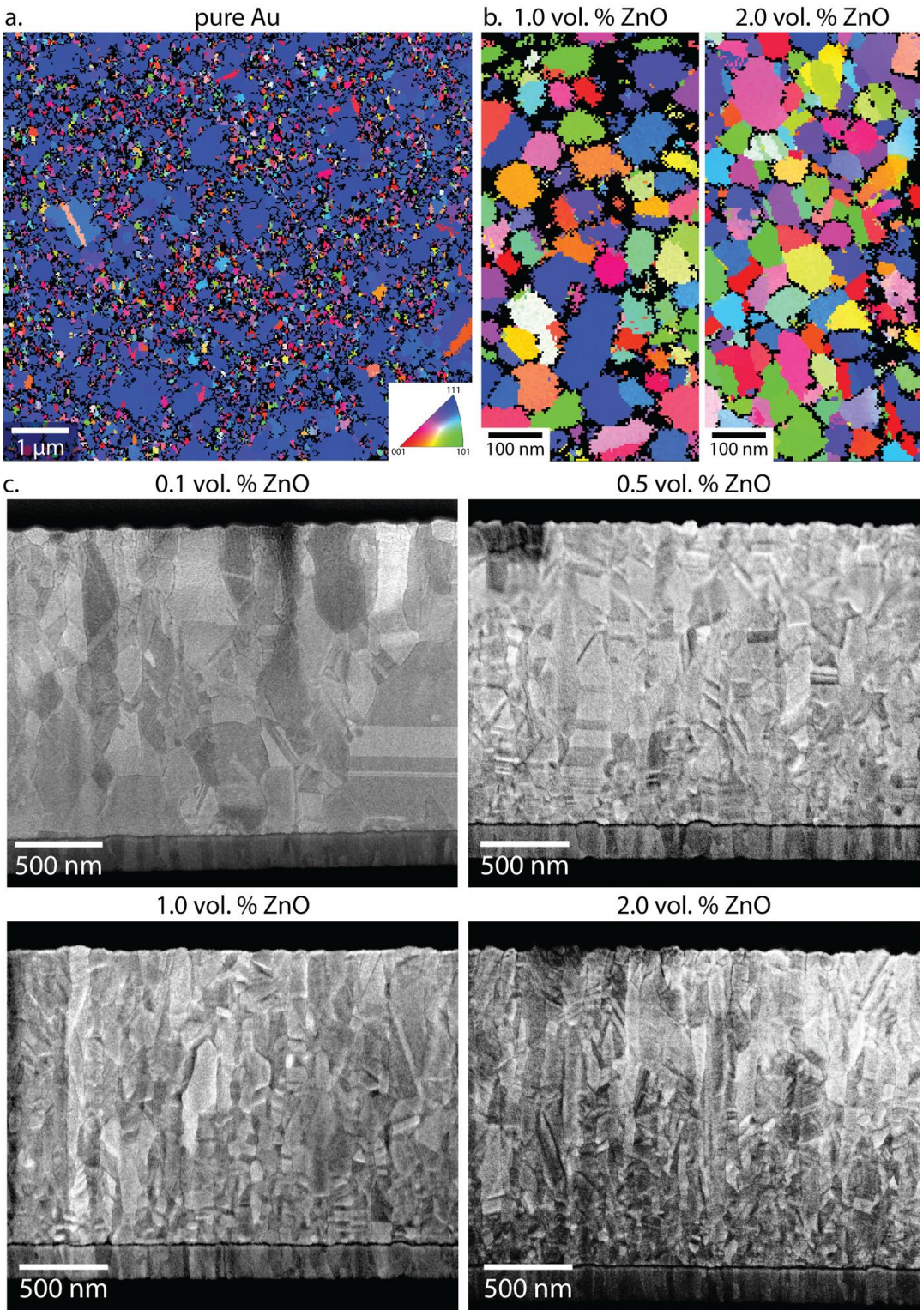

Fig. 5.1: (a) Surface normal electron backscatter diffraction map of 2 µm thick pure Au, (b) SEM surface normal oriented TKD maps of FIB prepared Au-(1.0, 2.0 vol.%)ZnO, and (c) SEM micrographs of FIB milled cross-sections of Au-(0.1, 0.5, 1.0, 2.0 vol.%)ZnO. Grain boundary contrast in (c) was enhanced by ion etching of the cross-section.

normal distribution. For the higher concentrations of ZnO (> 0.5 vol.%) in Fig. 5, although a smaller data set, the grain diameters measured perpendicular to the film surface appear to fit a normal distribution. The grain size results of horizontal line measurements of the Au-ZnO films from EBSD, TKD, and FIB cross-sections are summarized in Table 5.1 along with the calculated diameter of the average grain area assuming a circular cross-section. The grain diameter sizes reported here for EBSD, TKD, and FIB cross-sections were measured transverse in plane parallel to the surface and excluded grains including twin boundaries for reasons to be discussed in section 5.4.

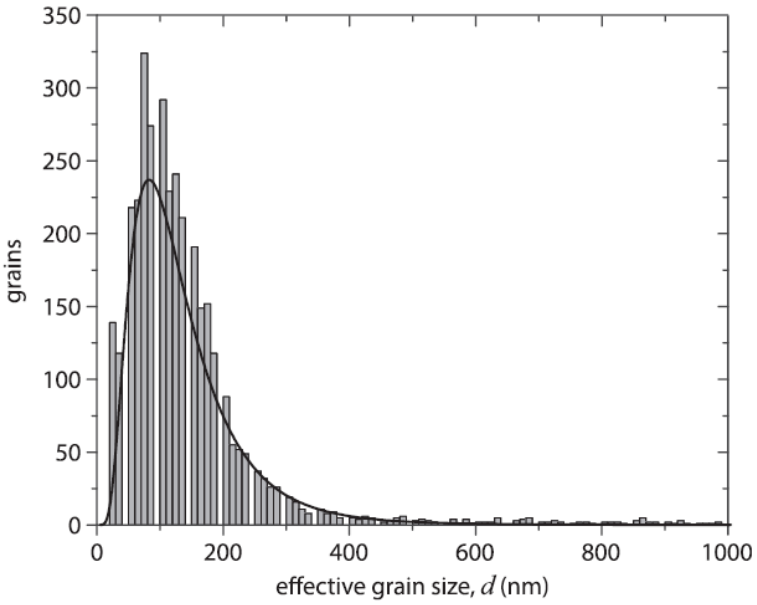

Fig. 5.2: Grain size histogram and fitted log-normal distribution for Au-0.1 vol.% ZnO. Data collected from large area EBSD map.

To further investigate grain size distribution through the film thickness high angle annular dark field and bright field TEM images of different magnification of a FIB prepared cross-section of Au-2.0 vol.% ZnO were collected (Fig. 5.3). In the lower magnification micrograph in Fig. 5.3a it can be seen that the highly equiaxed and nanocrystalline grain

structure begins at the onset of e-beam deposition at the Pt interface and retains this structure throughout the full thickness of the grown film. At higher magnification of an intrafilm location, shown in Fig. 5.3b, there is evidence of significant twining present in the nm sized grains similar to those observed for more dilute ZnO concentrations in Fig. 5.1. High magnification dark field and bright field micrographs of the Au-ZnO/Pt interface in Fig. 5.3c, and 5.3d, respectively, revealed evidence of a thin continuous ZnO layer between the Au-ZnO deposit and Pt adhesion layer. This ZnO film is likely formed post e-beam deposition and not an artifact of deposition as the substrates of the specimens containing the adhesion layers were shuttered in the e-beam chamber until the mass arrival rates of the Au and ZnO crucibles were balanced by QCMs. It is hypothesized that the ZnO film has formed from ZnO at the grain boundaries of the deposited film near the Pt interface as the thermal and epitaxial mismatch strain would be greatest there and assist in the diffusion of ZnO from the Au to minimize stress.

Table 5.1: Grain size results for various ZnO concentrations. Line intercept method reported as the arithmetic average diameter, d, and area-weighted average diameter in the surface normal plane with respective standard deviations.

vol.% ZnO	Imaging method	Avg. grain size, d (nm)	Std. dev. (nm)	Diameter of avg. grain area (nm)	Std. dev. (nm)	Grains
0.1	FIB/ion etch	320	385	498	793	73
0.1	EBSD	204	434	479	1476	3572
0.5	FIB/ion etch	105	50	115	116	49
1	FIB/ion etch	77	32	83	76	129
1	TKD	42	29	51	61	201
2	FIB/ion etch	71	28	76	67	35
2	TKD	46	28	54	56	127

To further determine the distribution of ZnO as a result of e-beam co-deposition, high resolution HAADF TEM micrographs of 2.0 and 10 vol.% ZnO film cross-sections (Fig. 5.4) were

performed with full X-ray spectra acquired for each pixel in the image array and the spectral image data analyzed using multivariate statistical analysis (MSA) methods to extract chemical components location and to reduce spatial spectral noise [4]. For the 2.0 vol.% film shown in Fig. 5.4a, ZnO appears to be well distributed, concentrated as a thin film at the Au grain boundaries and intragranularly dispersed as ZnO particles that are on the order of single of nm's in diameter appearing as darker contrast spots in the Au. For the 10 vol.% ZnO film shown in Fig. 5.4b&c, the ZnO at the Au grain boundaries has coalesced and formed larger grains while

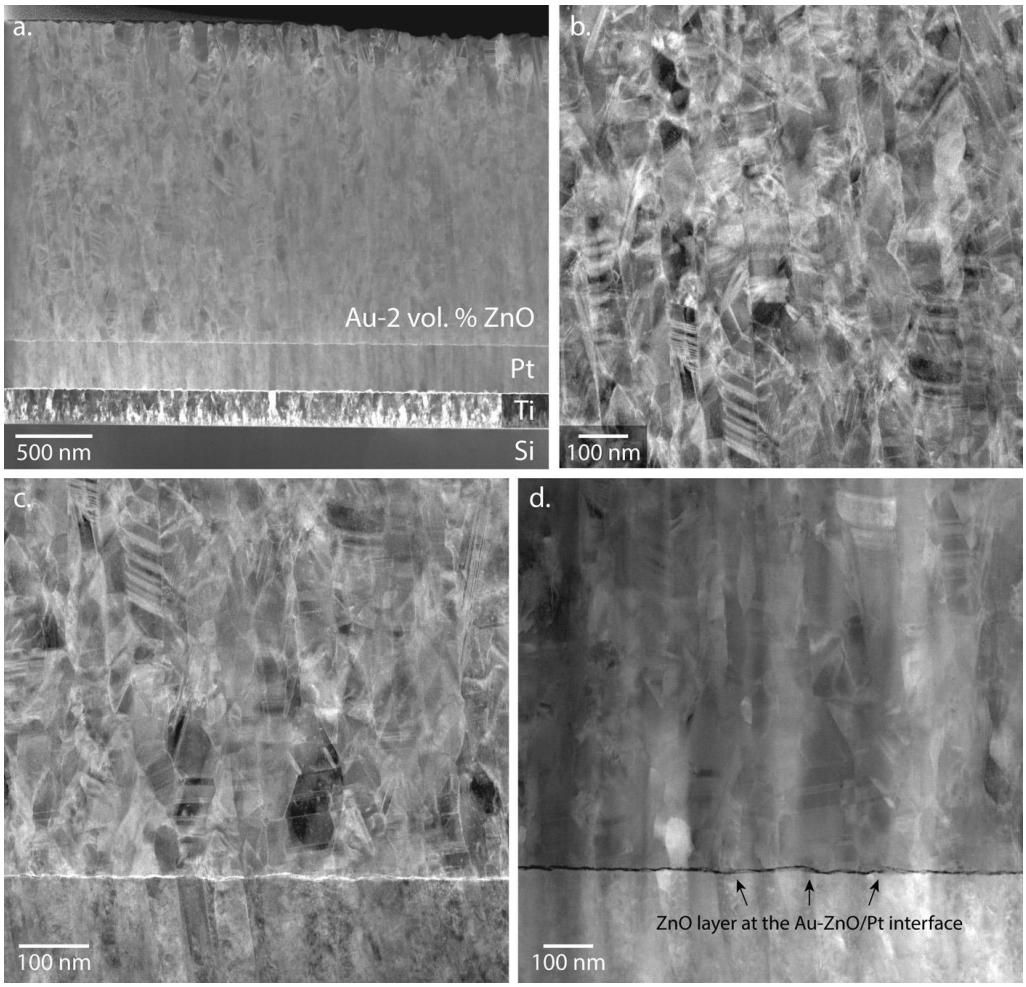

Fig. 5.3: (a-c) Annular dark field and (d) bright field TEM micrographs of as deposited Au-2.0 vol.% ZnO at varying magnifications. The bright film at the Au-ZnO/Pt interface of the dark field image in (c), and the dark film at the Au-ZnO/Pt interface of the bright field image in (d) correspond to a ZnO layer.

the ZnO intragranular particle density has also increased. This suggests that there is a ZnO concentration somewhere in the dilute regime (2.0< vol.% ZnO <10) at which the deposited ZnO at the Au grain boundaries is no longer homogeneously distributed as a boundary film but begins to coalesce and form larger grains.

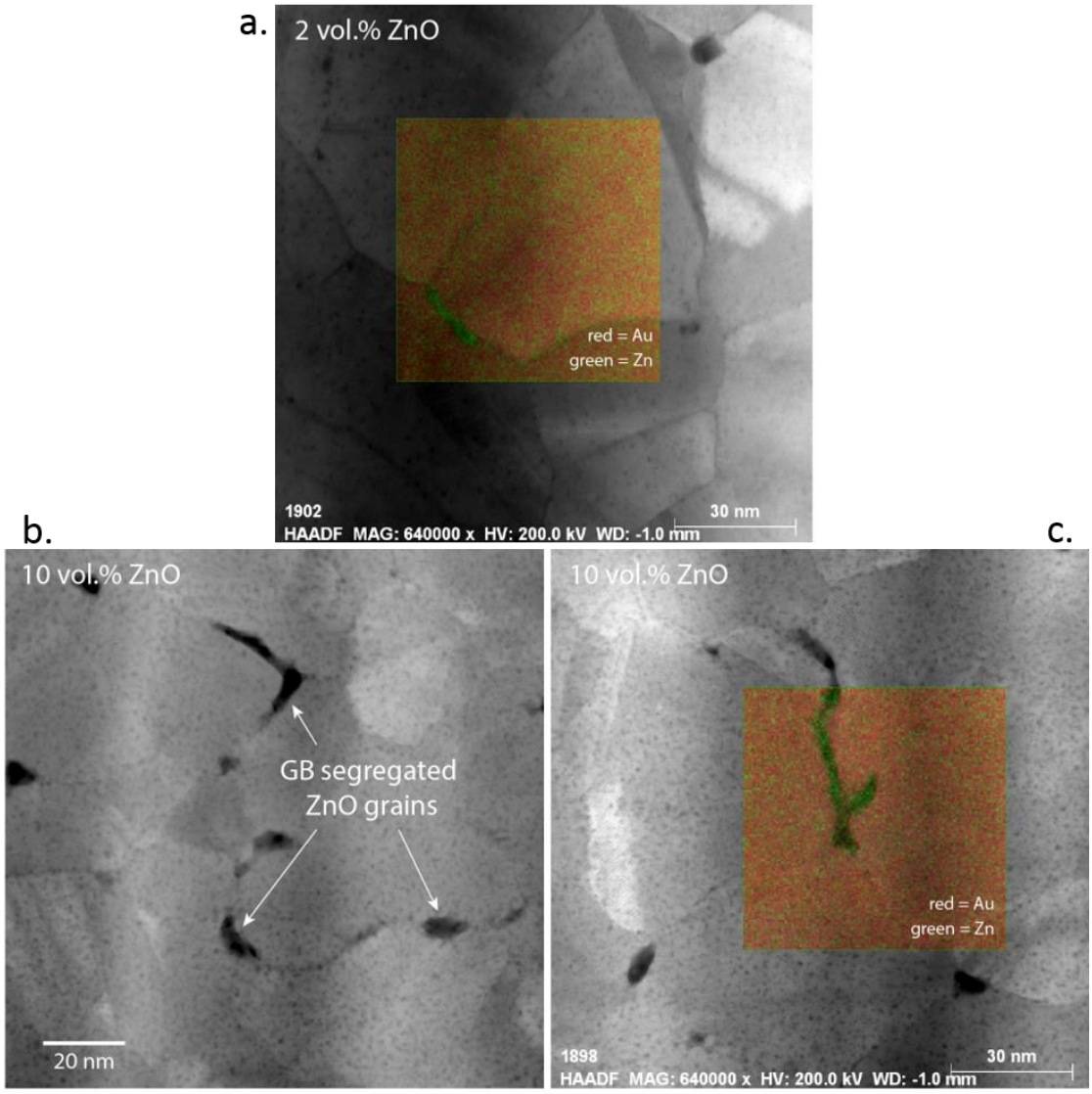

Fig. 5.4: High angle annular dark field STEM micrographs of (a) Au-2 vol.% ZnO and (b&c) Au-10 vol.% ZnO highlighting the grain boundary segregated ZnO and intragranular ZnO particles. Color overlays in (a&c) are MSA derived component images from collected x-ray spectra.

5.1.2 Nanoindentation Hardness and Strengthening Mechanisms

Fig. 5.5 shows the nanoindentation hardness and P/S^2 values of dilute ZnO hardened Au films as a function of indentation depth, where P is the indenter load and S the contact stiffness, both of which are directly measured variables. The P/S^2 is included as it is a value comparable to hardness and can indicate if surface roughness or plastic pile up effects are skewing the measured hardness in shallow indentation [5], or if substrate or other sublayers are significantly altering results [6]. The data has been plotted as the mean of 16 indentations

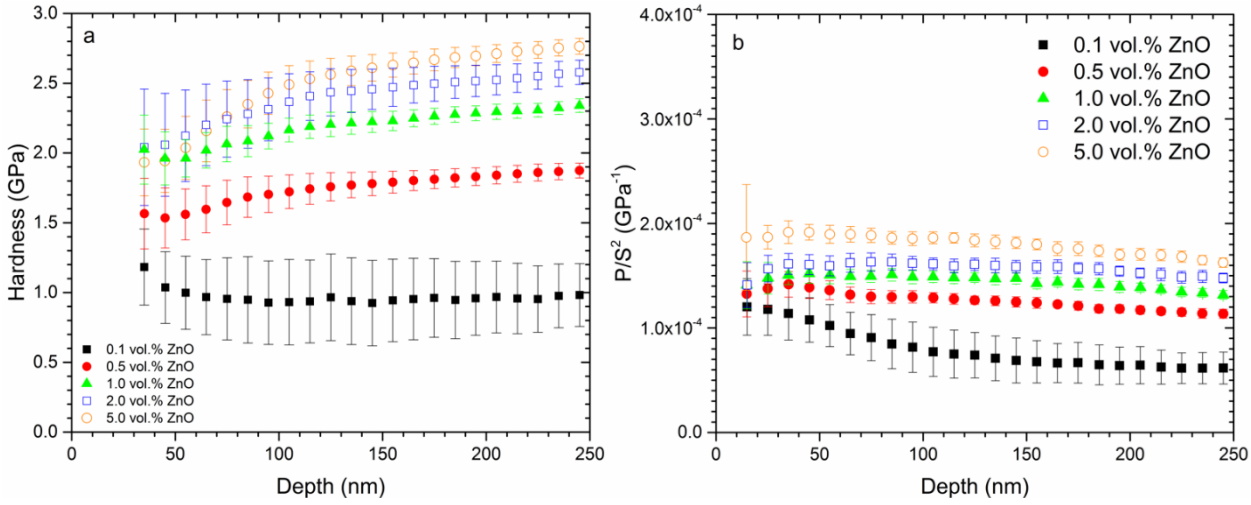

Fig. 5.5: Nanoindentation hardness (a), and indenter load normalized by the square of contact stiffness, P/S^2 (b) as a function of indentation depth of Au-(0.1, 0.5, 1.0, 2.0, 5.0 vol.%)ZnO films with standard deviation as error bars for data binned at intervals of 10 nm indentation depth.

with data from indentation depths < 30 nm excluded due to expected indenter tip radius effects on the results. It is evident from Fig. 5.5a that with increasing ZnO concentration the composite hardness of the films increased, as well as reducing the variance of the measured results. The highest variance in hardness was for the 0.1 vol.% ZnO film and is likely due to the highly variable log-normal grain size distribution (Fig. 5.2) and the fact that the indentation locations were not site specific, but taken in a 4x4 matrix of defined spacing near the center of the film. The P/S^2 values shown in Fig. 5.5b agree with the trend of increasing hardness with increasing

ZnO concentration and are fairly constant with indentation depths up to 250 nm suggesting that the data collected was not significantly affected by surface pile up or sublayer contributions. For this reason subsequent analysis of strengthening mechanisms in the dilute ZnO films used the average hardness values from indentation depths of 100-250 nm in accordance with ASTM E2546 methods of reporting hardness values of thin metallic films and are summarized in Table 5.2. The approximate elastic modulus values of the films, E_f, are also reported in Table 5.2. Film moduli were calculated from the measured reduced modulus, E_r, using Eq. 5.1 by assuming an elastic modulus of $E_i = 1140$ GPa and a Poisson's ratio of $\nu_i = 0.07$ for the diamond Berkovich indenter, and a Poisson's ratio of $\nu_f = 0.44$ of pure polycrystalline Au for each film.

$$\frac{1}{E_r} = \frac{1-\nu_f^2}{E_f} + \frac{1-\nu_i^2}{E_i} \tag{5.1}$$

The calculated elastic moduli of the films listed in Table 5.2 are comparable to values of pure polycrystalline Au, (~ 79 GPa), and reports of nanoindentation results on thin film polycrystalline Au 1 µm thick of 94 GPa [7] suggesting that the dilute ZnO regime does not yield a composite elastic moduli.

The average reported hardness values listed in Table 5.2 are plotted against grain size (calculated from Eq. 5.8 based on the measured resistivity of the films - the validity of which is explained in greater detail in section 5.3.2), and against volume fraction of ZnO in Fig. 5.6a and Fig. 5.6b, respectively. Also plotted in Fig. 5.6a&b is the expected Hall-Petch (H-P) contribution to hardness calculated using the classical H-P relation given in Eq. 5.2 and using literature obtained strengthening coefficient for Au thin films of $k_h = 25$ MPa·m$^{1/2}$ [8, 9]. A literature value

for the intrinsic hardness of $H_o = 400$ MPa, based on the hardness of bulk coarse grained Au, was also used for the calculated H-P contribution to hardening [10]. Although the H-P curve is not commensurate with the data shown in Fig. 5.5b, the trend of asymptotic increase in hardness with increasing ZnO concentration is in agreement and indicative that ZnO induced grain refinement is asymptotic. This limit to grain refinement (for 2.0 < vol.% ZnO < 10) is attributed to the observed coalescence and larger grain formation of ZnO at Au grain boundaries at higher concentrations as shown in Fig. 5.4b.

$$H = H_o + k_H \cdot d^{-0.5} \tag{5.2}$$

Table 5.2: Nanoindentation hardness, reduced modulus, and film modulus as a function of ZnO concentration.

vol.% ZnO	Nanoindentation hardness, H (GPa)	Std. dev. in H (GPa)	Reduced modulus, E_r (GPa)	Std. dev. in E_r (GPa)	Film modulus, E_f (GPa)
0.1	0.95	0.29	87.4	3.8	76.3
0.5	1.78	0.09	90.2	2.9	78.9
1.0	2.23	0.07	93.6	2.4	82.2
2.0	2.46	0.15	93.9	3.8	82.5
5.0	2.61	0.10	90.7	2.5	79.4

It is evident from Fig. 5.6a that there is a significant difference between the expected hardness of the Au-ZnO assuming a purely H-P strengthening mechanism and the measured values. There is however evidence of relatively spatially dense nm sized intragranular ZnO particles in the dilute oxide regime, as was shown for the 2.0 vol.% ZnO film in the HAADF TEM micrograph in Fig. 5.4a that could be significant sources of Orowan strengthening and is a novel structural feature of the e-beam synthesized composite. Orowan contributions to film hardness can be approximated by using Eq. 5.3, a modified form of the classical expression

given by Bannuru et al. [10].

$$\Delta H = \frac{2.43MGb}{2\pi\sqrt{1-\nu}} \ln\left(\frac{2r}{r_o}\right)\left(\frac{1}{L-2r}\right) \tag{5.3}$$

In this analysis the following parameters and values were used: a Taylor factor, $M = 1.77$, shear modulus of Au, $G = 27$ GPa, a Burgers vector, $b = 290$ pm, dislocation core radius approximation, $r_o = 4b$, and Poisson's ratio of Au, $\nu = 0.44$. The parameter *r* is the average radius of strengthening particles, in this case intragranular ZnO particles, and the parameter *L* is the edge to edge particle spacing. The hypothesized contribution of Orowan hardening due to intragranular ZnO particles, ΔH, was taken as the difference between the

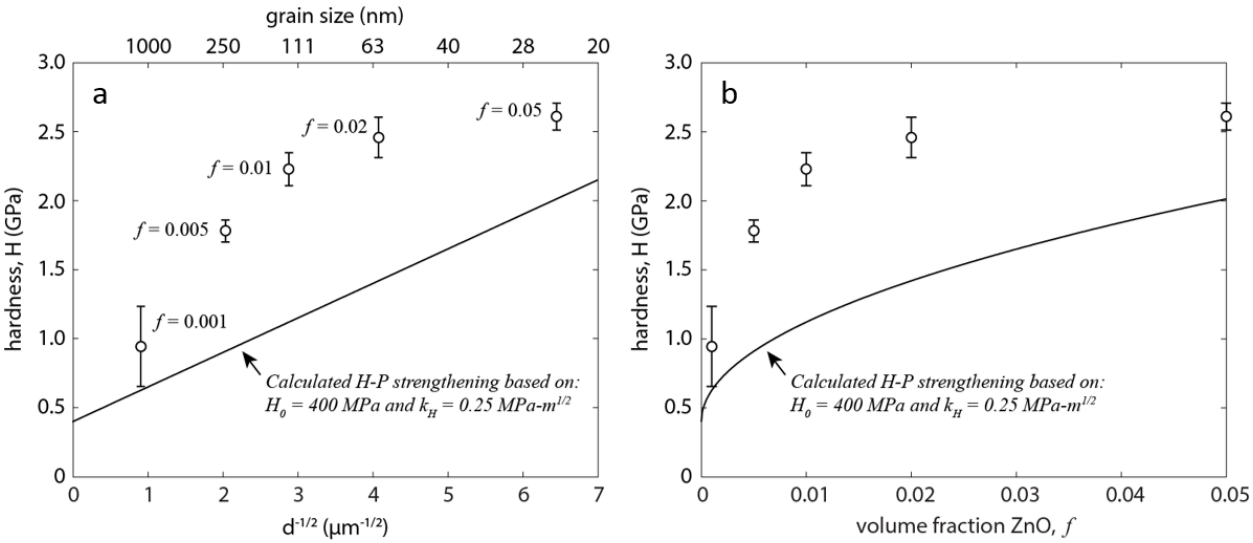

Fig. 5.6: Measured nanoindentation hardness values and calculated Hall-Petch contribution to hardness as a function of (a) grain size calculated from resistivity data in section 5.3, and (b) volume fraction ZnO.

average values of hardness in Fig. 5.6 and the calculated H-P contribution. Assuming that the average particle radius is invariant with ZnO concentration and has a value, *r*, between 1 to 2 nm, which is in qualitative agreement for the 2.0 vol.% and 10 vol.% ZnO micrographs

presented in Fig. 5.4, the required edge to edge particle spacing, *L*, to account for the difference in the measured hardness and expected H-P value varies between 30 nm to 10 nm for ZnO concentrations of 0.1 vol.% to 2.0 vol.% respectively. There are some uncertainties in the Orowan analysis as the increase in hardness is sensitive to the particle radius, *r*, which is difficult to fully characterize without extensive high resolution TEM, the assumption that the H-P and Orowan mechanisms can be directly summed instead of the root of the sum of their quadrature, and parameters such as the Taylor factor, *M*. However the calculated value for particle spacing, *L*, of 10 nm for 2.0 vol.% ZnO is in reasonable agreement with the observed particle spacing in Fig. 5.4a and gives experimental confirmation that hardness contributions, ΔH, from Orowan strengthening are a significant fraction of the measured hardness. Here it is worth mentioning that the Taylor factor used, $M = 1.77$, is not the typical value for FCC metals in uniaxial tension ($M \approx 3.06$) but instead that suggested by Frost & Ashby [11] based on the polycrystal analysis of Kocks [12], and is in good agreement with empirical nanoindentation analysis of oxide dispersion strengthened FCC Ni [13]. Other strengthening mechanisms such as those due to high twin boundary density, which the current analysis excluded from the grain size calculation, cannot be ruled out.

5.2 Tribological and ECR Behavior of As Deposited and Annealed Au-ZnO Films in the Dilute ZnO Regime

5.2.1 Friction and ECR Behavior of Au-ZnO

Typical friction coefficient and ECR results from unidirectional sliding ECR against Au-Cu alloy riders are shown in Fig. 5.7 for as deposited type II commercial Ni HG, pure e-beam Au,

and Au-(0.1, 0.5, 1.0, and 2.0 vol.%)ZnO films. The as deposited commercial Ni HG began at ~0.3 CoF and experienced a short run in period of 20 cycles of increasing friction until entering a region of periodic CoF response from cycle 30-50, and finally reaching a smooth steady state value of ~0.75 after cycle 80. The sliding ECR of the Ni HG was highly variable until approximately cycle 75 with values consistently exceeding 20 Ω. These exceptionally high ECR values in conjunction with the CoF behavior prior to cycle 80 were repeatable over several experiments indicating that a NiO film had likely formed on the surface due to environmental exposure to air. The ECR behavior can be explained as contact separation between the rider and film due to nonconductive third body wear debris generated by run in wear of the thin NiO film. In contrast to the Ni HG film, the pure e-beam Au film exhibited a rapid increase in CoF to ~1.75 commensurate with a highly adhesive and large area of contact until ~ cycle 45 before the CoF variance increased. The initial cycles (< 45) of ECR for the Au film retained a value of ~16 mΩ and low variance in conjunction with the same relatively low variance region in the CoF before increasing and becoming more variable per cycle. This change in CoF and ECR beyond cycle 45 is due to adhesive wear out through the thickness of the Au layer in large regions of the wear track with some retransferred pile up material, as seen in the SWLI maps in Fig. 4.12a, resulting in the rider sliding on Pt/Ti adhesion layers and retransferred worn Au patches that evolve through continued wear. The CoF with increasing ZnO concentration from 0.1-2.0 vol.% resulted in decreasing average CoF and variance as well as more stable regimes of friction throughout the 100 cycles of sliding ECR testing. The average stable ECR values for the 0.1-2.0

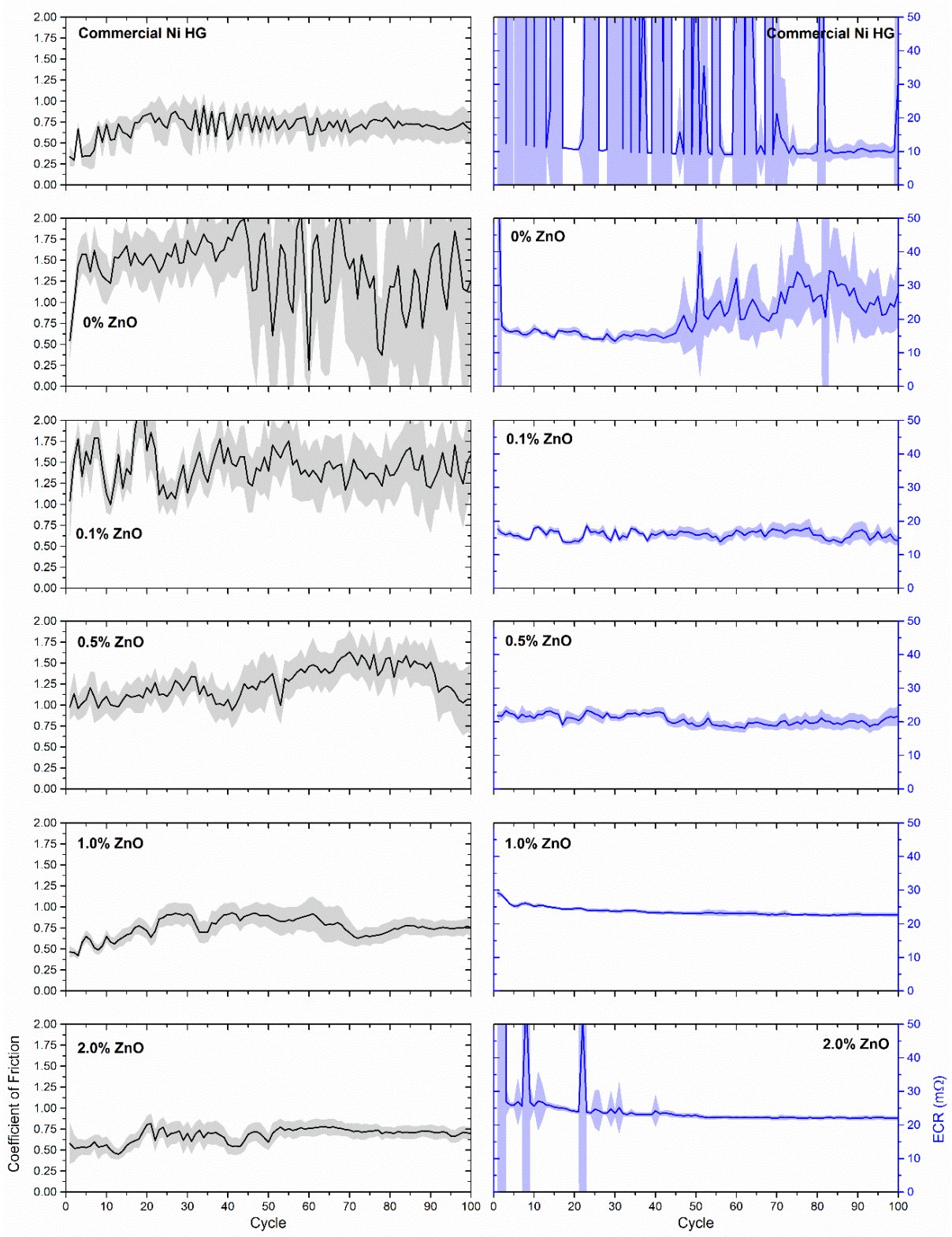

Fig. 5.7: Coefficient of friction and ECR data per sliding cycle for as deposited commercial Ni HG on alloy 52 substrates and 2 µm thick films of Au-(0.0, 0.1, 0.5, 1.0, 2.0 vol.%)ZnO on Ti/Pt adhesion layers on Si substrates sliding against a spherically tipped Au-Cu alloy rider; shaded areas correspond to the average value, solid line, ± 1σ of data collected at 50 Hz.

vol.% films increased with increasing ZnO concentration from ~16 mΩ to ~22 mΩ, respectively, and is likely due to the increase in resistivity of the films with increasing ZnO concentration discussed in subsequent sections. Overall the variance of the ECR has also significantly decreased for all of the dilute ZnO concentrations shown with the exception of the 2.0 vol.% film. In the first 30 sliding cycles of the 2.0 vol.% film, there are large spikes in ECR indicative of a large fraction of contact separation similar to the Ni HG. This ECR response is likely due to ZnO third body debris generated at the onset of wear before being displaced from the wear track as seen in SEM and characterized by EDS and SWLI maps of the same ZnO concentration film on Alloy 52 substrates [1].

Typical friction and ECR results of sliding ECR tests are shown in Fig. 5.8 for type II commercial Ni HG, pure e-beam Au, and Au-(0.1, 0.5, 1.0, and 2.0 vol.%)ZnO films annealed at 250°C for 24 hours in air. The commercial Ni HG interestingly exhibited a significantly reduced steady state CoF and ECR, ~0.25 and 18 mΩ, respectively, in comparison to the as-deposited film. The run in period of slightly higher CoF and ECR lasted for only the first 10 cycles before obtaining the low variance and steady state regime. It is unclear if annealing of the Ni HG at 250°C resulted in significant oxide film or Au grain growth, however the results indicate that the surface wear evolution led to a smooth and conformal contact without large third body debris that can cause the contact separation ECR response seen in Fig. 5.7. The pure e-beam Au friction began in excess of 3.0 while the ECR remained stable near 15 mΩ throughout and is a result of the Au film being completely (visible to the naked eye) detached from the Pt/Ti adhesion layers in the first few cycles. This is the result of gross adhesive wear and film adhesion failure as a result of large grain formation from annealing. The 0.1 vol.% ZnO

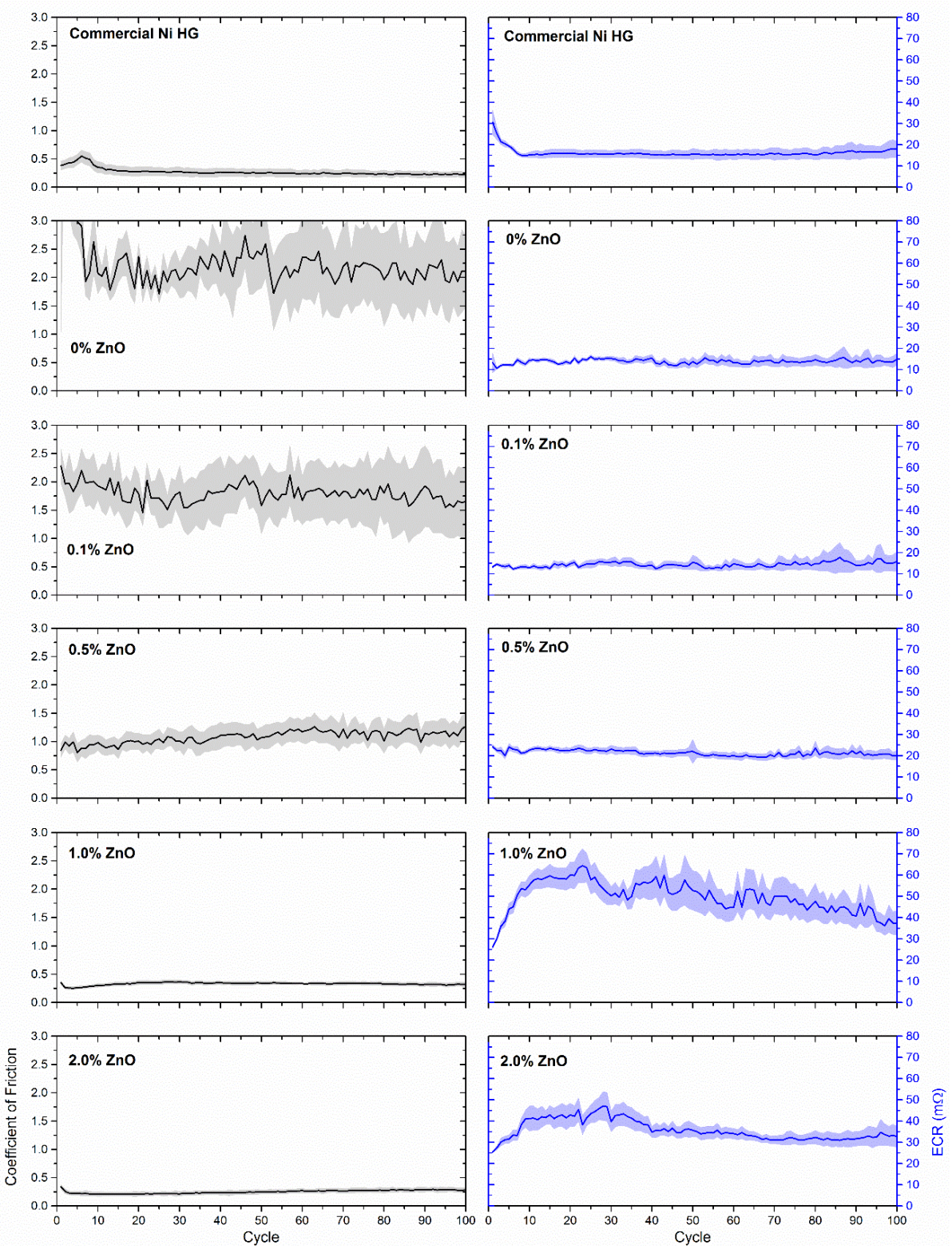

Fig. 5.8: Coefficient of friction and ECR data per sliding cycle for annealed condition of 250 °C in air for 24 hrs of commercial Ni HG on alloy 52 substrates and 2 µm thick films of Au-(0.0, 0.1, 0.5, 1.0, 2.0 vol.%)ZnO on Ti/Pt adhesion layers on Si substrates sliding against a spherically tipped Au-Cu alloy rider; shaded areas correspond to the average value, solid line, ± 1σ of data collected at 50 Hz.

exhibited an increase in CoF in the 250°C annealed condition, likely a result of grain growth, with a similar ECR value as the as-deposited condition, but did not completely fail as did the pure e-beam Au. The 0.5 vol.% ZnO film exhibited similar results to the as-deposited condition although the variance in CoF was decreased. Both the 1.0 and 2.0 vol.% ZnO films interestingly showed significantly reduced and stable CoF values of ~0.25 for the 250°C annealed condition. Their ECR response was also similar, increasing during a run in period over the first 10 cycles and slowly stabilizing to a value near 45 mΩ and 35 mΩ, respectively, over the duration of the experiment. These ECR values are nearly twice that of the as-deposited values and could be a result of a larger concentration of ZnO at the surface due to annealing that is not forming large third body debris resulting in contact separation as seen in the case of the as-deposited 2.0 vol% film in Fig. 5.7. The extremely stable and low CoF of these films corroborates the hypothesis that ZnO has migrated to the surface and is acting to minimize the adhesive contact contribution to friction.

To further investigate the thermal stability of friction and ECR of these films another set of samples were annealed at 350°C for 24 hours in air and typical sliding ECR friction results are shown in Fig. 5.9. Here the commercial Ni HG did maintain a stable CoF < 0.5 however the ECR values are of the first 12 cycles of sliding ECR are 2 orders of magnitude greater than the 250°C annealed film indicative of a thick and uniform NiO film. The ECR did reduce after initial wear broke through the surface oxide but exhibited large spikes again likely due to third body contact separation. The pure e-beam Au specimen, similar to the 250°C condition, completely failed and delaminated from the Pt/Ti adhesion layers in the first few cycles. Both the 0.1 and 0.5 vol.% ZnO films exhibited similar CoF and ECR values as the 250°C annealing condition. The 1.0

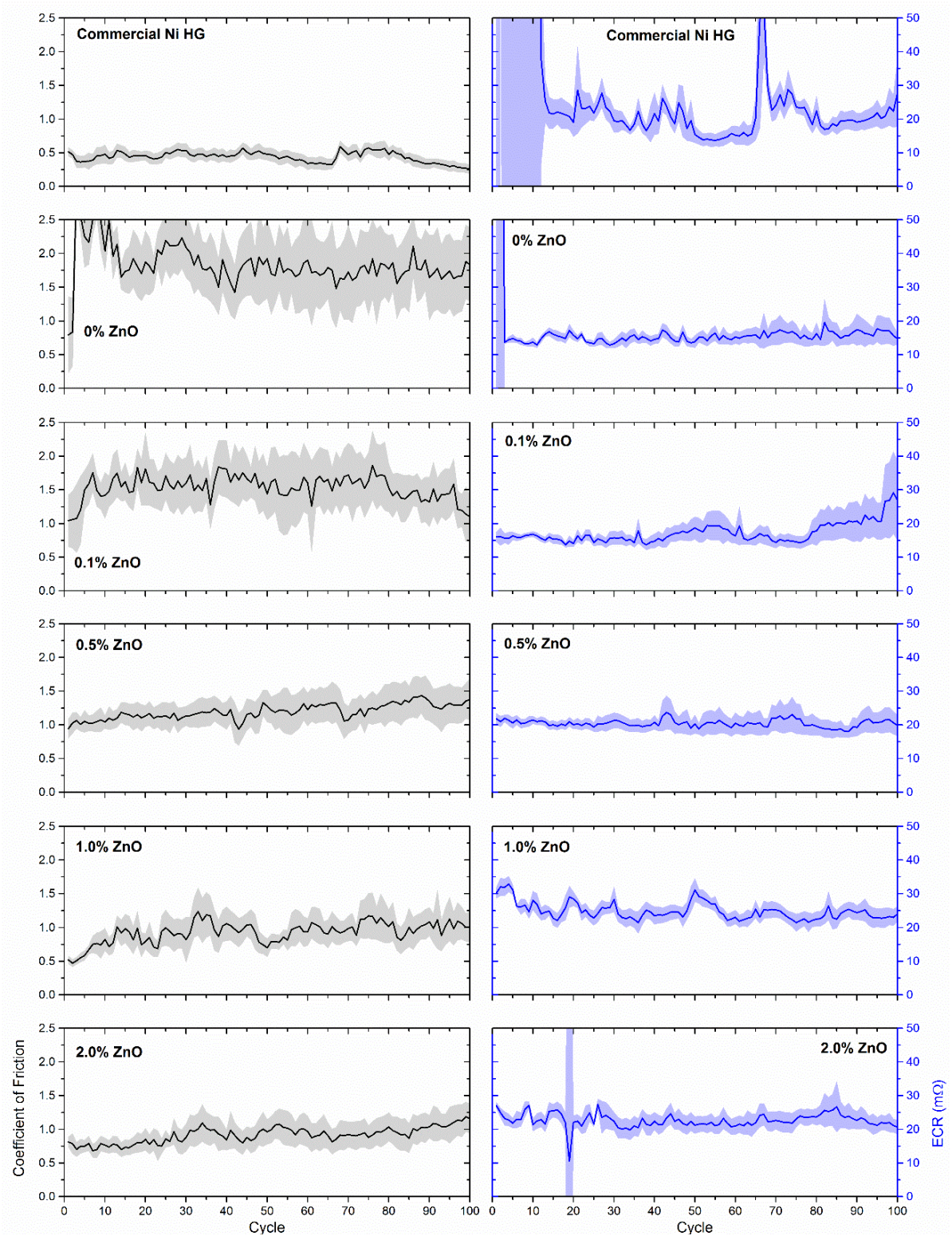

Fig. 5.9: Coefficient of friction and ECR data per sliding cycle for annealed condition of 350 °C in air for 24 hrs of commercial Ni HG on alloy 52 substrates and 2 µm thick films of Au-(0.0, 0.1, 0.5, 1.0, 2.0 vol.%)ZnO on Ti/Pt adhesion layers on Si substrates sliding against a spherically tipped Au-Cu alloy rider; shaded areas correspond to the average value, solid line, ± 1σ of data collected at 50 Hz.

vol.% film showed a marked increase in CoF in comparison to the 250°C annealed condition from ~0.25 to ~0.8, but overall a more stable ECR value near 25 mΩ. The 2.0 vol.% film also exhibited an increase in CoF to a value of approximately 0.8 with the increased annealing temperature, and decrease in ECR to near 25 mΩ, although there were a few points of contact separation during cycle 19.

Overall the friction and ECR response of the 2.0 vol% ZnO film was the most comparable in performance to the commercial Ni HG and outperforming it in regards to more stable ECR in the as-deposited condition. In the annealed condition of 250°C, the 2.0 vol% film exhibited a better and more stable CoF and comparable ECR values, and at the higher 350°C temperature anneal also provided much more stable ECR in comparison to the commercial Ni HG that showed the response of a thick homogeneous NiO film.

5.2.2 Wear Response of Au-ZnO Films and Counterface

Specific wear rates obtained from full wear track SWLI profilometry data on the sliding ECR wear scars of the as-deposited and annealed conditions of 250°C and 350°C of the films are summarized in Fig. 5.10. It is evident that the commercial Ni HG exhibited the lowest wear rate for the as-deposited condition tested here with a value of 9.48×10^{-5} mm^3/Nm, however this could be a reflection of a conformal native oxide film acting to minimize adhesive wear. The 0.1 and 0.5 vol.% ZnO films exhibited similar wear rates to that of the large grain pure e-beam Au for all the conditions tested. This result is interesting in that although the hardness of these films was greater than double that of the pure e-beam Au (~800 MPa), the wear rates were of the same magnitude, suggesting that the higher area fraction of large grains (evidenced by the

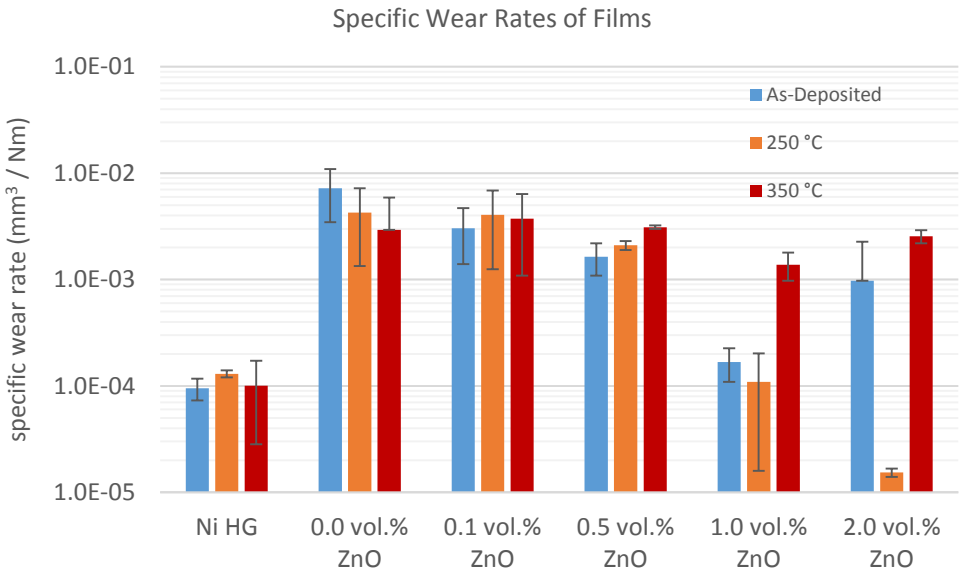

Fig. 5.10: Specific wear rates of commercial Ni HG and Au-(0, 0.1, 0.5, 1.0, 2.0 vol.%)ZnO films for as-deposited condition and annealed conditions of 250°C and 350°C in air for 24 hours.

log-normal distribution in Fig. 5.2) of these very dilute ZnO films yields similar adhesive wear to the pure e-beam Au. The 1.0 vol.% film exhibited similar wear rates to the Ni HG except for an increase by an order of magnitude for the 350°C annealed condition indicating a change in wear mechanisms for that film. The as-deposited 2.0 vol% film showed fairly high wear rates in comparison to what was reported by Argibay et al. [1] who could not calculate a wear rate for nearly identical testing conditions. This could be due to errors in the ZnO concentration due to variability in the e-beam deposition process or other unknown factors. However, the 2.0 vol.% film did exhibit drastically different wear rates for the 250°C annealed condition (1.54×10^{-5} mm^3/Nm), which was the lowest wear rate of all materials. For the films annealed to 350°C, the wear rate significantly increased, and was similar to the other ZnO films suggesting that there is a change in wear mechanisms between these two conditions that is likely surface structure and/or chemistry dependent as Schoeppner and coworkers [14] have determined that

nanoindentation hardness of the 2.0 vol.% film (from the same deposition run) cycled to an annealing temperature of 350°C five times was virtually unchanged from the as-deposited hardness of 2.46 GPa.

The specific wear rates of the Au-Cu alloy riders obtained from the negative volume removed from the surface calculated from spherically fitted SWLI profiles are summarized in Fig. 5.11. The wear rates of the riders are in excellent agreement with the wear rates of the films for each condition tested with the exception of the 350°C Ni HG rider, which is likely due to wear being localized to the rider as the ECR data in Fig. 5.9 indicated a thick and continuous NiO film. The strong correlation of wear rate response between the riders and films suggests that wear mechanisms for both materials are shared and highly dependent on the tribo interface interaction, and less so on the subsurface evolution.

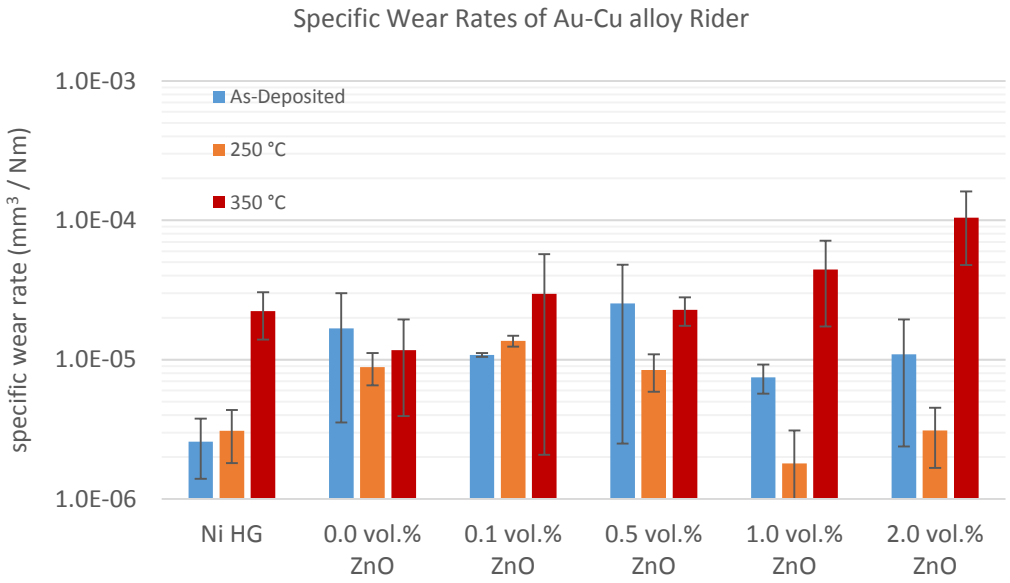

Fig. 5.11: Specific wear rates of Au-Cu alloy rider sliding against commercial Ni HG and Au-(0, 0.1, 0.5, 1.0, 2.0 vol.%)ZnO films for as-deposited condition and annealed conditions of 250°C and 350°C in air for 24 hours.

To evaluate the significant increase in specific wear rate of the 2.0 vol.% ZnO film between the 250°C and 350°C annealed conditions of over two orders of magnitude, SEM micrographs were collected of the unworn surface and wear track regions (Fig. 5.12). Fig. 5.12a is a micrograph of the 250°C annealed unworn surface and is similar to as-deposited surface morphology. The wear track in low magnification and higher magnification of the center of the wear track are shown in Fig. 5.12b&c, respectively. The wear track micrographs revealed dark contrast patches and regions near the edge of the sliding contact patch similar to those revealed and identified to be Zn rich wear debris by Argibay and coworkers for as-deposited 2.0 vol.% ZnO [1]. The higher magnification micrograph in the center of the wear track where contact pressure is the greatest revealed a very smooth and conformal wear surface with

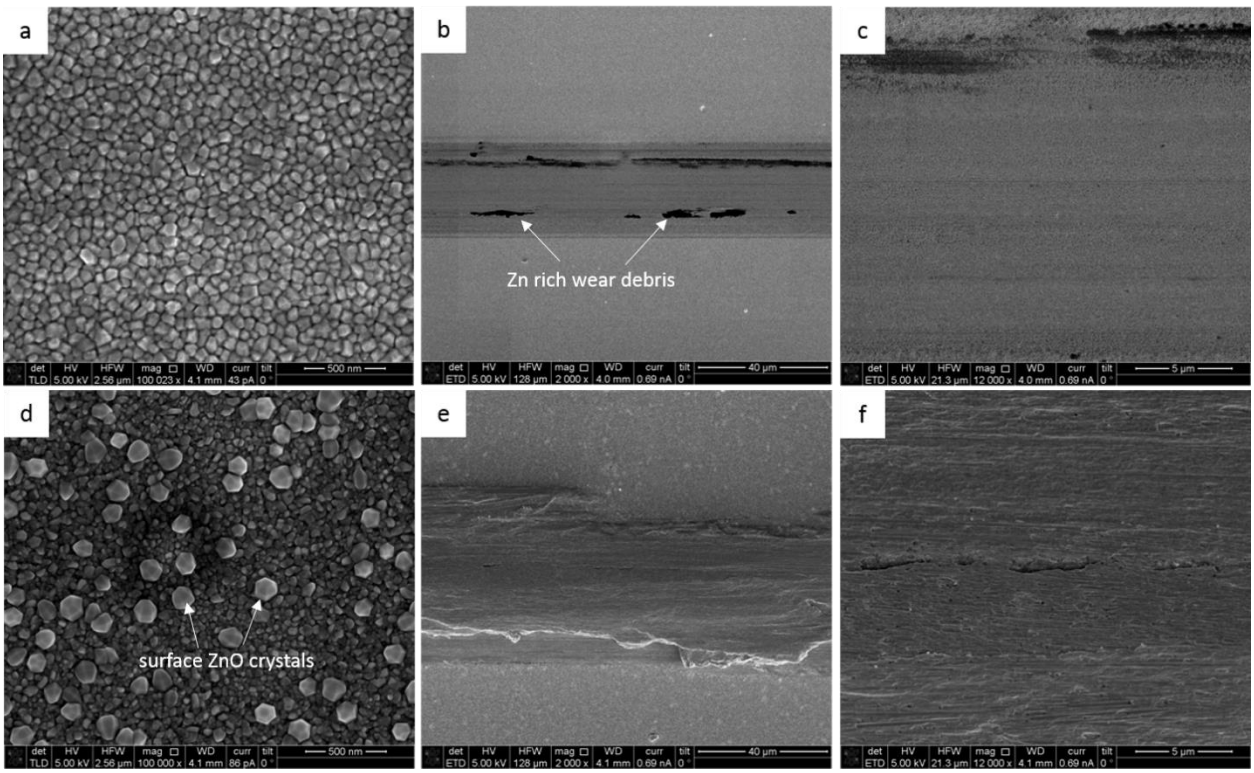

Fig. 5.12: SEM micrographs of Au-2 vol.% ZnO film annealed at the 250°C condition in (a-c), and film annealed at the 350°C condition in (d-f). The unworn surface is shown in (a&d), and the wear track surfaces after 100 cycles of sliding ECR testing shown in (b,c,e&f).

minimal striations in the direction of sliding indicating a fine scale nano-abrasive wear mechanism that is likely the root of the exceptionally low wear rate of this film condition.

Fig. 5.12d is a micrograph of the 2.0 vol.% 350°C annealed unworn film surface and revealed a distinct surface feature annotated in the figure that are hypothesized to be ZnO Wurtzite crystals (many of hexagonal faceted shape of Wurtzite) on the surface of the film with an average diameter of ~120 nm. Micrographs of the wear track in Fig. 5.12e revealed a much higher degree of plastic deformation and plowing of the film to the edges of the wear track in comparison to the 250°C condition film. At higher magnification in Fig. 5.12f, there is evidence of more coarse scale micro-abrasion striations as well as regions of adhesive pullout transfer. The change from fine nano-abrasive wear to combined coarse micro-abrasive and adhesive wear from the 250°C to 350°C condition is hypothesized to be a result of the ZnO in the near surface Au grain boundaries diffusing and forming the faceted nanocrystals seen on the surface in Fig. 5.12d. The loss of ZnO in the near surface Au grain boundaries could act to increase the real area of contact during the first few cycles of sliding wear, corroborated by the more than threefold increase in CoF, and permanently altering the adhesive contact as well adding hard ZnO crystals to add a micro-abrasive wear mechanism. The loss of the reinforcing ZnO is likely confined to the near surface of the film as significant grain growth was not observed by EBSD data on similarly annealed films by Schoppner and coworkers as well due to the aforementioned fact that nanoindentation hardness was unchanged [14].

5.2.3 Sliding-induced Subsurface Deformation of Annealed Au-ZnO Films

To further investigate the change in sliding ECR friction and wear mechanisms of the 250°C and 350°C annealed 2.0 vol.% ZnO films, HAADF-S(TEM) analysis was conducted on film

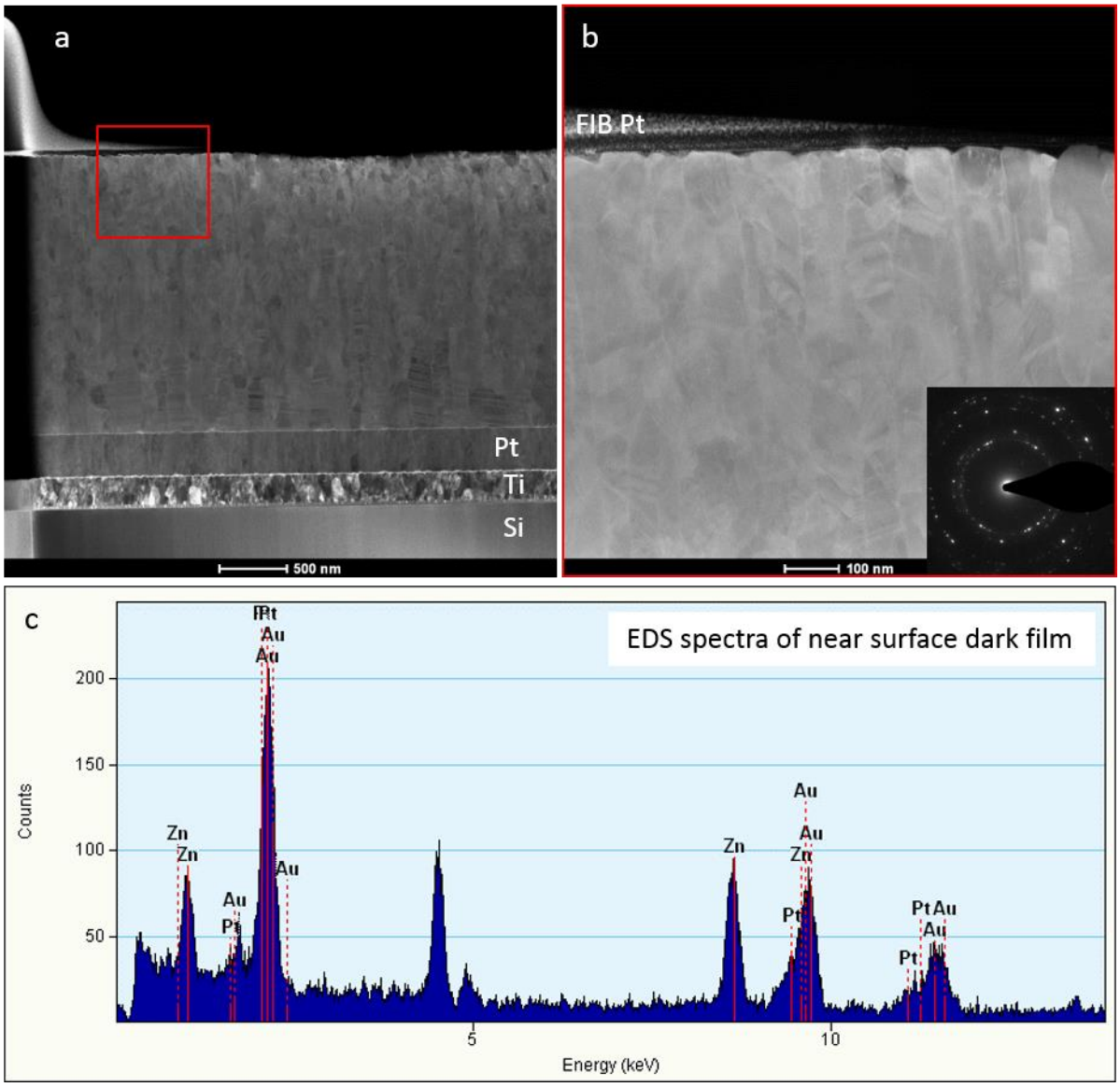

Fig. 5.13: HAADF-STEM micrographs of the 250°C annealed condition Au-2 vol.% ZnO film after 100 cycles of sliding ECR wear (a), and higher magnification, (b), with inset diffraction pattern of the red bordered region in (a). (c) Shows the EDS spectra of the dark film on the surface of the Au grains shown in (b). Direction of sliding was right to left.

cross-sections (Fig. 5.13 and 5.14 respectively) locally FIB milled form the center of the wear track and parallel to the direction of sliding. Fig. 5.13a shows a low magnification HAADF-STEM image of the worn cross-section of the 250°C film which retained nearly the entire initial film thickness of 2 µm after 100 cycles of sliding ECR wear. Film grain structure beneath the wear track also retained nearly identical structure to that of the as-deposited condition shown in Fig.

5.3. At higher magnification in Fig. 5.13b a thin layer several nm thick of darker contrast just below the protective FIB Pt layer is identified and the EDS spectra collected from this region is given in Fig. 513c. Although EDS cannot spatially resolve chemical information on this scale it did reveal that the upper most layer does contain a significant amount Zn, probably as ZnO, which could be acting to reduce adhesive contact and thus friction as was observed in the sliding ECR tests. This ZnO containing film was thicker in other sections of the wear track as evident by another FIB liftout shown in Fig. 5.14. An ~80 nm thick, more continuous ZnO film on the wear surface is shown. The selected area diffraction pattern on this layer indicated a predominately amorphous structure. In addition, there is also near surface Au grain refinement where dislocation cells are orientated parallel to the sliding direction (right to left).

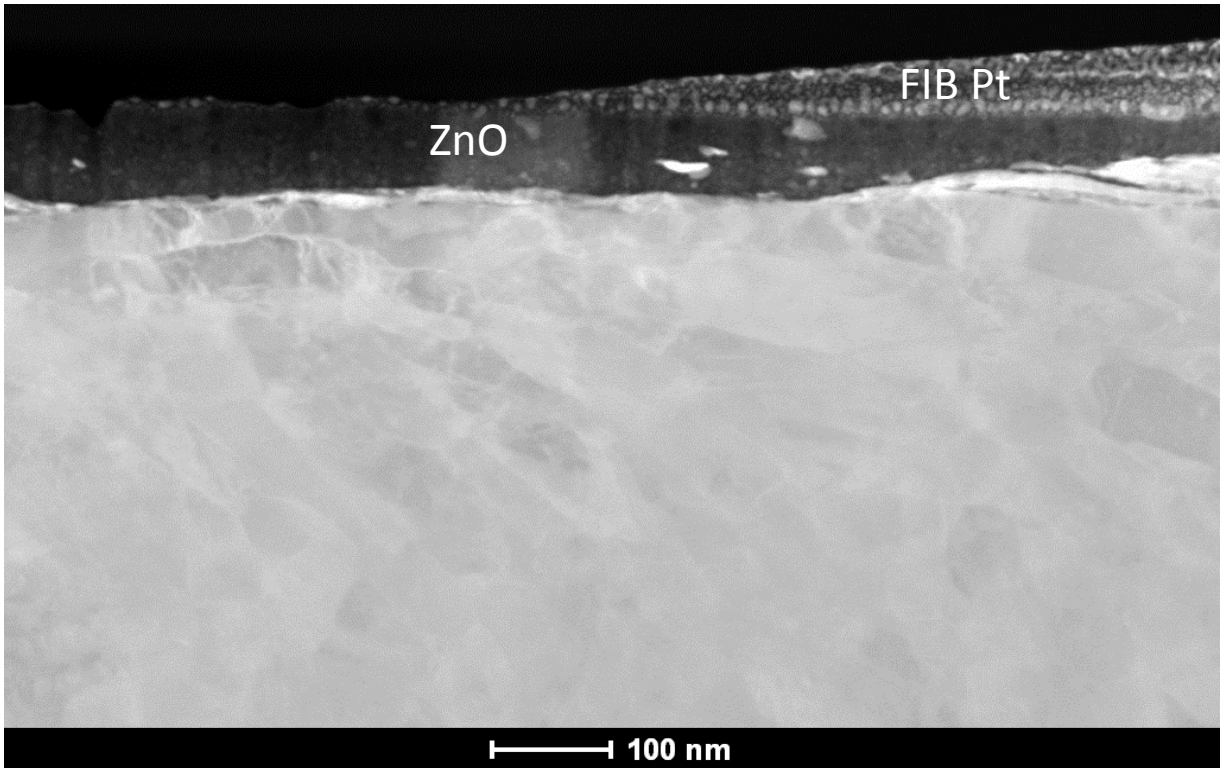

Fig. 5.14: Higher magnification HAADF-STEM micrograph of the 250°C annealed condition Au-2 vol.% ZnO film after 100 cycles of sliding ECR wear. A continuous Zn-containing film, likely ZnO, is present on the wear surface. Direction of sliding was right to left.

Furthermore, this thin ZnO film was not observed across the entire wear surface indicating the wear debris layer was non-continuous, similar to varying thickness of Zn containing wear debris shown in planar SEM image in Fig. 12b.

In contrast to the 250°C condition, the low magnification HAADF micrograph of the 350°C annealed 2.0 vol.% film worn cross-section in Fig. 5.15a showed significant wear with approximately 200-400 nm of the Au-ZnO film remaining. Also captured in this micrograph is a surface embedded particle likely from those observed on the surface of the unworn film in Fig. 5.12d. At higher magnification in Fig. 5.15b the observed Au grain microstructure has lost its columnar growth structure and has no evidence of twins but contains highly deformed and dislocation rich grains elongated in the direction of sliding due to tribological stress. Large scale Au grain refinement is evident compared to the 250°C annealed film. This is evident when

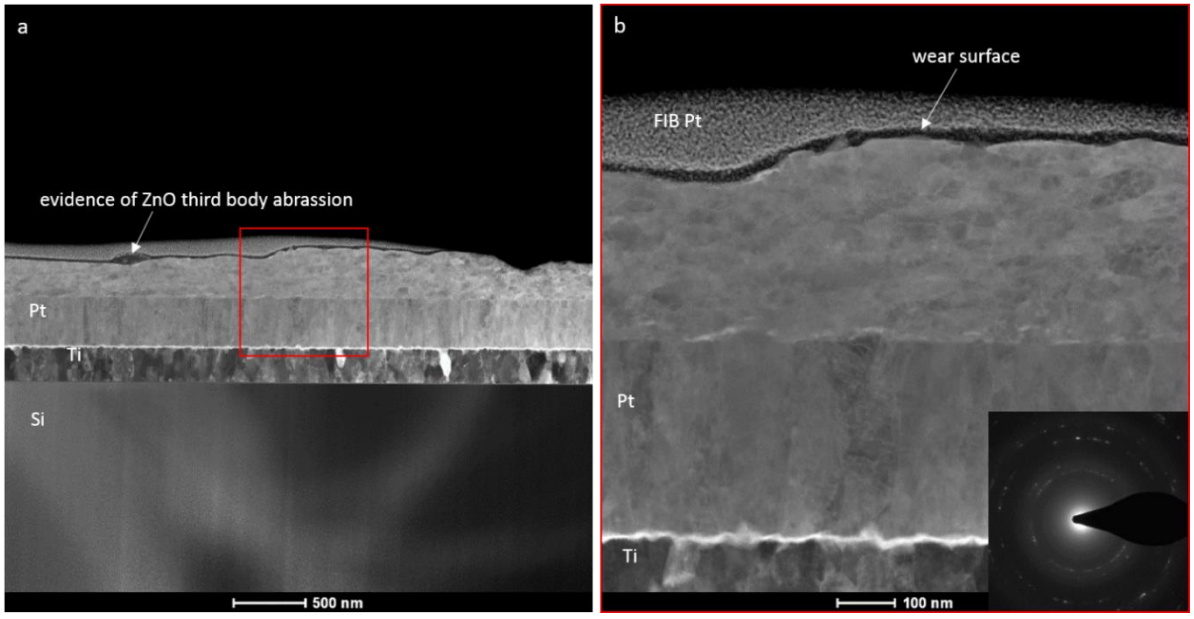

Fig. 5.15: HAADF STEM micrographs of the 350°C annealed condition Au-2 vol.% ZnO after 100 cycles of sliding ECR wear (a), and higher magnification, (b), with of red region in (a). Inset diffraction pattern was taken from the remaining Au-ZnO worn layer. Direction of relative sliding was transverse in the plane of TEM foil.

comparing the diffraction patterns for each film where the 350°C pattern in Fig. 5.15b inset shows more ring-like diffraction spots confirming an increase in grain refinement There is also evidence of the Zn rich tribofilm as observed in the 250°C annealed worn cross-section. The significantly reduced film thickness and highly deformed microstructure of the cross-section agree with the high wear rate and suggest that a significant portion of the film thickness experienced a migration of the strengthening ZnO at the Au grain boundaries due to the elevated annealing temperature. ZnO diffusing up through the grain boundaries with increased mobility at 350°C results in a non-continuous Zn rich layer.

5.3 Electrical Resistivity of Au-ZnO Composites in the Dilute ZnO Regime and Dependence on Grain Size

5.3.1 Empirical Function of Electrical Resistivity Dependent on ZnO Concentration

Electrical resistivity values of as-deposited Au-ZnO in the dilute ZnO regime (< 5.0 vol.%) measured via four point probe are plotted as a function of vol.% in Fig. 5.16 along with the average hardness values reported in table 5.2. Electrical resistivity values plotted here are expected to have errors contained within the size of the plotted symbols. In the dilute oxide regime, the resistivity of the films is found to increase linearly with the concentration of ZnO and a least squares fit of the data is plotted as a dashed line Fig. 5.16. An empirical linear relationship of resistivity as a function of ZnO volume fraction is presented in Eq. 5.4, where ρ_o is the resistivity of the pure e-beam Au, *f* is the volume fraction of ZnO, and *C* is an empirical coefficient of the linear rate of change of resistivity with volume fraction ZnO.

$$\rho(f) = \rho_o + Cf \tag{5.4}$$

The coefficient C is similar to the linear scalar Nordheim coefficient for metal solutions except that in we chose to have the function depend on volume fraction, *f*, instead of atomic fraction and has units of (μΩ-cm/*f*). For the dilute oxide regime of the e-beam Au-ZnO films the empirical coefficient was determined to be $C = 120$ μΩ-cm/*f* (1.20 μΩ-cm/vol.%). This value for the linear scaling coefficient is similar to the value of dilute oxide regime Au-V_2O_5 reported by Bannuru et al [10], yet significantly lower than the Nordheim coefficients of many binary Au metal solid solutions [15]. Although similar results were obtained for the Au-V_2O_5 system in the dilute oxide regime, the authors attributed the increase in electrical resistivity with increased electron scattering of nm sized well dispersed oxide particles. As was shown for the 2.0 vol.% ZnO film in Fig. 5.4a, there is a significant amount of nm sized ZnO intragranular particles that were estimated to have a mean spacing of ~10 nm to account for Orowan strengthening contributions. However the electrical resistivity is also highly dependent on the density of

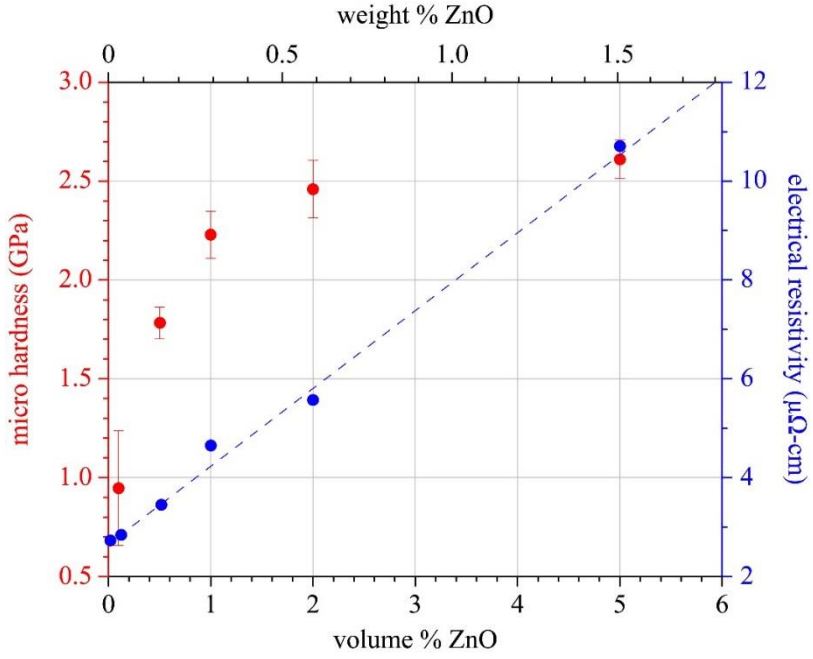

Fig. 5.16: Average hardness and electrical resistivity as a function of ZnO vol.% concentration for 2 μm thick films.

planar electron scattering sites such as grain boundaries and a change in grain size is observed from the pure e-beam Au (Fig. 5.1a) to the dilute addition of only 2.0 vol.% ZnO (Table 5.1) of two orders of magnitude.

5.3.2 Adapting the Mayadas-Shatzkes Electron Scattering Model to Predict Grain Size of Au-ZnO Composites

To extend the analysis of the resistivity of the dilute oxide Au-ZnO thin films and correlate it with the average grain size a combination of the empirical relationship, Eq, 5.4 and the Mayadas-Shatzkes (M-S) electron scattering model, which describes change in electrical resistivity with grain boundary scatting, is presented. The closed form solution expressing the change in resistivity of a single crystal material and a polycrystalline material originally derived by M-S is given in Eq. 5.5 [16]. The change in resistivity in the M-S model is given as a function of the dimensionless parameter, α given in Eq. 5.6, which is itself a function of several material dependent values. The material dependent values in Eq. 5.6 are the bulk electron inelastic mean free path, λ, average distance between planar defects, d, and an empirically derived reflection coefficient, R, which describes the fraction of electrons that are internally reflected when encountering a boundary rather than transmitting through the planar defect and has a value between 0 and 1.

$$\rho = \rho_o \left[1 - \frac{3}{2}\alpha + 3\alpha^2 - 3\alpha^3 \ln\left(1 + \alpha^{-1}\right) \right]^{-1} \tag{5.5}$$

$$\alpha = \frac{\lambda}{d}\frac{R}{1-R} \tag{5.6}$$

In the case of the Au-ZnO films, the four point probe resistivity measurements yield a measurement of electrical conduction that is transverse in the plane of the film such that the

planar defect spacing encountered is that of the grain diameters measured in the plane and reported in table 5.1 for various methods. For this case, we can treat the planar defect spacing, *d*, as the average grain diameter of the Au-ZnO films. In the original publication of the M-S model two simplified approximations of Eq. 5.5 were given for when the dimensionless parameter $\alpha \ll 1$ and for when $\alpha \gg 1$. However for the dilute oxide Au-ZnO films resulting in nm sized grain sizes and using the literature obtained values of mean free path, $\lambda = 44$ nm [17], and boundary scattering coefficient, $R \cong 0.5$, a value of $\alpha \cong 1$ is obtained. The relative error between the closed form solution in Eq. 5.5 and the original approximations for $\alpha \ll 1$ and for when $\alpha \gg 1$ are 4% or greater for values of $\alpha \cong 1$. For this reason a new approximation to the closed form M-S model solution for the ratio of resistivity, Eq. 5.7, was proposed that is shown in [18] to have at most 2% relative error.

$$\frac{\rho}{\rho_o} \cong 1 + \frac{4}{3}\alpha \tag{5.7}$$

With this approximation in Eq. 5.7 and the empirical linear relationship in Eq. 5.4 describing the change in resistivity as a function of volume fraction, *f*, of ZnO and the assumption that ,*d*, is representative of the transverse average grain diameter (excluding twin boundaries) it is possible to derive an expression for average grain size as a function of the concentration of ZnO, Eq. 5.8.

$$d \cong \frac{4\rho_o}{3Cf}\left(\frac{\lambda R}{1-R}\right) \tag{5.8}$$

Fig. 5.17 shows a plot of the average grain sizes determined from the various microscopy methods in Table 1 for dilute oxide Au-ZnO films and the average grain size values predicted by Eq. 5.8. It can be seen that the predicted average grains sizes are in agreement

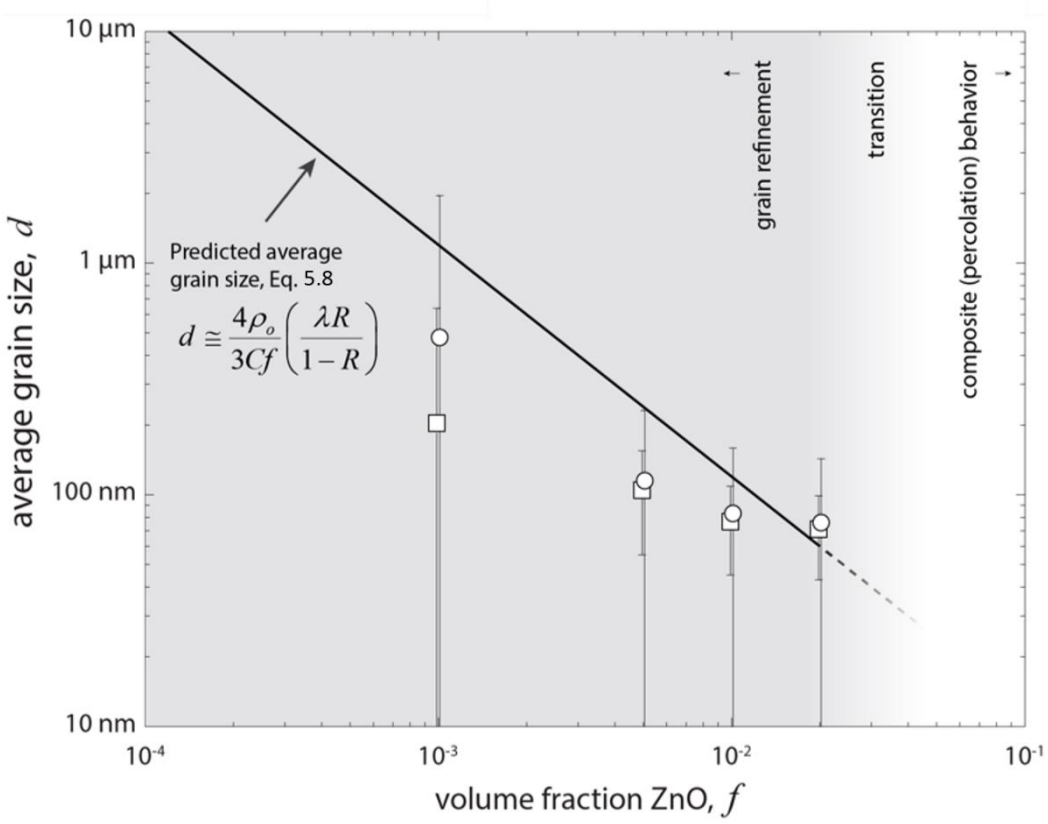

Fig. 5.17: Average grain arithmetic diameter (squares) and area-weighted average grain diameter (circles), from Table 5.1, plotted versus ZnO volume fraction. Solid line is a plot of the predicted effective grain size calculated using Eq. 5.8. Shaded region highlights the ZnO volume fraction range where Eq. 5.8 is valid.

with those reported in Table 1 considering the large standard deviations of the measured grain sizes and the relatively small number of counted grains due to their nm size scale and the assumption that any analysis on relatively small two dimensional sections are representative of a three dimensional structure. The shaded region in Fig. 5.17 equates to the range in which the Au-ZnO films exhibit the linear relationship of resistivity with ZnO concentration and where grain size is rapidly reduced and inversely proportional to the volume fraction of ZnO (from 0 – 2.0 vol.% ZnO). Beyond this point there is a transition region where grain refinement reaches its asymptotic limit and the ZnO acting at the Au grain boundaries becomes saturated and coalesces into larger grains. Here it is worth mentioning that twin boundaries were excluded

from the horizontal line measurements of grain diameters reported in Table 1 as the boundaries were recently found to be negligible to electron scattering contribution [6], and thus would not contribute to the measured resistivity values and cannot be represented in the current model. This new expression is however still a powerful method by which average grain size, and indirectly other properties such as hardness, can be determined via simple four point probe resistivity measurements of thin metallic films and without the need for extensive microscopy analysis that typically are small sections of the bulk structure.

5.4 Investigations of the Grain Size Thermal Stability of Au-ZnO Composite Thin Films

5.4.1 Evaluation of Structure Evolution in Au-ZnO Films for Low Temperature Annealing

To observe the change in grain structure of the 2.0 vol.% ZnO film due to annealing in air, TEM foils were prepared from FIB cross-sections of the films annealed 24 hours at 250°C and 350°C. The HAADF micrographs of these cross-sections are shown in Fig. 5.18 a and b for the 250°C and 350°C condition, respectively, and can be compared to the as-deposited micrographs presented in Fig. 5.3. In both Fig. 5.18a and b we observe abnormal grain growth in the film cross-section with the largest grains located near the Au-Pt interface. In both the inset image of the 250°C annealed film and the 350°C annealed film in Fig. 5.18b we observe the thin ZnO layer that is likely formed from diffusing ZnO located in the Au grain boundaries near the interface. The depletion of the ZnO near the Au-Pt interface and the subsequent loss of boundary pinning is the hypothesized mechanism of the grain growth in both annealing conditions. Also, there is no Pt diffusion into the Au grains. For the 250°C annealed film condition, the larger grain formation was accompanied by twin boundary formation roughly

parallel to the Au-Pt interface (Fig. 5.18a inset), while the 350°C film lacked the annealing twin boundary formation it extended further into the Au-ZnO layer. This observed subsurface abnormal grain growth highlights the inherent difficulty in determining grain growth of thin films from typical surface EBSD maps and or 2D planar and cross-sectional imaging methods that capture a small section of the overall structure. With the observation of highly non-homogeneous grain growth, and evidence that much of the growth occurs subsurface, a new method to indirectly measure average grain growth of the entire film was developed and presented in the next section.

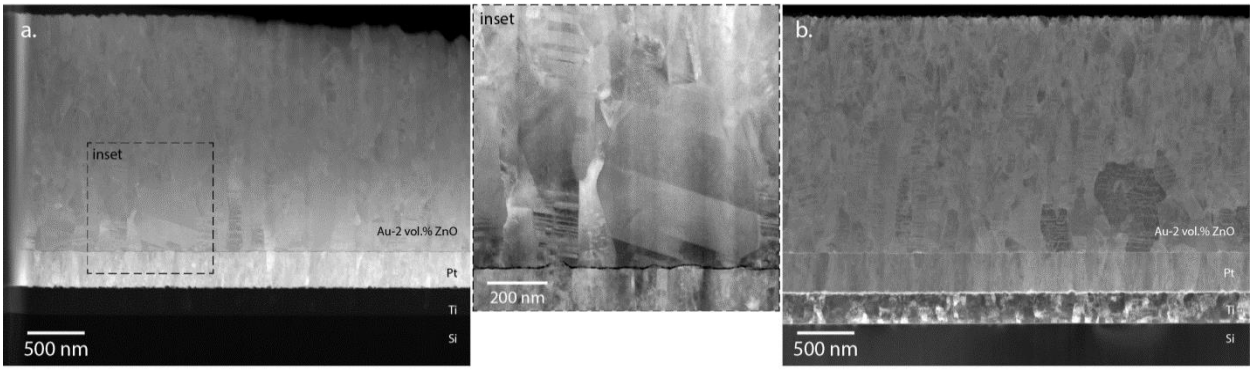

Fig. 5.18: Representative HAADF TEM micrographs (a) and (b) and inset bright field micrograph of film cross-sections of Au-2.0 vol.% ZnO film post (a) 250°C annealing and (b) 350°C annealing for 24 hours in air.

5.4.2 In situ Electrical Resistivity Annealing Experiments and Data Interpretation

With the relation between grain size and electrical resistivity of the Au-ZnO films developed using the M-S model and an empirical function dependent on volume fraction ZnO presented in Eq. 5.8, it is now possible to acquire an average grain diameter value from a simple 4 wire probe measurement (excluding twin boundaries). To utilize this relation and investigate the grain growth behavior of the Au-ZnO films, a custom built 4 probe resistivity platform, described in section 3.5.2, was fabricated to acquire data at elevated temperatures. Samples of

1.0 and 2.0 vol% ZnO films were deposited onto polished alumina substrates without adhesion layers to prevent possible solid solution and parallel metallic layer contributions to the measured resistivity values. These samples were then annealed in a continuous stepped annealing profile starting at room temperature and ramping at a rate of 2°C/min to 8 hour dwells at nominally 100, 200, 300, 400, and 500°C followed by passive cooling back to room temperature. Temperature was recorded by placing a k-type thermal couple in contact with the center of the film. The results of the in-situ resistivity annealing profiles of 1.0 and 2.0 vol.% ZnO films are shown in Fig. 5.19 with the temporal progression of both experiments annotated on the 2.0 vol.% ZnO profile.

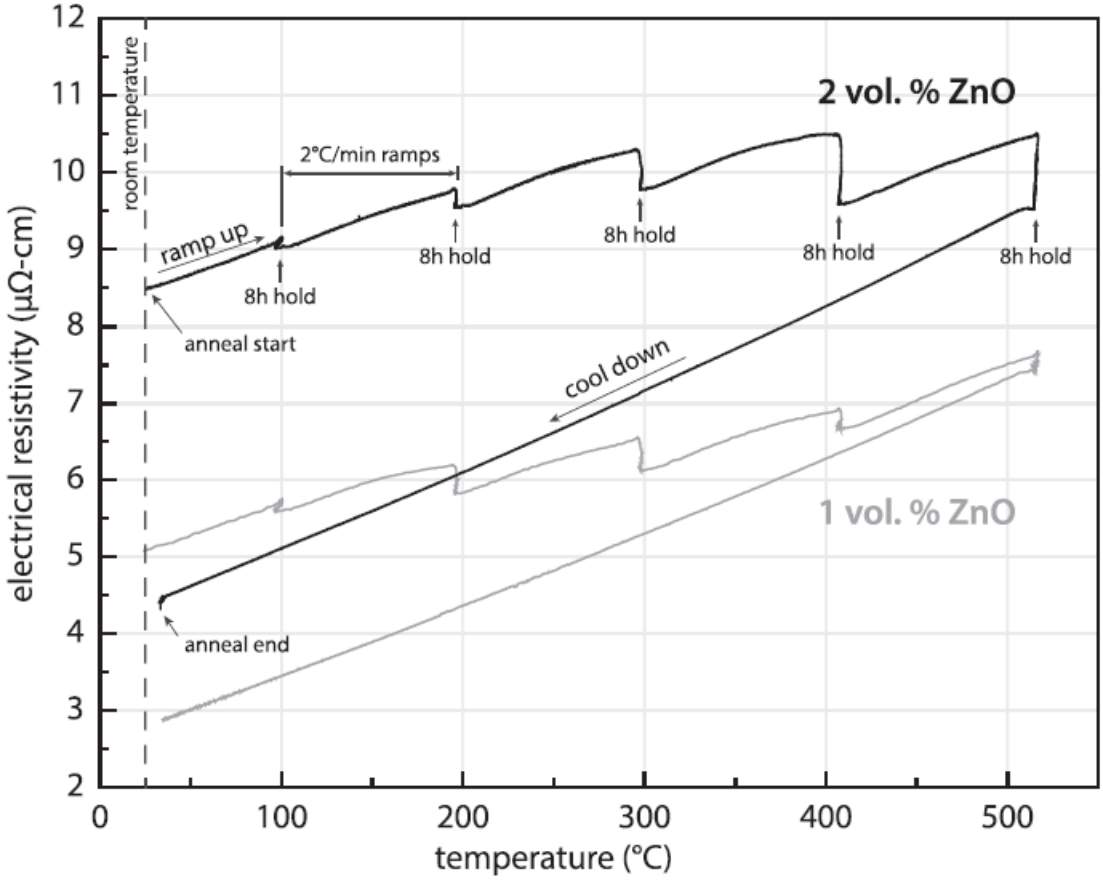

Fig. 5.19: Electrical resistivity data versus temperature from in-situ annealing profile of 1.0 and 2.0 vol.% ZnO films. The 2.0 vol.% ZnO data is annotated with the thermal ramp rate and temporal progression of the experiments.

To extract grain growth information from the in-situ resistivity annealing data presented in Fig. 5.19, data was processed in the following methods. Initially the resistivity data was corrected to remove thermal phonon contributions to the measured values so that changes in resistivity could be correlated to the grain growth. A piece wise linear interpolation to determine the resistivity temperature coefficient (RTC) of the films was applied to the cool down data of the 1.0 vol.% ZnO film shown in Fig. 5.19. The 1.0 vol.% ZnO film was used as it was expected to have reached a stable and coarse grain size after the annealing profile and evidenced by the linear cool down profile. The 2.0 vol.% ZnO film exhibited some continuing grain growth after the 500°C 8 hour dwell and during the cool down profile for temperatures above ~400°C as evidenced by curvature in the cool down profile in Fig. 5.19 at these temperatures. The RTC measured from the 1.0 vol.% ZnO film was assumed to be independent of composition and the linear increase in resistivity due to thermal contributions was subtracted from the recorded values in Fig. 5.19 according to Matthiessen's rule of additive contributions to metallic resistivity.

Next mean grain size values were calculated from the temperature corrected resistivity values using Eq. 5.8. Fig. 5.20 presents the grain growth data for each of the 8 hour temperature dwells for both the 1.0 and 2.0 vol.% ZnO films. Also plotted in Fig. 5.20 as red traces are the fitted values of grain size determined using the grain growth model proposed by Michels et al. [19], given in Eq. 5.9, that describes the grain growth kinetics of metal systems stabilized by solute drag at boundaries with the drag force also being dependent on temperature. This model was not applied to the 100°C anneal profile as no appreciable grain growth was observed for either film.

$$\bar{d}(t)=\left[\bar{d}_{\max}^{2}-\left(\bar{d}_{\max}^{2}-\bar{d}_{o}^{2}\right)\exp\left(\frac{-8A}{\bar{d}_{\max}^{2}}\left(t-t_{o}\right)\right)\right]^{1/2} \tag{5.9}$$

In the Michels et al. model [19] given in Eq. 5.9, $\bar{d}_{\max}$ is a fitting parameter corresponding to the asymptotic and stable mean grain size for a given temperature, $\bar{d}_{o}$ is a fixed parameter corresponding to the as-deposited mean grain size, $\left(t-t_{o}\right)$ is elapsed time at a given temperature, and *A* is fitting parameter describing the combined grain boundary mobility and grain boundary energy with the units of (length^2/time). The as-deposited grain size, $\bar{d}_{o}$, calculated from room temperature resistivity values of the films used in the in-situ resistivity annealing experiments using Eq. 5.8 and used throughout the analysis. For nearly all of the grain growth profiles in Fig. 5.20 the recorded data enters the tail or closely approaches the asymptotic grain size predicted by the Michels et al. model [19], with the notable exception being the 2.0 vol.% ZnO film at the 500°C, which is further confirmation that the curvature of the cool down profile for that film did indeed include the assumed continued grain growth and that the RTC value of the Au-ZnO films was best calculated using the 1.0 vol.% film.

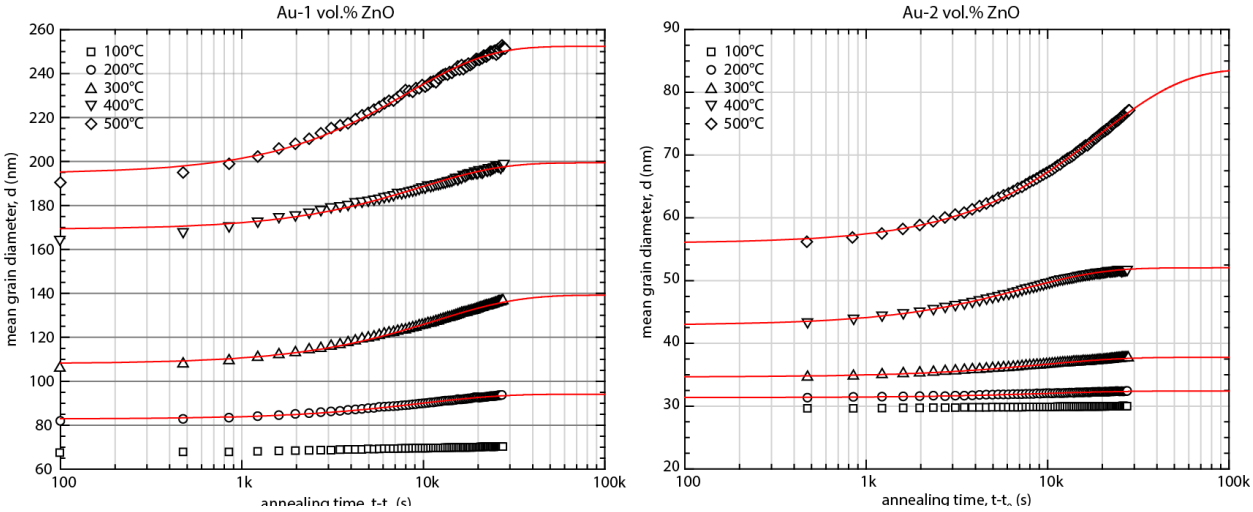

Fig. 5.20: Grain size evolution of 1.0 and 2.0 vol.% ZnO films determined by Eq. 5.8 during each 8 hour hold period of the in-situ resistivity anneal profile. Curve fitting of the Michels et al. grain growth model for each 8 hour hold are shown in red.

As the mobility parameter, *A*, in the Michels et al. model [19] is representative of the grain boundary energy and mobility it was expected to exhibit an Arrhenious behavior with temperature. Fig. 5.21 shows the mobility parameter calculated using the Michels et al. grain growth model [19] fitted to each temperature dwell that exhibited grain growth in Fig. 5.20, and a linear least squares fit to the data. From the least squares fit in Fig. 5.21 and the general expression for Arrhenious behavior given in Eq. 5.10, the parameter E_a, the activation energy for grain boundary mobility, and the parameter A_o, a pre-exponential factor representing the theoretical maximum thermally activated mobility, could be calculated. The results of the Arrhenious least squares fit in Fig. 5.21 and the fitting parameters of the Michels et al. model presented in Fig. 5.20 are consolidated in Table 5.3.

$$A = A_o \exp\left(-\frac{E_a}{kT}\right) \tag{5.10}$$

The application of the Michels et al. model [19] and resultant fits to the 8 hour dwell grain size data calculated by Eq. 5.8 and presented in Fig. 5.20 yeild satisfacrory fits, however it is unclear whether the observed asymptotic behavior in grain growth is indicative of intrinsic thermodynamic stability of grain size, or if the growth was sufficiently kinetically limited to appear stable and asymptotic over the 8 hour annealing times analyzed. The Arrhenious behavior observed for the grain boundary mobility parameter could be representative of the limiting kinetic mechanism of the observed growth, and not intrinsic grain size stability. Although the activation energy of the 1.0 vol.% ZnO film is greater than that of the 2.0 vol.%

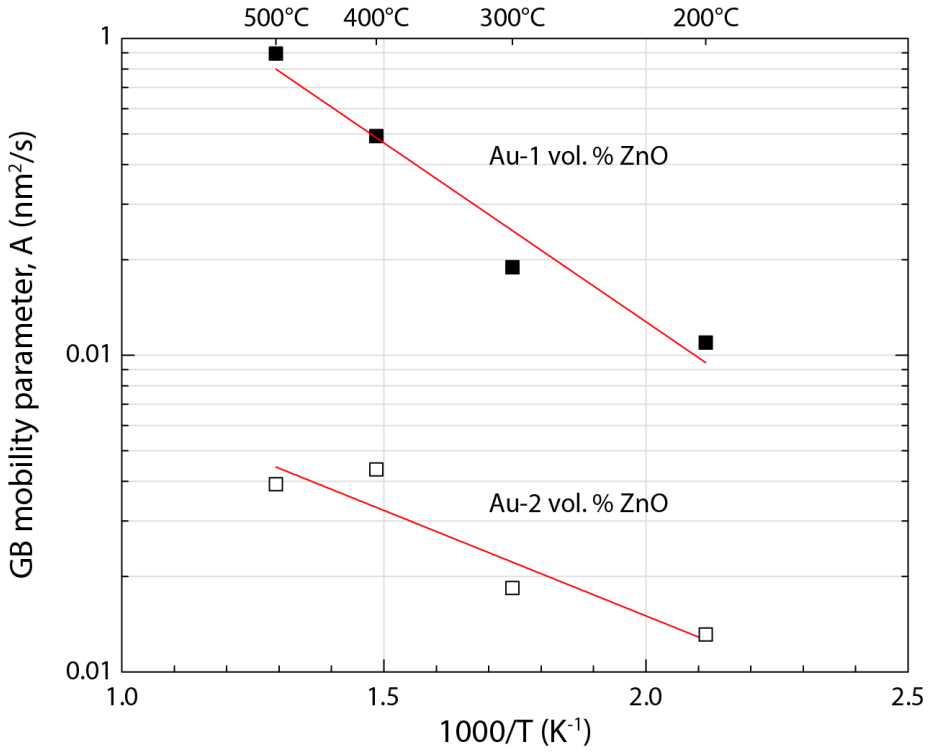

Fig. 5.21: Plot of grain growth Arrhenious behavior in the grain boundary mobility parameter for 8 hour holds during in-situ resistivity annealing profiles for 1.0 and 2.0 vol.% ZnO films determined using the Michels et al. model applied to grain size determined from Eq. 5.8.

film by nearly a factor of 2 and is expected if it is interpreted as a decrease in the activation barrier due to a higher density of grain boundaries (e.g. smaller grain size) for the 2.0 vol.% film, the theoretical maximum mobility, A_o, is more difficult to interpret. Values of the calculated maximum mobility for both films are similar to that of grain boundary diffusivity values for various metals used to strengthen Au [20-22], however the value for the 2.0 vol.% film is an order of magnitude less than that of the 1.0 vol.% film suggesting that if it may be self reducing based on the saturation of ZnO at the grain boundaries. There is previously reported evidence to support the hypothesis that the Au grain growth is dominated by the diffusion and depletion of grain boundary ZnO near the Au/Pt as shown in Fig. 5.18 for 2.0 vol.% ZnO films annealed at 250 and 350°C and at the surface grains as shown for the ZnO crystal formation on the surface

of film in Fig. 5.12d. This depletion of grain boundary ZnO, which appears to increase in rate at higher temperatures, removes the source of Zener drag and no longer inhibits Au grain growth and is likely what is being parameterized by the mobility parameter, *A*, in Eq. 5.9.

Table 5.3: Resultant fitting parameters of the Michels et al. grain growth model applied to the grain size data, calculated using Eq. 5.8, acquired during the 8 hour holds during in-situ resistivity annealing profiles and the activation energy, E_a, and pre-exponential factor, A_o, determined from the least squares fit in Fig. 5.21.

vol.% ZnO	T (°C)	1000/T (K^{-1})	*A* (nm^2/s)	E_a (kJ/mol)	A_o (m^2/s)
1.0	500	1.29	0.90	21.6	2.3×10^{-17}
	400	1.49	0.49		
	300	1.74	0.19		
	200	2.11	0.11		
2.0	500	1.29	0.04	12.7	3.1×10^{-18}
	400	1.49	0.04		
	300	1.74	0.02		
	200	2.11	0.01		

5.6 Chapter 5 References

1. Argibay, N., et al., *Wear resistant electrically conductive Au–ZnO nanocomposite coatings synthesized by e-beam evaporation.* Wear, 2013. **302**(1-2): p. 955-962.
2. Argibay, N., et al., *Electrical resistivity of Au-ZnO nanocomposite films.* Journal of Applied Physics, 2013. **113**(14): p. 143712.
3. Grovenor, C., H. Hentzell, and D. Smith, *The development of grain structure during growth of metallic films.* Acta Metallurgica, 1984. **32**(5): p. 773-781.
4. Kotula, P.G., M.R. Keenan, and J.R. Michael, *Automated analysis of SEM X-ray spectral images: A powerful new microanalysis tool.* Microscopy and Microanalysis, 2003. **9**(01): p. 1-17.
5. Page, T., et al. *Nanoindentation Characterisation of Coated Systems: P: S 2-A New Approach Using the Continuous Stiffness Technique*. in *MRS Proceedings*. 1998. Cambridge Univ Press.
6. Saha, R. and W.D. Nix, *Effects of the substrate on the determination of thin film mechanical properties by nanoindentation.* Acta Materialia, 2002. **50**(1): p. 23-38.
7. Cao, Y., et al., *Nanoindentation measurements of the mechanical properties of polycrystalline Au and Ag thin films on silicon substrates: Effects of grain size and film thickness.* Materials Science and Engineering: A, 2006. **427**(1): p. 232-240.

8. Emery, R.D. and G.L. Povirk, *Tensile behavior of free-standing gold films. Part I. Coarse-grained films.* Acta Materialia, 2003. **51**(7): p. 2067-2078.
9. Chew, Y.H., et al., *Strain rate sensitivity and Hall–Petch behavior of ultrafine-grained gold wires.* Thin Solid Films, 2008. **516**(16): p. 5376-5380.
10. Bannuru, T., et al., *The electrical and mechanical properties of Au–V and Au–V[sub 2]O[sub 5] thin films for wear-resistant RF MEMS switches.* Journal of Applied Physics, 2008. **103**(8): p. 083522.
11. Frost, H.J. and M.F. Ashby, *Deformation mechanism maps: the plasticity and creep of metals and ceramics.* 1982.
12. Kocks, U., *The relation between polycrystal deformation and single-crystal deformation.* Metallurgical and Materials Transactions, 1970. **1**(5): p. 1121-1143.
13. Follstaedt, D.M., J.A. Knapp, and S.M. Myers, *Strengthening by high densities of nanometer-size precipitates: Oxides in Ni.* Metallurgical and Materials Transactions A, 2003. **34**(4): p. 935-949.
14. Schoeppner, R., et al., *Mechanical and electrical performance of thermally stable Au–ZnO films.* Acta Materialia, 2015. **91**: p. 1-9.
15. Kasap, S.O., *Principles of electronic materials and devices*. 2006: McGraw-Hill.
16. Mayadas, A.F. and M. Shatzkes, *Electrical-Resistivity Model for Polycrystalline Films: the Case of Arbitrary Reflection at External Surfaces.* Physical Review B, 1970. **1**(4): p. 1382-1389.
17. Matula, R.A., *Electrical resistivity of copper, gold, palladium, and silver.* Journal of Physical and Chemical Reference Data, 1979. **8**(4): p. 1147-1298.
18. Argibay, N., et al., *On the thermal stability of physical vapor deposited oxide-hardened nanocrystalline gold thin films.* Journal of Applied Physics, 2015. **117**(14): p. 145302.
19. Michels, A., et al., *Modelling the influence of grain-size-dependent solute drag on the kinetics of grain growth in nanocrystalline materials.* Acta materialia, 1999. **47**(7): p. 2143-2152.
20. Holloway, P.H., *Analysis of grain-boundary diffusion in thin films: Chromium in gold.* Journal of Applied Physics, 1976. **47**(9): p. 3769.
21. Tompkins, H.G., *Diffusion of Cobalt out of Cobalt-Hardened Gold Measured with Auger Electron Spectroscopy.* Journal of the Electrochemical Society, 1975. **122**(7): p. 983-987.
22. Tompkins, H.G. and M.R. Pinnel, *Relative rates of nickel diffusion and copper diffusion through gold.* Journal of Applied Physics, 1977. **48**(7): p. 3144.

CHAPTER 6

CONCLUSIONS AND REMARKS ON FUTURE RESEARCH

The main focus of this dissertation was to synthesize nanocrystalline Au and make the grain structures stable during thermal exposure and under sliding electrical contacts. Two techniques were adapted to achieve this: ZnO addition that preferentially resided on grain boundaries and He ion implantation. Specifically, e-beam deposition of Au thin films implanted with noble gas ions, He and Ar, as well as codeposited Au-ZnO nanocomposites in the dilute oxide regime were studied for use as sliding electrical contact films. The selection of ion beam modification of Au films by noble gas ion implantation and codeposition with ZnO is based on two main assumptions: that both of these processing methods would result in a net increase in Au film hardness in comparison to as-deposited e-beam Au films to reduce real contact area in tribological sliding, and thus friction and wear; and that noble gasses and ZnO would have no chemical potential with ambient air to act as a driving force for diffusion and segregation at ambient and low temperature aging conditions. Based on this premise it has been shown that He ion implantation and codeposition with ZnO can improve Au film hardness and tribological performance under specific processing conditions, including Ar ion implantation, and can significantly improve friction and wear response with minimal deleterious effect on the sliding ECR. In the case of Au-ZnO nanocomposite films, novel in-situ annealing experiments coupled with electrical resistivity and grain growth models and transmission electron microscopy (TEM) methods showed that these films retain their initial structure in low temperature aging conditions and continue to provide suitable friction, wear, and ECR properties.

A holistic approach of experimental methods was applied in this study as research on

sliding electrical contact materials, and tribology in general, involves interdependencies of several scientific disciplines. These methods included simultaneous sliding friction and ECR measurements, topographical analysis of wear phenomena with scanning white light interferometry (SWLI), and thin film nanoindentation techniques to characterize the tribological, interfacial electron transport, and mechanical properties. Structural characterization of the films was conducted using state-of-the-art methods including X-ray diffraction (XRD); scanning electron microscopy (SEM) imaging, electron backscatter diffraction (EBSD), and transmission Kikuchi diffraction (TKD) coupled with focused ion beam (FIB) preparation; as well as high resolution scanning (STEM) of film cross-sections. For a more complete view of the structural response and effects on tribological behavior, HRTEM was conducted on as-deposited and worn film cross-sections prepared by site specific FIB milling. Electrical resistivity and correlations to structure were determined by four point probe measurements, and unique in-situ resistivity annealing experiments applied to Au-ZnO films to elucidate grain size thermal stability. The following sections present the major conclusions drawn from these investigations.

6.1 Noble Ion Implanted e-beam Deposited Au Films

- Single energy implantation of He ions to the greatest fluence investigated in this study, $\phi = 1x10^{16}$ cm^{-2}, did not alter the e-beam deposited Au grain surface normal texture of (111) and the lowest and highest energies of 22.5 keV and 1200 keV, respectively, did not affect the columnar grain growth structure or grain size as revealed by TEM micrographs.

- Atomic mass contrast imaging via high angle annular diffraction (HAADF) STEM of select He ion implanted film cross-sections revealed He induced cavities with depth distributions in good agreement with SRIM modelling. He induced cavities in the near surface, top 10 nm, were approximately 2-5 nm in diameter while cavities at greater depths were approximately 1 nm in diameter. For the 1200 keV He implanted film there was an observed high density of cavities concentrated at the Au/Pt interface.
- Single and multiple energy implantation of He ions at all fluences investigated had negligible effects on the Au film resistivity, likely because the grain structure was shown to be largely unaffected and because point defect generation of light ion implantation is expected to be minimal.
- Single energy He ion implantation to a fluence of $\phi = 1x10^{16}$ cm^{-2} and at an energy of E = 650 keV, resulting in a He range near half the thickness of the Au layer, reduced the e-beam residual tensile stress by more than 50%.
- Nanoindentation hardness results of single energy He ion distributions were incapable of determining mechanical property changes of the Au films. However, coupled with SRIM modeling, nanoindentation of uniform concentration He profile films showed significant hardness increases, from ~0.8 GPa for as-deposited Au to ~2.5 GPa for 5 at% He. This strengthening was shown to increase proportional to the $(\text{He concentration})^{1/3}$ and is likely due to an Orowan strengthening mechanism of He induced cavities as seen in other FCC metals.
- Specific He ion implantation conditions were able to significantly reduce the sliding friction against Au-Cu alloy counterfaces with little change in ECR. A change of wear

mechanisms from gross adhesion for pure e-beam Au to nano and micro abrasion were observed for the He implantation conditions yielding improved tribological response. Furthermore SWLI analysis of transfer volumes identified a bifurcation in the He implanted sample data sets tribological behavior between either gross adhesion or surface abrasion.

- Cross-sectional TEM revealed that single energy He implantation can significantly reduce the degree of subsurface plasticity due to tribological stress, while HAADF STEM revealed a growth in mean He cavity size and their redistribution, that at the very near surface could be acting to stabilize a nanocrystalline tribo-induced zone that is beneficial to friction and wear behavior.
- Initial investigations of greater atomic mass Ar ion implantation into the near surface of Au films on sliding friction, wear, and ECR yielded similar improved results as specific He implantation conditions.
- Investigations of Au ion implantation into Au films revealed implantation induced point defect and dislocation networks alone were not sufficient to improve sliding ECR tribological behavior, and that noble gas ion induced cavities were of critical importance.

6.2 Au-ZnO Nanocomposites Synthesized by e-beam Deposition

- Codeposition of dilute concentrations of ZnO (< 5.0 vol%) with Au via e-beam evaporation was shown through EBSD, TKD, and cross-sectional imaging to significantly reduce the Au grain size in the composite film to the nanometer scale.

- HRTEM HAADF imaging in conjunction with spatial x-ray spectral analysis revealed that grain size reduction approaches an asymptotic value for ZnO volume concentrations somewhere in the range of 2.0 – 10 vol.% as a result of the grain boundary segregated ZnO, which is responsible for pinning Au grain boundaries during film growth, coalescing to form larger grains instead of being uniformly distributed. E-beam synthesis was also shown to result in nm sized intragranular ZnO particles throughout the Au matrix.
- The composite Au-ZnO films showed significant nanoindentation hardness increases in comparison to pure e-beam Au (from ~0.8 GPa to 2.61 GPa for Au-(5.0 vol.%)ZnO) that was asymptotic with increasing ZnO concentration. The increase in mechanical strength was shown to be a result of Hall-Petch strengthening via the grain size reduction, as well as a significant contribution from Orowan strengthening as a result of the homogenously distributed intragranular ZnO particles.
- As-deposited Au-ZnO films showed increased performance in friction and wear with increasing ZnO concentration, with minimal chatter and variability in ECR in comparison to commercial Ni hardened Au.
- Au-ZnO films of 1.0 and 2.0 vol.% ZnO annealed to 250°C in air yielded similar friction, ECR, and wear performance as similarly annealed commercial Ni hardened Au that was aided by non-continuous thin amorphous ZnO surface layer. However at annealing conditions of 350°C the wear mechanisms were shown to change to more sever abrasion as ZnO diffused to the surface to form Wurtzite crystals acting as third body abrasion particles. ZnO was also observed via cross-sectional HAADF STEM to diffuse to the Pt/Ti interface. This migration of ZnO resulted in a loss of strengthening

mechanisms of the composite resulting in increased plastic deformation throughout the film due to tribological stresses.

- By adapting the Mayadas-Shatzkes electron scattering model of planar defects with an empirically determined linear function of resistivity with ZnO concentration a function capable of predicting grain size from ZnO volume fraction was derived.
- Using the derived function correlating mean grain size to resistivity in conjunction with novel in-situ resistivity annealing experiments grain growth evolution information was able to be determined. This method could prove valuable for evaluating the mean grain size and growth due to annealing in conductive thin films, especially when grain growth is abnormal as was observed in the Au-ZnO system by cross-sectional microscopy.

6.3 Remarks on Future Research

Based on the body of work presented within this dissertation, the following areas of research are suggested for future and continuing research on these stable nanocrystalline Au film systems.

- High cycle simultaneous sliding ECR friction and wear studies at low loads suitable to real applications to determine the cycle to failure and expected performance of the noble ion implanted and Au-ZnO nanocomposite films.
- Low temperature thermal annealing with pressure monitored desorption experiments of He and Ar ion implanted Au films in conjunction with cross-sectional HRTEM should be conducted to evaluate the retained concentration of noble gasses in Au as well as the evolution of implantation induced cavity structure and distribution.

- Auger or XPS depth profiling of Au-ZnO composite films annealed in air at low temperatures and varying times should be conducted to gain a better understanding of the diffusion rates of the ZnO to the surface and adhesion interfaces.
- HRTEM of cross-sections taken from nanoindentation sites of uniformly He implanted Au films could be valuable to determine the strengthening mechanisms at the dislocation/cavity interaction scale to see which slip systems and dislocation types are, if at all, effectively pined by these structures.